AN ABSTRACT OF THE DISSERTATION OF

J. Trey Diulus for the degree of Doctor of Philosophy in Chemical Engineering presented on July 18, 2019

Title: Characterization and Investigations of Thin-Film Materials with X-ray Photoelectron Spectroscopy

Abstract approved:

_____

Gregory S. Herman

Surface characterization of materials is widely utilized over a range of disciplines and essential to the development of new materials, technology, or processes. Metal oxide nanoclusters have shown promise as potential new generation photoresist materials for extreme ultraviolet (EUV) nanolithography. Organotin clusters have been proposed as potential candidates for resist materials due to a high photoabsorption cross section in the EUV energy range. Before industrial implementation, these new materials must undergo rigorous analysis through the use of numerous characterization techniques to verify effectiveness and satisfactory performance. In addition to characterization, not much information is known about the radiation induced mechanism that causes a solubility transition; a key component for acting as a photoresist. The use of near ambient pressure X-ray photoelectron spectroscopy (NAPXPS) provides the ability to study chemical changes in organotin nanocluster thin films during radiation exposure in a range of ambient environments. NAPXPS using synchrotron X-rays determined that impinging photon energy can play a role in the solubility transition mechanism

since the total electron yield is dependent on the photon energy. The presence of ambient oxygen was also shown to enhance resist sensitivity. NAPXPS with a monochromated Al Kα X-rays were used to measure a contrast curve, further highlighting oxygen's ability to enhance resist sensitivity, while also showing a decrease in sensitivity for ambients of nitrogen, water, and methanol. Thermal NAPXPS studies following the solubility transition in the resist determined a significant amount of carbon remains in the film even though carbon removal was hypothesized to be a primary step during solubility transition. This led to the conclusion that a metal oxide polymer is formed following sufficient X-ray exposure and annealing. Metal oxide materials have also shown promise as oxidation catalysts. The conversion of volatile organic compounds to non-toxic molecules like CO_2 is important for pollution control. Interactions of near ambient pressures of 2-propanol (IPA) with a well ordered SnO_2 surface has yet to be studied from a mechanistic standpoint. For these studies, a SnO_2 single crystal was prepared with a stoichiometric oxidized surface and characterized with low energy electron diffraction (LEED) and valence band spectra. NAPXPS was used to track chemical changes in the Sn surface oxidation state and adsorbate reactions during exposure to up to 3 mbar of IPA and mixtures of IPA and oxygen at 400, 500, and 600 K. The reaction products were measured using mass spectrometry to compliment the NAPXPS results. Oxygen was found to be required for the complete conversion of IPA to CO_2 to prevent the surface reduction of the Sn, which otherwise would yield the intermediate product acetone. Ultimately, surface characterization is imperative towards forming foundational chemical knowledge of materials, which can lead to new and improved technology.

Characterization and Investigations of Thin-Film Materials with X-ray Photoelectron Spectroscopy

by
J. Trey Diulus

A DISSERTATION

submitted to

Oregon State University

in partial fulfillment of
the requirements for the
degree of

Doctor of Philosophy

Presented July 18, 2019
Commencement June 2020

Doctor of Philosophy dissertation of J. Trey Diulus presented on July 18, 2019

APPROVED:

Major Professor, representing Chemical Engineering

Head of the School of Chemical, Biological, and Environmental Engineering

Dean of the Graduate School

I understand that my dissertation will become part of the permanent collection of Oregon State University libraries. My signature below authorizes release of my dissertation to any reader upon request.

J. Trey Diulus, Author

ACKNOWLEDGEMENTS

I'm happy to thank my parents, John and Barbra Diulus, who were exceptionally supportive of me pursuing my educational goals. Both were always there for me when I needed them and I could never have accomplished this feat without them.

I would like to thank all the colleagues I've worked with through the years in the Herman group. Gustavo Albuquerque was a great role model for his hard work and dedication. Ryan Frederick was extremely helpful during my first year in the Herman group allowing me to get started as a PhD student. His close collaboration, hard work, and friendship were significantly important towards my success. Additionally, collaboration with Shane Lorona and his hard work led to a publication together. Other members of the group include Tyler McCrea and Stebby John, both of which were good friends and enjoyable to discuss research with during long hours in the office.

There are two very important scientists that I would like to thank, who were vital components towards me obtaining my knowledge of XPS. First Bill Stickle, and his work with HP that I was able to shadow, provided the initial basics of running XPS experiments. He was extremely helpful and enthusiastic about also teaching the more complicated components of the technique. He also generously provided our lab with a copy of his XPS handbook which was extensively used during my time as a student. The other was Igor Lyubinetsky, who was able to show me how to align the monochromator in the PHI 5600 system and responsible for bringing up the Specs NAPXPS system. Igor was a great learning resource and collaborated with me on a

majority of my projects. The amount of time we spent servicing equipment was spent with good company.

Another important colleague I need to thank is Joe Bergevin. Joe was a great person to work with and an enthusiastic problem solver. If I had a problem with something, I could always rely on some input from Joe. Joe was also responsible for helping me learn how to use AFM. Without his help maintaining the PHI XPS, I would have had a difficult time focusing on my research and maintaining the Specs system.

For other equipment techniques and help, I would like to thank Jenn Amador and Shawn Decker with their help using the ellipsometer. Rick Pressley and Chris Tasker for their help with the clean room and training using equipment. I would also like to thank Chris for his help troubleshooting numerous equipment problems over the years I was a student. I want to thank Deok-Hie Park and Nizan Kenane for their help maintaining the TPD system. Nizan was also a great collaborator and colleague as a co-lead with me for the nanopatterning group. Her help writing quarterly reports and organizing meetings was greatly appreciated. Thank you to David Marsh, Sumit Saha, and Danielle Hutchison who were responsible for the syntheses of the nanocluster resist materials. I also want to thank Chris Nelson and the Writing Center at Oregon State for their help with article and dissertation draft reviews.

I want to thank all my committee members, John Conley, May Nyman, Zhenxing Feng, and Líney Árnadóttir. My committee was fantastic and extremely helpful towards shaping my program of study and giving me insight on my first “first author” paper following my preliminary exam. They have also provided numerous collaboration opportunities for me as well. Another important professor was Kelsey

Stoerzinger, who provided me the opportunity to collect data at ALS with her as well as a number collaborations. She played an important role in my maturity from being a data crunching grad student to being able to shape a story from a research idea. I also want to thank the staff in CBEE, especially Elisha Bracket, Lea Clayton, and Charlotte Williams, who were extremely helpful for administrative issues.

I also want to thank the Center for Sustainable Materials Chemistry for providing my PhD funding. It goes without saying that this dissertation literally would not be possible without support from the CSMC. Thank you to all the professors involved in the center that haven't been mentioned already, specifically Doug Keszler, Rick Garfunkel, and Yves Chabal. Bettye Maddux and Amanda Polly must also be thanked for all the logistical work they provided for the CSMC.

My friends, past and present all played a significant role in my success and mental health. Thank you to Peter Melero, David Mercado, Gabriel Sandler, Kylee Probert, Priya Parikh, Kellee Britt, Anthony Zea, Rich Hilliard, Ross Warner, Rebecca Paustian, and many others. Also thank you to my extended family members who have all shown me support during my experience as a PhD student.

Ultimately, none of this would be possible without my advisor Greg Herman. He showed confidence in my ability to be a research scientist and provided fantastic mentorship through my time as his student. I must thank him for his commitment to making me the best scientist I can be.

It goes without saying that I can't possibly formally thank everyone with the few pages I have. Ultimately, the number of people I've met and collaborated with at OSU have all been a joy to work with and I'm glad to have worked with all of them.

CONTRIBUTION OF AUTHORS

Some of the work presented in this presentation could not have been achieved without the help of many great scientists. Chapter 3 discusses TPD and ESD data for organotin thin films. The experimental setup was based on prior experiments performed by Ryan Frederick. Quantitative data analysis for both TPD and ESD were carried out using computational software designed by Ryan as well.

Chapter 4 presents NAPXPS data from Stanford Synchrotron Radiation Lightsource (SSRL) where a number of people were responsible for helping to collect spectra. A team of Ryan Frederick, Mengjun Li, Líney Árnadóttir, Igor Lyubinetsky, Danielle Hutchison, and Greg Herman alongside myself were needed for the measurements.

In Chapters 3, 4, and 5, all β-$NaSn_{13}$ Keggin precursor was synthesized by Danielle Hutchison in May Nyman's lab at Oregon State. The Sn_{12} cluster was synthesized by David Marsh at University of Oregon in Darren Johnson's lab.

Greg Herman provided contributions towards experimental design and interpretation of results for all experiments carried out in Chapters 3, 4, 5, and 6. Greg was also involved in manuscript editing for all chapters in this dissertation.

TABLE OF CONTENTS

Page

CHAPTER 1: INTRODUCTION 1

1.1 SURFACE SCIENCE 2

1.2 INDUSTRIAL IMPACT 2

1.3 INSTRUMENTATION & TECHNIQUES 3

1.4 APPROACHES TO SURFACE CHARACTERIZATION 5

1.5 MATERIALS OF INTEREST 6

1.5.1 Organotin Nanoclusters for Thin Film Photoresists *7*

1.5.2 Tin Oxide Catalysis Studied with NAPXPS *9*

CHAPTER 2: EXPERIMENTAL TECHNIQUES AND METHODS 12

2.1 ULTRA-HIGH VACUUM 13

2.2 TEMPERATURE PROGRAMMED DESORPTION MASS SPECTROMETRY 16

2.3 ELECTRON STIMULATED DESORPTION MASS SPECTROMETRY 18

2.4 X-RAY PHOTOELECTRON SPECTROSCOPY 20

2.5 SYNCHROTRON LIGHT SOURCE AND SPECTROSCOPY 27

2.7 LOW ENERGY ELECTRON DIFFRACTION 28

2.8 SPECTROSCOPIC ELLIPSOMETRY (SE) 30

2.9 ATOMIC FORCE MICROSCOPY 32

CHAPTER 3: CHARACTERIZATION OF ORGANOTIN PHOTORESIST MATERIALS 48

3.1 ABSTRACT 49

3.2 INTRODUCTION 50

3.3 EXPERIMENTAL 53

3.4 RESULTS AND DISCUSSION 55

3.5 CONCLUSIONS 62

3.6 ACKNOWLEDGEMENTS 63

CHAPTER 4: AMBIENT-PRESSURE XPS CHARACTERIZATION OF RADIATION INDUCED CHEMISTRIES OF ORGANOTIN CLUSTERS 70

4.1 ABSTRACT 71

4.2 INTRODUCTION 72

4.3 EXPERIMENTAL 74

4.4 RESULTS AND DISCUSSION 78

4.5 CONCLUSIONS 90

4.6 ACKNOWLEDGEMENTS 90

CHAPTER 5: EFFECT OF AMBIENT CONDITIONS ON ORGANOTIN EUV PHOTORESIST RADIATION CHEMISTRIES 99

5.1 ABSTRACT 100

5.2 INTRODUCTION 101

5.3 EXPERIMENTAL 105

5.4 RESULTS AND DISCUSSION 110

5.5 CONCLUSIONS 122

5.6 ACKNOWLEDGEMENTS 122

CHAPTER 6: SURFACE CHEMISTRY OF 2-PROPANOL ON SnO2(110) STUDIED WITH AMBIENT-PRESSURE XPS 132

6.1 ABSTRACT 133

6.2 INTRODUCTION 133

6.3 EXPERIMENTAL 135

6.4 RESULTS AND DISCUSSION 137

6.5 CONCLUSIONS 143

6.6 ACKNOWLEDGEMENTS 143

CHAPTER 7: CONCLUSIONS AND FUTURE DIRECTIONS 154

7.1 ORGANOTIN PHOTORESISTS 155

7.2 TIN OXIDE CATALYSIS.....160

REFERENCES.....164

LIST OF FIGURES

Figure Page

Figure 2.1. General schematic for the setup of the Hiden TPD Workstation. The sample is brought close to the mass spectrometer and heated through the stage for TPD measurements (a). An e^- gun source is focused onto the sample with the sample slightly retracted from the mass spectrometer for ESD measurements (b). 37

Figure 2.2. Schematic of electron excitation following exposure to either a photon source (X-rays) or electrons. On the left, an Auger transition occurs leading to the emission of a KL_1L_{23} electron for Auger spectra. On the right, the photoemitted 1s electron is measured to obtain core level XPS..... 38

Figure 2.3. Diagram of a standard NAPXPS setup with both dual anode and monochromatized X-ray sources. Differential pumping stages are used to achieve lower vacuum pressures at the detector compared to what is seen by the sample. Electrostatic lens filters are utilized to focus the collected electrons leading to an increase the signal seen by the detector. A mass spectrometer can also be added in the lens chamber to measure the partial pressures of molecules in the chamber..... 39

Figure 2.4. An example of peak fitted spectra using CasaXPS for Si 2p. On the bottom is spectra from HF etched Si, while the top is spectra after surface oxidation following exposure to 1 mbar O_2 at 573 K for ~4 hours. 40

Figure 2.5. Setup for a standard synchrotron endstation. Electrons are accelerated in the synchrotron source ring resulting in photons that can reach the endstation. Slits are used to diffract the photons while mirrors are used to focus the photons. A spherical reflection grating is used as a monochromator to tune the energy of the photons. 41

Figure 2.6. Schematic of a standard LEED setup. An e^- gun focuses a low energy electron beam onto a sample leading to electron diffraction. When the electrons hit the screen, diffraction spots are visible and correlate to the surface lattice in reciprocal space. 42

Figure 2.7. Images of a LEED diffraction pattern for stoichiometrically prepared SnO_2(110) using 60, 90, and 130 eV electron energies. The 1x1 pattern is seen for all three energies shown by the red rectangle. 43

Figure 2.8. Standard setup for a spectroscopic ellipsometer measurement. Monochromated light passes through a linear polarizer and then reflects of the sample surface into a detector. The measurement is dependent on the number of layers in the sample, their refractive index (n) of each layer, and the thickness (t) of each layer. . 44

Figure 2.9. An example fit using the J. A. Woollam CompleteEASE software. The β-$NaSn_{13}$ on 100 nm TO_x sample thickness was measured using a Cauchy model. The model parameters are plotted as dashed black lines, while the Ψ and Δ are plotted as red and green lines, respectively. The MSE gives the goodness of fit of the model to the experimental data for both Ψ and Δ. 45

Figure 2.10. General setup for an AFM measurement. The laser is focused to the back of the cantilever and reflected to a photodiode detector. As the tip moves up and down while traveling across the sample, the movement of the reflected spot is measured by the photodiode and processed into an image. 46

Figure 2.11. A screenshot image from Bruker Nanoscope software showing the ideal depiction of what a well-tuned cantilever phase and amplitude. The Gaussian peak represents the amplitude, while the negative slope line represents the phase. The inverted triangle shows the optimal resonant frequency chosen by the software. 47

Figure 3.1. AFM images for 5x5 μm scans of β-$NaSn_{13}$ Keggin (a) and Sn_{12} Football (b) organotin precursors. 64

Figure 3.2. TPD studies showing the primary mass profiles (a) and the inversion analysis to calculate a thermal desorption energy for a range of pre-factors (b) for both the β-$NaSn_{13}$ Keggin and Sn_{12} Football precursors. 65

Figure 3.3. ESD studies showing the primary mass profiles (a) and the desorption cross section analysis using Gaussian beam simulations (b) for both the β-$NaSn_{13}$ Keggin and Sn_{12} Football precursors. 66

Figure 3.4. XPS characterization of both the β-$NaSn_{13}$ Keggin and Sn_{12} Football precursors, comparing C 1s, O 1s, Sn 3d, Na 1s, and Sn MNN Auger spectra using Mg Kα dual anode X-ray source. 67

Figure 4.1. TEY XAS obtained from a β-NaSn13 film. 92

Figure 4.2. NAPXPS obtained for β-$NaSn_{13}$ in both UHV and P_{O_2} = 1 Torr using hν = 626 eV. (a) C 1s, (b) O 1s, and (c) Sn 3d core levels. 93

Figure 4.3. NAPXPS data obtained for different X-ray exposure times for C 1s in (a) UHV and (b) P_{O_2} = 1 Torr, and O 1s in (c) UHV and (d) P_{O_2} = 1 Torr. 94

Figure 4.4. X-ray induced change in peak intensity ratios: C-H component of the C 1s spectra obtained in (a) UHV, (b) P_{O_2} = 0.01 Torr, (c) P_{O_2} = 1 Torr, and (d) Total O 1s spectra at hν = 626 eV for indicated oxygen pressures. The curves in the figure (b,c) are fits to equation 1, while the lines in figure (a) are fits to a linear function. In figure (d) the UHV data are fit to equation 1, while the ambient oxygen data are fits to a linear function. 95

Figure 4.5. Atomic percent calculations showing the compositional changes for C 1s, O 1s, and Sn 3d core levels and their respective chemical states after sequential C 1s scans (42 min of exposure) at $h\nu$ = 626 eV. 96

Figure 4.6. Proposed mechanism showing the conversion from β-$NaSn_{13}$ to SnO_2. Photons are absorbed leading to photoemission (a), followed by electron scattering and generation of secondary electrons (b and c). The homolytic cleavage of butyl ligands (d) is enhanced in the presence of oxygen and provides a more efficient route to SnO_2 (e, f, and g). 97

Figure 5.1. Extended (a) and zoomed in (b) β-$NaSn_{13}$ contrast curves using Al K_α X-rays (50 W, 15 kV, 30° impingement) for UHV, P_{O_2} = 1 mbar, P_{D_2O}= 1 mbar, P_{MeOH} = 1 mbar, and P_{N_2}= 1 mbar ambients. Error bars were calculated from an average of three ellipsometer thickness measurements. 124

Figure 5.2. XPS for C 1s during exposure to UHV (a), P_{O_2} = 1 mbar (b), P_{D_2O}= 1 mbar (c), P_{MeOH} = 1 mbar (d), and P_{N_2}= 1 mbar (e) for both before X-ray exposure (initial) and after 30 min of X-ray exposure. 125

Figure 5.3. XPS for O 1s during exposure to UHV (a), P_{O_2} = 1 mbar (b), P_{D_2O}= 1 mbar (c), P_{MeOH} = 1 mbar (d), and P_{N_2}= 1 mbar (e) for both before X-ray exposure (initial) and after 30 min of exposure. 126

Figure 5.4. XPS for C 1s (a) and O 1s (b) before X-ray exposure and annealing designated "before anneal." Annealing was performed after 30 min X-ray exposure in ambients of UHV, P_{O_2} = 1 mbar, P_{D_2O}= 1 mbar, and P_{N_2}= 1 mbar, then cooled and pumped to UHV before the next set of spectra was collected. 127

Figure 5.5. Suggested chemical mechanism for the full lithographic process of patterning β-$NaSn_{13}$ in the presence of O_2. 128

Figure 6.1. A photographed image of a LEED pattern for the prepared stoichiometric surface using an electron energy of 90 eV. A visible 1x1 pattern is highlighted in the red box. The suggested ideal surface structure is shown in the cartoon below, with Sn (grey), O (red), and bridging O (yellow) atoms. 144

Figure 6.2. Valence band spectra using both monochromated Al kα X-rays (a) and He I UV light (b) for both the oxidized stoichiometric surface (black) and the reduced ion bombarded surface (red). 145

Figure 6.3. XPS of C 1s (a) and O 1s (b) of stoiciometrically oxidized SnO_2(110) after exposures to P_{IPA} = 0.1, 1, and 3 mbar at room temperature. 146

Figure 6.4. NAPXPS of C 1s (a) and O 1s (b) at P_{IPA} = 0.5 mbar for 400, 500, and 600 K, as well as after exposure at UHV. 147

Figure 6.5. Gas phase NAPXPS spectra of C 1s (a) and O 1s (b) at P_{IPA} = 0.5 mbar for 400, 500, and 600 K. 148

Figure 6.6. Subtracted mass spec data for acetone (m/z 43, yellow and m/z 58, red), CO_2 (m/z 44, blue), water (m/z 18, purple), hydrogen (m/z 2, pink), O_2 (m/z 32, black), and IPA (m/z 45, grey) at P_{IPA} = 0.5 mbar. 149

Figure 6.7. NAPXPS of C 1s (a) and O 1s (b) at $P_{IPA} = P_{O_2}$ = 0.5 mbar for 400, 500, and 600 K, as well as after exposure at UHV. 150

Figure 6.8. Gas phase NAPXPS spectra of C 1s (a) and O 1s (b) at $P_{IPA} = P_{O_2}$ = 0.5 mbar for 400, 500, and 600 K. 151

Figure 6.9. Subtracted mass spec data for acetone (m/z 43, yellow and m/z 58, red), CO_2 (m/z 44, blue), water (m/z 18, purple), hydrogen (m/z 2, pink), O_2 (m/z 32, black), and IPA (m/z 45, grey) at $P_{IPA} = P_{O_2}$ = 0.5 mbar. 152

Figure 6.10. Cartoon diagram of the mechanism for IPA adsorption and decomposition on a stoichiometric SnO2(110) surface. 153

LIST OF TABLES

Table Page

Table 3.1. Ellipsometry thickness measurements for the β-$NaSn_{13}$ Keggin and Sn_{12} Football precursors spin coated as thin films. 68

Table 3.2. XPS atomic percent calculations for the β-$NaSn_{13}$ Keggin and Sn_{12} dodecamer precursors. The Auger parameter is also calculated from the Sn $M_4N_{45}N_{45}$ kinetic energy. 69

Table 4.1. Ratio of TEY from β-NaSn13 resists normalized to $h\nu$ = 472 eV. Ratio of X-ray attenuation for different photon energies and oxygen partial pressures normalized to UHV. Photoabsorption cross section values obtained from Henke et al.[66] 98

Table 5.1. Calculated D_0 and D_{100} parameters for both photon dose (ph/cm^2 x10^{16}) and exposure time (sec). 129

Table 5.2. Calculated XPS At % values for C, O, and Sn obtained from C 1s, O 1s, and Sn 3d spectra before X-ray exposure (Initial) and after 30 min of exposure in UHV,P_{O_2} = 1 mbar, P_{D_2O}= 1 mbar, P_{MeOH} = 1 mbar, and P_{N_2}= 1 mbar. 130

Table 5.3. Calculated XPS At % percent information for C 1s, O 1s, and Sn 3d peaks post exposure after annealing to 170 °C for 5 min in UHV,P_{O_2} = 1 mbar, P_{D_2O} = 1 mbar, P_{MeOH} = 1 mbar, and P_{N_2}= 1 mbar. 131

LIST OF EQUATIONS

Equation Page

Eq. 2.1 Impingement rate calculation 15

Eq. 2.2 Polanyi-Wigner equation 17

Eq. 2.3 Desorption rate relationship for ESD 20

Eq. 2.4 Solved ESD equation for exponential decay of intensity 20

Eq. 2.5 Energy balance for photoemission 20

Eq. 2.6 Energy balance for Auger transition 21

Eq. 2.7 Atomic ratio dependence for XPS 26

Eq. 2.8 Sensitivity factor XPS atomic ratio calculation 26

Eq. 2.9 Wavelegnth of an electron 29

Eq. 2.10 Polarization calculation for ellipsometry 31

Eq. 2.11 Cauchy model for ellipsometry 32

Eq. 4.1 PSD model for exponential decay of intensity 82

Eq. 4.2 Normalized PSD model 83

Eq. 5.1 Conrast parameter calculation 109

Eq. 5.2 Fadley method XPS atomic ratio calculation 110

DEDICATION

I dedicate this dissertation to my grandmother Jo Cardillo.

CHAPTER 1:

INTRODUCTION

1.1 SURFACE SCIENCE

Surface characterization of materials is a widely applicable branch of chemical analysis that is utilized to study the chemistry of typically the top ~5 nm of a material surface. Obtaining a molecular-level understanding of the chemistry that occurs at surfaces is essential for the development of numerous technological applications, specifically in the fields of heterogeneous catalysis, energy storage, electrochemistry, semiconducting materials, and adhesive materials.[1] Within the semiconductor industry, characterization methods are required to help ensure nanoscale devices are correctly prepared and impurities do not affect performance. In the field of heterogeneous catalysis, characterization techniques are employed to understand atomic scale reaction mechanisms on solid-gas interfaces. By studying the surface chemistry of a material one can assess the optical, electrical, and/or mechanical properties of materials to better understand how a material might behave in an environment or application.[1] These fundamental studies provide the basis for the field of surface science.

1.2 INDUSTRIAL IMPACT

Over the past two centuries, the importance of surface science studies has been evident through numerous technological advancements. In the late 19th century and early 20th century, the production of both syngas and ammonia were two separate breakthroughs based on surface catalyzed reactions.[2] The study of micelles in the same time period are what paved the way for the development of soaps and other detergents.[2] Catalysis and colloids are just two of the many other disciplines, like photography,

electrochemistry, and tribology, which have surface science to thank for their development.[2]

Eventually, around the mid-20th century, advancements in surface science allowed for studies of microscopic chemistry instead of just macroscopic interactions.[2] This led to innovations in the creation of integrated microelectronic circuits, ink-jet printing, and many others, while also facilitating the advancements of previously studied disciplines.[2] Current technological advancements in modern society are undoubtedly tied to advancements in surface science. For many fields to develop past their current state, improvements in materials, process design, efficiency, etc. are required. Through surface science, the knowledge to make these types of improvements can be obtained.

1.3 INSTRUMENTATION & TECHNIQUES

In modern day surface science, fundamental chemistries are studied for a range of applications using multiple instrumental techniques. Many surface characterization techniques have been established over the past ~50 years, which require ultra-high vacuum (UHV) to create a pristine environment.[3] Modern advances in surface characterization have largely been driven by innovation in the field of vacuum science and technology.[3]

Vacuum systems are typically able to achieve ambient pressures of $\leq 10^{-9}$ mbar, which allows for the preparation of adsorbate-free and ordered surfaces.[2] These pure surfaces form an idealized model for studying either the underlying chemistry of a material or interfacial reactions between a material and other chemicals. In a practical

sense, a material's surface is imperfect with numerous defects as well as adsorbate contamination that can influence the chemistry. This presents numerous variables which can affect the chemistry that occurs on the surface and complicate the detailed understandings.

In order to make arguments about practical applications, we must first try to understand the basics of the chemical reactions that may or may not take place. While we may know certain systems, processes, or materials may work in practical use, surface characterization techniques are employed to obtain basic knowledge of a material's surface chemistry or chemical reaction mechanisms that occur through exposure to known concentrations of adsorbates.[2] This scientific approach forms building blocks of knowledge that can lead to improvements or innovations in current designs, or sometimes the creation of newer better performing materials.

Most surface characterization techniques utilize the interaction of either photons, electrons, or ions, with a material.[1] Through energy conservation, these particle interactions lead to either the generation of new particles or loss of energy in the incident particle, both of which can be measured and analyzed.[1] Some common techniques used today include X-ray photoelectron spectroscopy (XPS), Auger electron spectroscopy (AES), secondary ion mass spectrometry (SIMS), reflection absorption infrared spectroscopy (RAIRS), Rutherford backscattering (RBS), and ion scattering spectroscopy (ISS).[1] Electron microscopy [both scanning electron (SEM) and transmission electron (TEM)] as well as scanning tunneling microscopy (STM) are also widely used for nanoscale image characterization of surfaces.[1] All of these techniques

have advantages and disadvantages versus each other and can be utilized for different applications, sometimes in conjunction with each other.

1.4 APPROACHES TO SURFACE CHARACTERIZATION

Initially, studies of single monocrystalline solids and their interaction with gaseous adsorbates set the groundwork for modern surface science. Single crystals cut with exact surface terminations were loaded into vacuum systems and cleaned by bombarding the surface with Ar^+ ions, which leads to the removal of the topmost layer of atoms.[2] This process, known as ion sputtering, can remove adventitious contamination and surface oxide, but also introduces defects and can reduce the oxidation state of the atoms on the surface.[2] Typically, heating the sample can reorder the surface and reproduce the original surface orientation, however the resulting structure is sample dependent and at times can even introduce more defects or drive contamination from the bulk.[2] If bulk contaminants are found following heating (also called annealing) they can then be sputtered away. After a few cycles of sputtering and annealing, a pristine surface exempt of contamination can be prepared.[2,10] Obtaining a clean and ordered structure with control over the variables affecting the chemistry taking place is required for creating a building block model in order to limit variables.

Once a surface is prepared, the surface chemistry or interactions with molecules can be reproducibly studied. Classically, a simple molecule of interest can be leaked into the vacuum chamber at low pressures (~$1x10^{-8}$ mbar).[4] Diatomic molecules like CO were the first to be studied due to the simplicity of the molecule and possible binding configurations on the sample surface.[4] By controlling the pressure and length

of exposure, one can control the number of molecules that will stick, or adsorb, onto the surface (also known as the coverage). The interaction of adsorbed molecules on a surface can be studied with techniques, like XPS or RAIRS, to determine the chemistry taking place, including a change in oxidation state or estimating the adsorbate coverage on the surface. Realistically, any technological application for studying single crystals will never operate in an ultra-high vacuum without contamination. This approach merely establishes a foundation for the underlying interfacial chemistry taking place.

As the field of surface science continues to mature, more complicated molecules or substrates can be studied by applying the well understood models previously developed and then slowly adding complexities.[3] Currently, other materials like metal alloys, metal oxides, thin films, organic materials, nanoclusters, or biomaterials can be studied using the same or improved versions of surface characterization techniques.[3] Overall surface characterization provides a route to study a wide range of materials allowing for continued technological advancements and innovation.

1.5 MATERIALS OF INTEREST

This dissertation focuses on two separate types of materials: organometallic nanocluster thin films, and metal oxide single crystals. Nanoclusters and other nanomaterials can be studied as deposited thin films after synthesis to determine material properties and help guide synthesis design. [5,6,7,8,9] Metal-oxides have been shown to act as effective oxidation catalysts.[10,11,12] Recent advances in surface characterization methods have led to improved knowledge of well understood materials

through chemical analysis at pressures close to atmospheric conditions.[13,14,15] Research at near ambient (or NAP) conditions allow for more practically relevant studies by providing insight on how a material behaves closer to operating conditions.[13,14,15] NAP experiments using the following materials serve as the primary focal point throughout this dissertation.

1.5.1 Organotin Nanoclusters for Thin Film Photoresists

Organotin compounds have recently gained interest primarily due to the unique ability to form precisely controlled nanostructures at the atomic level.[16] These nanostructures are like building blocks where numerous structures can be formed, and additionally linked with an abundance of fragments to form even larger units.[16,17] By controlling the pH of the nanocluster solution, the nanostructure size can also be controlled.[17] Specific fragments can be chosen as ligands in order to implement designs of structures that can chemically behave a desired way when exposed to a known environment. The ability to control the size and fragments of the structure allows for control over the electronic structure of the nanocluster, which provides even greater chemical versatility.[16]

Organotin nanoclusters have a wide range of potential applications, including use as catalysts,[18,19,20] biocides,[21] polymer stabilizers,[21,22] anti-cancer agents,[23,24,25] and precursors for nanoscale materials.[26,27] For example, organotin nanoclusters can function as catalytic supports,[18,28] or as catalysts for transesterification and esterification reactions.[19,20] Organotin materials have been shown to exhibit both anti-viral and anti-cancer activity mainly due to their ability to interact with DNA.[23,24,25] Organotin nanoclusters can be synthesized with precise atomic-scale control, where

manipulation of size, shape, or structure allows for a range of chemical compositions and properties.[16,17] The Sn-C bond is also relatively weak (compared to a C-C bond) which makes organotin compounds photosensitive. This provides for promising application as inorganic photoresists for extreme ultraviolet (EUV) photolithography.[29,30,31]

EUV photolithography is an industrial process in the semiconductor industry which utilizes a photosensitive material to create a mask that is resistant to chemical etching to write patterns onto substrates. The photosensitive material, also called a photoresist, can be patterned using a radiation source and then removed after the etching step to create a patterned substrate. EUV uses significantly shorter wavelengths (λ~13.5 nm) compared to the previous industrial standard, deep ultraviolet radiation (DUV, λ~193 nm), which allows much higher patterning resolution to be acheived.[31,32] A challenge for EUV photolithography is that the EUV photon energy ($h\nu$ = 92 eV) corresponds to low photoabsorption cross sections for elements typically used for photoresists.[31] As a result inorganic photoresists have gained considerable interest, especially those that incorporate tin which has a EUV photoabsorption cross section ~20x higher than carbon.[33] Recent studies have proposed that replacing the industry-standard polymer photoresists with metal oxide nanocluster photoresists will provide higher resolution, lower line-edge roughness (LER), higher etch resistance, and higher sensitivity for EUV photolithography.[5,6,7,8,9] Although organotin clusters have recently shown promise as next generation EUV photoresists[5,7,34] the chemical mechanisms that result in radiation-induced solubility transitions are not fully understood.[35]

In this dissertation, Chapter 3 discusses a standard set of surface characterization methods and analysis techniques to obtain a baseline for polyoxometalate photoresist materials. In chapters 4 and 5, further experiments are applied to an ideal organotin photoresist material that leads to mechanistic claims on the solubility transition that occurs through exposure to radiation.

1.5.2 Tin Oxide Catalysis Studied with NAPXPS

Metal oxides have unique electronic and chemical properties that make them interesting materials for catalysts,[10,11,12,13] semiconductor components,[10,36,37] and sensors.[10,36,37,38,39] For most metals, its oxide is the lowest free energy state when exposed to air, making these materials extremely stable in atmospheric conditions.[36] Metal oxides can store oxygen in the lattice allowing for efficient transfer of oxygen in oxygen-based reactions.[13,36] Due to the high stability, presence of lattice oxygen, and generally low cost, metal oxides have been extensively studied as catalytic electrodes in electrocatalysis.[13,36] Dielectric materials in semiconductor devices are also commonly metal oxides, due to their temperature stability, corrosion resistance, and low cost.[36] Some metal oxides are conductive and can instead be utilized as semiconducting materials.[36,37] The electrical resistivity can additionally be altered through adsorbates on the surface, making metal oxides prime candidates for gas sensing.[38,39]

Studies have shown that some metals are more reactive in their oxidized state for oxidation catalysis.[10] In most initial catalytic applications, metal oxides have been utilized as supports for other materials for the transport of oxygen to and from the substrate.[40,41] While oxide supported materials are promising catalysts and still heavily

studied,[36,40] other studies suggest oxides in pure form are also effective catalytic materials.[36,42] Recently, studies of well-ordered metal oxide surfaces have increased in the surface science community in order to better define the physical and chemical properties of these materials.[36,40] The catalytic oxidation of CO is a classic example of a study on well-ordered metal oxides.[40,42] Literature suggests that oxidation reactions with bulk oxides usually follow a Mars-van Krevelen mechanism, where lattice oxygen is removed during the reaction and then replaced by gas phase oxygen available in the ambient.[40,42] However, further studies are required for other oxides and molecule interactions to fully understand the oxidation chemistry of these materials for improved catalyst designs.

Tin dioxide (SnO_2) is an interesting metal oxide material due to its high conductivity and optical transparency.[10,36,129] There is additionally a wide range of obtainable surface structures, which means the oxygen surface concentration can be adjusted and potentially controlled, making it a promising material for oxidation catalysis.[10,129] The reactivity of SnO_2 can be strongly influenced by the surface structure and cation oxidation states.[10,129] More recent studies showed that the surface Sn^{2+}/Sn^{4+} ratio strongly influenced the oxidation activity, specifically for CO oxidation.[12] While standard UHV surface characterization studies are useful in determining a potential mechanistic route, the pressure gap between vacuum and operating conditions makes it challenging to completely define how the material behaves during operation.[13] Instead, with NAPXPS, spectra can be collected during exposures of molecules at near ambient pressures (up to ~1 mbar). Obtaining mechanistic insights at higher pressures

closer to that of operating conditions will lead to more practical information for the design of catalytic materials.[13]

In chapter 6, the catalytic conversion of 2-propanol (IPA) to CO_2 with a SnO_2 catalyst is studied using NAPXPS. A SnO_2(110) single crystal is prepared with a stoichiometric surface and exposed to high pressures of IPA and mixtures of IPA and molecular O_2 to determine the chemical reaction mechanism that occurs as IPA is oxidized to CO_2.

CHAPTER 2:

EXPERIMENTAL TECHNIQUES AND METHODS

2.1 ULTRA-HIGH VACUUM

For many surface characterization techniques, a low-pressure environment is required. This is either due to the detection sensitivity of the equipment, or to keep the surface pristine by preventing any potential background signal from contamination. Vacuum is typically described in tiers based on achievable pressure, e.g. low vacuum (1000 – 1 mbar), medium vacuum (1 – 10^{-3} mbar), high vacuum (10^{-3} – 10^{-7} mbar), and ultra-high vacuum (UHV) (10^{-7} – 10^{-11} mbar).[43] UHV can be obtained with the combination of multiple pumps. Turbomolecular (turbo) pumps can achieve vacuum pressures of ~10^{-9} mbar by spinning a turbine at high speeds (1-10 kHz). The volumetric flow rate through a turbo is mostly constant at low pressures, but decreases significantly as it approaches ~10^{-3} mbar as this is the transition pressure between molecular and laminar flow.[43] In order for a turbo pump to reach its maximum designed rotation speed, a backing pump is needed to lower the pressure in the chamber and turbo pump to approach molecular flow. Backing pumps can be any type of rotary or diaphragm pump, but dry pumps are the most common due to the possibility of chamber contamination through back diffusion with oil pumps.

When a chamber is being pumped for the first time, a pressure of only ~10^{-7} mbar is usually achievable (based on the chamber volume) due to adsorbed water on the chamber walls. This water is not effectively pumped unless heat is applied to vaporize the water into the gas phase. A “bake” is a standard procedure done to vacuum systems where heating straps covered in aluminum foil, or specially designed heating jackets, are wrapped around the chamber and the chamber is heated to 120-140 °C. The temperature should be hot enough that you can efficiently remove the water from the

system, but not too hot where plastic is melted, feedthroughs/equipment are damaged, or a pressure is obtained that is too high for the turbos to pump. Usually any plastic on the system is removed and feedthroughs are covered with Al foil to prevent damage.

To achieve even lower pressures than baked turbo systems, a sorption or cryogenic pump can be added to the system. Hydrogen, helium, and other light molecules are notoriously difficult to pump with turbo pumps due to their molecular size.[43] A cold trap can be implemented where liquid nitrogen is used to cool a wall in the chamber to about -170 °C. This will only lead to molecules being trapped through adsorption onto the cold wall. Once the cooling source is no longer applied, the molecules can desorb back into the chamber ambient. Another common solution is a titanium sublimation pump, where a layer of titanium is deposited on a cold wall and acts as a getter. Molecules react with the freshly deposited film and multiple cycles of newly deposited titanium can lower the chamber pressure.[43] The other more popular sorption pump is an ion pump. Ion pumps ionize the gasses that interact with it and then use a large voltage (3-7 kV) to chemically trap the ions into an electrode material.[43] These pumps provide the most effective way to pump hydrogen and noble gasses, and are required to obtain chamber pressures of 10^{-11} mbar.[43]

Once the desired chamber environment is reached, samples can be prepared or introduced through a load lock chamber. For surface chemistry, it is important to consider the surface interactions that will occur at UHV pressures. Using the kinetic theory of gasses, we can obtain a relationship for the flux of molecules impinging onto a surface for a specific pressure (P), shown in Eq. 2.1.[2]

$$F = \frac{N_A P}{\sqrt{2\pi MRT}} \quad \text{(Eq. 2.1)}$$

Calculating the flux for impinging molecular oxygen atoms, where the molar mass (M) of O_2 is 32 g/mol, N_A is 6.02×10^{23} atoms/mol, R is 8.314 J/mol/K, at room temperature (T = 300 K) and pressure (1.3×10^{-6} mbar), we get a value of ~4×10^{14} atoms/cm^2/s impinging with the surface. Even at pressures ~8 magnitudes below atmospheric pressure, there are still a significant amount of molecule collisions that occur. If we factor in that the number of atoms on a solid surface is roughly 10^{15} atoms/cm^2, and then assume that each collision leads to a molecule sticking to the surface, we can estimate that the surface is completely covered in 1 second.[2] This provides a separate unit commonly used in vacuum science known as a Langmuir (L), which is equivalent to 1.3×10^{-6} mbar*sec. Essentially, assuming a sticking coefficient of 1 (100% of collisions stick to the surface), 1 L results in one monolayer of molecules adsorbed on the surface.

The Langmuir unit significantly stresses the notion that UHV is required for pristine surfaces. Obtaining UHV at a pressure of 10^{-10} mbar (7.6×10^{-11} Torr), it would take 10000 seconds (~3 hours) to get one monolayer with all molecules sticking. It is also important to consider the collisions of molecules with the surface for ambient experiments. Gas molecules can be intentionally leaked at a specified pressure for a period of time to obtain a defined coverage or determine chemical changes through these interactions. The ambient conditions play a significant role in many of the following techniques when used for chemical analysis.

2.2 TEMPERATURE PROGRAMMED DESORPTION MASS SPECTROMETRY

Mass spectrometry can be used to measure desorbing species from a material to obtain information about the adsorbates binding energy on a surface, or the thermal stability of a thin film on a surface. Temperature programmed desorption (TPD) experiments are performed by heating a sample using a linear ramp rate and using a mass spectrometer to measure desorbing species from the sample.[44,45] In Figure 2.1a, a general setup of a Hiden TPD Workstation is shown, which was the system used for all TPD experiments in this dissertation. While linearly heating a sample, one can collect a thermal profile for a specific mass, where the measured intensity in the profile correlates to the partial pressure of a mass plotted with respect to the sample temperature. If a monolayer of a molecule is bound to a surface (e.g. butyl ligands bound to tin atoms on a SnO_2 surface), once enough thermal energy is applied to the sample, the bond between the adsorbed molecule and surface atom breaks, leading to the desorption of the molecule. The mass spectrometer will then monitor an increase in the intensity for the mass of the desorbed species at the time of desorption. The mass data can be linked with the temperature data to form the TPD profile.

Obtaining a desorption temperature for the removal of an adsorbed molecule or the complete decomposition of a thin film is important for determining thermal stability. In Chapter 3, TPD experiments were carried out to determine at what temperature organotin resists can be heated before the films decompose. This is important to the semiconductor industry as there are numerous baking steps during photolithography, meaning a resist material must remain stable up to temperatures

required to remove residual solvent. This information is also extremely useful for general material and process design. TPD can additionally be used for calibrating sample temperature measurements. Collecting TPD for a well-studied sample that has a sharp desorption profile at a specific temperature can be used to set proportional-integral-derivative settings on a temperature controller and also ensure the measured temperature matches the known value.

Significant additional information can be extracted from TPD spectra. The increase in mass intensity is directly correlated to the amount of adsorbed species that desorb. This means the area under the desorption profile can be used to calculate an effective coverage for the desorbing species. This is only the case if the desorbing molecule has a distinct mass from other molecules in the background, or can be labeled appropriately to track only the desorbing molecule's intensity change. The profile shape can be used to determine the order of the thermally-induced reaction. Therefore, an experiment can be designed where varying amounts of material are adsorbed or deposited onto a surface and then heated to track desorption. Depending on how the profile shape changes with respect to surface coverage, one can determine the kinetics of the desorption to be either zeroth, first, second, or a higher order. Finally, the activation energy for desorption can also be calculated using the Polanyi-Wigner equation Eq. 2.2.[46]

$$I(T) \sim \left(-\frac{d\theta}{dt}\right) = v(\theta, T) * \theta^n * \exp\left(\frac{-E_{des}(\theta, T)}{k_B T}\right) \qquad \text{(Eq. 2.2)}$$

Where I(T) represents the mass spectrometer intensity as a function of temperature (T), ν is the frequency factor, θ is the coverage, E_{des} is the desorption energy, k_B is the

Boltzmann constant, and $\frac{d\theta}{dt}$ is the desorption rate. By assuming or measuring the desorption order and estimating a range of frequency factor values, Eq. 2.2 can be inverted to calculate a range of desorption energies. This inversion analysis was utilized in Chapter 3 to obtain desorption energies for the thermal cleavage of butyl tin bonds in organotin photoresists.

2.3 ELECTRON STIMULATED DESORPTION MASS SPECTROMETRY

Similar to TPD, electron stimulated desorption (ESD) is another mass spectrometry technique that measures desorbing species from a sample. For ESD, an electron gun is used to create an electron beam which impinges on the sample causing bonds to break and adsorbed species to desorb. Electron irradiation can typically be used to break bonds by colliding with a sample through electronic excitation from the absorption of an electron, leading to bond breakage and desorption.[47,48] Once desorption occurs, a mass spectrometer measures the intensity of the desorbing species.[47,48] Usually a shutter is used to block the electron beam from hitting the sample, allowing control for when the electron beam interacts with the sample. Once the shutter is open, an immediate response showing the increase in signal intensity is obtained. ESD experiments completed in this dissertation also used the Hiden TPD Workstation shown in Figure 2.1b.

An alternative approach to using ESD is to determine a materials sensitivity to electron irradiation. As mentioned in Chapter 3 about metal organic photoresists, the primary mechanism for generating a solubility change was hypothesized to be due to

low energy electron interactions.[45,47,49,50] Low energy electrons are generated through the absorption of a photon by an atom which results in the emission of an electron, based on the photoelectric effect. If desorption occurs during an ESD experiment, then the hypothesis for the role of low energy electrons can be verified. Moreover, performing an ESD experiment and tracking desorbed species can be directly correlated to the resist sensitivity.[47]

Electron beams of different shapes, sizes, and energies can be used for ESD experiments. A focused Gaussian beam will provide a larger sample current to a smaller area on the sample compared to a defocused wide area beam. In order to truly determine electron sensitivity, one must account for the beam shape, exposed area and current. The beam current can be measured using a Faraday cup connected to a picoammeter. If the Faraday cup is mounted on an XYZ manipulator, one can measure the current in multiple positions and generate a beam profile. Once a beam profile is obtained, a beam current density can be calculated by integrating over the profile.

As desorption occurs, less molecules are available for interaction with the impinging electrons, thus the desorption follows an exponential decay profile. A constant desorption profile would only be possible if the number of impinging electrons (beam current) was increasing. The kinetics of an exponentially decaying desorption profile can be determined assuming the beam current is constant. Eq. 2.3 relates the first order desorption rate $\frac{d\theta}{dt}$ to a ratio of the desorption cross section (Q), adsorbate coverage (θ), beam current density (J), and time to the charge of an electron (ε).[51]

$$\left(-\frac{d\theta}{dt}\right) = \frac{\theta QJ}{\varepsilon} t \quad \text{(Eq. 2.3)}$$

Similar to TPD, the intensity change in the mass spectrometer can be directly correlated to the change in adsorbate coverage, therefore we can rewrite this equation using the mass spectrometer intensity (i) and solve the equation using a constant (i_0) at time t = 0 to give Eq. 2.4.

$$ln\left(\frac{i(t)}{i_0}\right) = \frac{QJ}{\varepsilon} t \quad \text{(Eq. 2.4)}$$

With Eq 2.4, we can take the natural log of the mass spectra intensities and the calculated beam current density to calculate the desorption cross section. This value essentially represents the probability of an electron interaction leading to a desorbing species. The effective desorption cross section was calculated in Chapter 3 for organotin photoresists and plays an important role in the design of experiments completed in Chapters 4 and 5.

2.4 X-RAY PHOTOELECTRON SPECTROSCOPY

X-ray photoelectron spectroscopy (XPS) is a powerful technique that provides chemical state and compositional information for a material.[52,53] Based on the photoelectric effect, when a photon is absorbed by an electron of an atom in a material, the energy of the photon is transferred to the electron, leading to the ejection of the electron. The fundamental energy balance for this process is shown in Eq. 2.5:[53]

$$E_{kin} = hv - E_B - \Phi_S \quad \text{(Eq. 2.5)}$$

Where E_{kin} is the kinetic energy of the ejected electron, E_B is the binding energy that must be overcome to eject the electron, hv is the photon source energy, and Φ_S is the

workfunction of the spectrometer.[52] Since the electrons in all elements have distinct binding energies, the photoemitted electrons can be measured with an electron energy analyzer and the resulting data used as a "chemical fingerprint." Only hydrogen and helium are typically not analyzed with XPS due their low photoemission cross sections.[54]

During photoemission, another process called an Auger transition occurs that can also be measured which contributes to the XPS data.[52,53] When an electron is ejected, a core hole is created. In order to achieve a stable energy state, a relaxation process takes place where an outer electron fills the core hole.[52,53] The resulting energy from this relaxation can cause either a characteristic X-ray emission or the ejection of another outer shell electron.[52,53] Figure 2.2 shows a schematic for both events during the photoexcitation process. Both processes can be measured by separate techniques to identify elements. For the purposes of XPS, the ejected electron is still important as it can also be measured with the electron analyzer. The energy balance for the KL_1L_{23} transition is shown in Eq. 2.6:[52]

$$E_{kin}(KL_1L_{23}) = E_K - E_{L_1} - E_{L_{23}} - \Phi_S \qquad \text{(Eq. 2.6)}$$

Where E_K is the binding energy for the K shell electron, E_{L_1} is the binding energy for the L_1 electron that replaced the core hole, and $E_{L_{23}}$ is the binding energy of the L_{23} electron that was ejected.[52] Notice that the photon source energy is not present in the equation. This is because the kinetic energy of an Auger ejected electron is independent of the photon energy required to create the transition, as long as the photon energy is larger than E_K to create the core hole needed for the transition to occur.

There is some standard XPS nomenclature based on quantum physics theory which is used to designate what electrons correlate to each transition. From quantum theory, the principal quantum number represents the different energy levels for electrons in an atom. The azimuthal quantum number determines the angular momentum of an orbital and is established by the quantum number. Electrons emitted during XPS are named by the energy level and orbital they were ejected from. This means an electron ejected from the second energy level (n = 2) and the s orbital (l = 0) will be denoted a "2s" electron. For orbitals with larger angular momentum, like a p orbital (l = 1), the electron spin must be considered. The electron spin and angular momentum of the orbital can interact leading to spin orbit splitting which causes the spectra for one orbital to be split in two. Again from quantum theory, the spin values can be $\pm\frac{1}{2}$, and is added to the angular momentum. For the p orbital, we can get a spin of $\frac{1}{2}$ and $\frac{3}{2}$. In Figure 2.2 we see the number of electrons present in the 1s, 2s, $2p_{1/2}$ and $2p_{3/2}$ orbitals. Spin orbit splitting determines the ratio of the doublet obtain with XPS, where $p_{3/2}$ and $p_{1/2}$ have a ratio of 2:1, $d_{5/2}$ and $d_{3/2}$ have a ratio of 3:2, and $f_{7/2}$ and $f_{5/2}$ have a ratio of 4:3. X-ray notation is also commonly used for Auger transitions, where a letter and number represent the orbital transition. X-ray notation is also seen in Figure 2.2, starting at K (representing 1s) followed by L_1 (2s), L_2 ($2p_{1/2}$), L_3 ($2p_{3/2}$), etc.

XPS is limited by the environment in which it can be measured in. Electrons have an inelastic mean free path (IMFP) on the order of ~3 nm for the energies commonly measured with XPS.[52,53] This means that the technique is extremely surface sensitive, but also means that UHV is required since electron scattering can occur in

the gas phase. Recently, new systems have been designed with a workaround to this pressure gap problem. By designing a chamber that is differentially pumped and has a small working distance from the sample to the analyzer, near ambient pressure (NAP) XPS can be collected. Figure 2.3 shows the setup for a standard NAPXPS system. There are two pumping stages in the analyzer as well as one not shown in the analyzer. This provides a vacuum pressure on the order of 1 x 10^{-9} mbar in the detector, where sample ambient conditions can be set to up to 10 mbar.[13,14,15] Electrostatic lens filters are utilized to focus the photoemitted electrons through the analyzer chamber and into the detector.[13,14] The rest of the components in Figure 2.3 are standard in any basic and modern XPS system. Two different X-ray sources are typically used for XPS. A dual anode source uses a filament to bombard a metal anode with electrons. The source is called a dual anode as two anode materials are typically used allowing for the generation of two characteristic X-ray energies. For the case of the PHI 5600 system used in Chapter 3, the two anodes were Al and Mg, providing Al Kα and Mg Kα X-rays. Dual anode sources can be challenging for peak analysis due to secondary radiation ($K\alpha_x$ or Kβ, and Bremsstrahlung radiation) that is generated from the source, creating photoemission transitions known as satellite peaks.[52] In order to remove these extra peaks, a monochromatic source can be utilized. For monochromatic sources, an e^- gun bombards an anode material with electrons which generates photon emission. The produced X-rays are then reflected on quartz crystals causing the X-ray beam to diffract based on Bragg's law. If the alignment is set correctly, only the primary X-ray emission ($K\alpha_1$) wavelength will be focused onto the sample.

Figure 2.3 also shows a hemispherical analyzer and detector, which is the most important aspect of collecting energy distribution curves in XPS. Analyzers are set to a specific kinetic energy range by the user the electrons are counted at each kinetic energy, providing photoemission spectra. Electrons enter the analyzer where positive and negative fields guide the electrons to the detector. The user can set a pass energy, which is the energy that the electrons are decelerated to as they enter the analyzer. The pass energy is what is used to adjust the resolution of the analyzer. Adjusting the pass energy (or resolution) will lead to a change in the full width half maximum (FWHM) of the photoemission peak. Pass energies are generally chosen from 20-150 eV. Higher pass energies provide lower resolution but larger intensities, while low pass energies provide higher resolution but low intensities. Survey spectra, encompassing a large range (0-1400 eV for Al Kα), are usually collected with large pass energies at the cost of resolution, since the purpose is to identify peaks in the spectra. High resolution spectra can then be performed on desired peaks at smaller energy ranges and higher pass energies. The user can also set the number of data points by adjusting the energy step in the set energy range. Surveys have larger steps to reduce collection time, while high resolution scans have smaller steps. During electron detection, noise is typically detected resulting from the random collection of electrons over time. To decrease the noise in spectra, multiple scans can be collected and added together. Multi-channel detectors (shown in Figure 2.3) allow spectra to be collected faster leading to less noise.

XPS can provide chemical state and compositional information, however this information must be appropriately interpreted.[53,55,56] Energy differences in peaks may not be very distinguishable in some cases.[53,55,56] For example, if a material has

numerous oxidation states, the spectra will be seen as a distribution of the peaks for all of these states. Peak fitting is required to deconvolute spectra and obtain peak energy values which can then be used for oxidation state analysis. It is standard to utilize literature and reference samples to accurately fit spectra. Peaks in spectra can be fit based on theory to draw conclusions about a material. Peak shapes are typically fit using a mixture of Gaussian/Lorentzian components.[56] The interaction of the photoemitted electron and the material can lead to electron kinetic energies slightly lower (higher binding energies) than theoretically expected.[56] A phenomenon called shake up occurs following initial photoionization where the generated ion stays at an energy above the ground state.[53] This leads to asymmetry that occurs at higher binding energies than the photoemission peak. Shake up features are material specific and sometimes can make peak fitting exceptionally difficult. The background must also be considered as peak area changes will adjust the accuracy of the fit. The two most common are linear and Shirley backgrounds. Linear backgrounds fit a line to two ends of the peak, while Shirley backgrounds assume the peak area above the background is proportional to the intensity for the binding energy of each data point.[55] Shirley backgrounds are generally the most accurate for most peak fitting purposes.[55]

For most spectra, using a mixed Gaussian/Lorentzian shape with a Shirley background is appropriate to fit peaks. Figure 2.4 shows an example fit for Si 2p spectra following HF etching (bottom) and a four hour exposure to P_{O_2} = 1 mbar at 573 K (top). A Gaussian/Lorentzian ratio of 40 and a Shirley background was used for the fit. A doublet for the Si $2p_{3/2}$ and $2p_{1/2}$ is constrained to a 2:1 ratio and an energy splitting

provided from literature.[53,57] The silicon oxide peaks are constrained to energy positions that are also provided from literature for silicon oxide materials.[57] For the elemental peaks (purple and teal) a FWHM of 0.8 eV is seen. For the oxidized peaks at higher binding energies, the FWHM increases, making it difficult to distinguish the spin orbit split. Therefore, only one peak was used to fit the oxide peak contributions. Once a good fit is obtained with the applied constraints, one can calculate atomic densities using Eq. 2.7:[53]

$$n = \frac{I}{f\sigma\theta y\lambda AT} \quad \text{(Eq. 2.7)}$$

where n is the atomic density (atoms/cm^3), f is the X-ray flux (photons/cm^2/sec), σ is the elemental specific photoabsorption cross section (cm^{-2}), A is the analysis area (cm^2), λ is the IMFP (nm), θ is the photoemission efficiency, y is the detection efficiency, and T is the detection efficiency.[53] If we take the atomic ratio of two elements, we can calculate atomic percent values from Eq. 2.8:[53]

$$\frac{n_1}{n_2} = \frac{I_1/S_1}{I_2/S_2} \quad \text{(Eq. 2.8)}$$

where S is a measurable factor that represents $f\sigma\theta y\lambda AT$. This value is instrument specific, X-ray source dependent, and angle dependent.[53]

Obtaining atomic percent values can provide useful information about a material. In Chapter 3, calculated atomic percent values were used to determine the composition of organotin photoresists. In chapter 4, atomic ratios were calculated to distinguish chemical changes following exposures to different photon energies and ambient environments. Chapters 5 and 6 additionally used atomic percent calculations to make mechanistic conclusions about reaction mechanisms. Proper utilization of XPS

is imperative to framing foundational knowledge of material properties and chemical reactions.

2.5 SYNCHROTRON LIGHT SOURCE AND SPECTROSCOPY

XPS is dependent on the photon source and energy used for photoemission. With synchrotron light, a range of photon energies can be achieved which can be used for XPS. A synchrotron is a large ring where electrons are accelerated at high speeds leading to the generation of photons over a continuous spectrum.[52] Synchrotrons have numerous endstations present that have varying equipment for a wide range of radiation based techniques. Figure 2.5 shows a general setup for a synchrotron lightsource endstation used for XPS analysis. The light from the synchrotron ring reflects off a pre-focus mirror and focused through an entrance slit.[58] The entrance slit diverges the beam onto a spherical grating which then diffracts the beam to a wavelength of choice. The light then passes through an exit slit and diverges again before reflecting off a refocus mirror, focusing the photon beam onto the sample.

With the above-mentioned dual anode or monochromatic X-ray sources in Section 2.4, only one energy is achievable. This limits the transitions that can be studied in a material to the energy range of whatever anode is being used. An entire range of energies can be used with synchrotron light compared to traditional X-ray sources. Additionally, Eq. 2.7 shows a direct relationship with the photoabsorption cross section to the spectral intensity. The cross section is energy dependent, meaning the ability to utilize different photon energies can allow for higher intensity spectra for certain transitions. Another advantage of synchrotron sources is the ability to sweep the photon

energy on the sample. With XPS, only the detection energy for emitted electrons can be varied, allowing for the collection of a survey. By sweeping the photon energy, a new technique known as X-ray absorption spectroscopy (XAS) can be collected.[59] One can measure the photoabsorption edges to determine the energy required to create a photoemitted electron from a specific orbital.

In chapter 4, XAS was used to track the absorption edges of an organotin sample. As the photon energy is adjusted, the generated electrons create a sample current that can be measured, called the total electron yield (TEY). Once the absorption edge energies were obtained, XPS was collected above, below, or on specific edges to determine how the number of electrons plays a role in the radiation induced mechanism for organotin photoresist.

2.7 LOW ENERGY ELECTRON DIFFRACTION

Obtaining chemical information from a surface is important to characterization, but sometimes the surface structure must be known to fully understand the characterization results. Collection of a diffraction pattern provides a route to determine the positions of atoms on a surface, which allows for the interpretation of the crystal lattice.[60] Obtaining a diffraction pattern can be done with low energy electron diffraction (LEED).[60] LEED can only measure a diffraction pattern on well-ordered surfaces. By utilizing the elastic scattering of low energy electrons on a surface, diffraction spots are formed and can be observed with a phosphorescent screen.[60] This is based on the wave properties of an electron, originally hypothesized by De Broglie, forming Eq. 2.9:

$$\lambda_e = \frac{h}{m_e v} = \frac{h}{\rho_e} \quad \text{(Eq. 2.9)}$$

Where the wavelength of an electron is equal to Planck's constant divided by the momentum of the electron.[60]

A standard LEED setup is shown in Figure 2.6, where a grounded sample is placed in front of an e-gun. The e-gun is set to low energies (10-200 eV) and can be adjusted to a desired energy during exposure. The scattered electrons are diffracted back towards the LEED and pass through a set of grids before reaching the phosphor screen. The first grid is grounded to reduce electrostatic deflection of the diffracted electrons. The second grid has a negative voltage to allow for only elastically scattered electrons for a small energy range to reach the phosphorescent screen. A large voltage is applied to the phosphorescent screen (4-6 kV) to make the diffraction spots visible. Additional grids can also be used for enhanced diffraction spot visibility. Adding a grid that is grounded before the phosphorescent screen will eliminate interference from the high voltage on the screen.

LEED is useful for quickly and routinely determining the symmetry of the surface and determine if there is a reconstruction.[60] Diffraction patterns are formed in reciprocal space of the lattice, meaning one can estimate a LEED pattern by converting the real space lattice vectors to reciprocal space. Figure 2.7 shows the effect of changing the energy for a stoichiometrically prepared SnO_2(110) single crystal. At 60 eV (a) the space between diffraction spots is largest compared to 90 eV (b), and 130 eV (c). By adjusting the impinging beam energy, the radial distance of diffracted electrons is also adjusted based on Bragg's Law.[60] Therefore, adjusting the energy provides larger or

smaller diffraction patterns. In Chapter 6, collecting LEED prior to reaction studies was required to verify that the desired surface structure was obtained. Sample preparation was tested through numerous Ar^+ sputter/anneal cycles followed by high pressure O_2 exposure to obtain the 1x1 diffraction pattern.

2.8 SPECTROSCOPIC ELLIPSOMETRY (SE)

Spectroscopic ellipsometry (SE) is a technique that uses linearly polarized light to measure material properties of either a thin film on a substrate or a substrate itself.[61] Because the technique utilizes the change in reflectance of incident light, it can be extremely sensitive to very thin films (~0.1 nm).[61] A standard measurement is completed by using monochromated light from an arc lamp that passes through a polarizer creating linearly polarized light that is focused onto a sample. The light then reflects off the sample as elliptically polarized light into a rotating polarizer and enters a detector. Adjusting the angle of incidence will change the optical path length, meaning additional information can be obtained by combining measurements at numerous angles. The thickness, surface roughness, and other material properties like the bandgap and optical constants can be extracted from the measured reflected light.

The physical theory behind ellipsometry is based on the polarized light transmission equations for reflections in multi-layered materials. Two primary parameters, psi (Ψ) and delta (Δ), are measured during ellipsometry data collection. Ψ represents the amplitude ratio of s and p polarized light, while Δ is the phase quantity between s and p.[61] The polarization state change (ρ) can be measured from data

collection and then Ψ and Δ can be calculated using Eq. 2.10, where r_s and r_p are the Fresnel reflection coefficients for s and p light.[61]

$$\tan(\Psi) * e^{i\Delta} = \rho = \frac{r_p}{r_s} \quad \text{(Eq. 2.10)}$$

The ratio ρ is a function of both the wavelength of light (λ) used and the angle of incidence (θ).[61] Therefore, usually at least two measurements at different angles are utilized to optimize data accuracy.

For thin films processing and analysis, ellipsometry is extensively used to obtain thickness measurements. Thickness values are indirectly measured, as they must be fit to a model and then calculated. A model can be formed in most ellipsometry software, where a substrate and multiple layers are selected based on the sample being studied. The model contains optical constants, like the index of refraction (n) and the excitation coefficient (k) as well as a manually inputted (guessed) thickness. Once the model has been built, simulated data can be created and compared to the measured data. Values for these parameters in the model are adjusted until a good fit to the measured data is obtained with a low mean squared error (MSE).

Numerous models can be utilized for a range of different types of materials and interfaces, but for the purposes of this dissertation, a Cauchy model was used to examine the thicknesses of an organotin thin film spin coated on a thermally grown oxide (TO_x) Si substrate. Cauchy models are used for modelling dispersion in the index of refraction, and also commonly used for transparent materials, of which includes tin oxide based thin films.[61] The model equation relates the refractive index as a function of wavelength consisting of three parameters (A, B, and C), shown in Eq. 2.11.[61]

$$n(\lambda) = A + \frac{B}{\lambda^2} + \frac{C}{\lambda^4} \quad \text{(Eq. 2.11)}$$

An example of a fit for the β-$NaSn_{13}$ film on a TO_x substrate is shown in Figure 2.9, which was obtained using the CompleteEASE software by JA Woollam. The model is designed with a SI_JAW file for the Si substrate, along with a SIO2_JAW file for the thermally grown oxide. An additional layer, INTR_JAW is placed in between the oxide and substrate to account for the interface between the two. There is no thickness input for the substrate, while the interface and oxide thickness are well known and inputted manually as 1 nm and 101 nm, respectively. The plot shown in Figure 2.9 shows the measured Ψ and Δ data for three collected angles (55, 60, and 65°). The last layer in the model is the Cauchy file, where only the A parameter and thickness were set to fit in order to simplify the data analysis. The simulated data is also plotted as black dashed lines, obtaining a MSE of 15.447 and leading to an estimated thickness of 22.28 nm. Nominally, a MSE of greater than 30 is typically considered a bad fit where the data was discarded, collected again, or the fit parameters where further optimized. Multiple thickness measurements were carried out on the same sample and averaged to determine the thicknesses for all organotin thin film samples prepared and characterized in this dissertation.

2.9 ATOMIC FORCE MICROSCOPY

Collecting a microscopic image of a sample surface can be extremely useful for designing materials or studying chemical behavior on a micro scale. However, standard light microscopes that refract light to collect an image can only achieve a resolution

based on the wavelength of light used.[62] This limitation prevents the ability to collect images of nanoscale features. Instead of refracting light, scanning probe microscopy utilizes a probe or tip that interacts with the molecules/atoms on the surface and back calculates an image based on changes from interactions. There are numerous types of atomic force microscope imaging methods (AFM) (tapping, conductive, contact modes) but this section will only focus on tapping mode.

AFM microscopes have five primary components; a cantilever with a sharp tip on the end, a cantilever holder/stage, a piezo drive and a feedback connection to a computer for generating an image.[62] AFM probes are very thin trapezoidal shaped pieces, about 1-2 mm wide, with a cantilever (about 20 μm wide) extending from the end. A sharp tip with roughly a 10 nm radius (so sharp that it is not macroscopically visible) is located on the end of the cantilever. The cantilever is mounted to the holder or stage and a sample is loaded directly underneath the cantilever with the tip facing the sample. The stage or holder with the mounted cantilever is lowered so that the tip comes within nanometers of the surface. During the approach, the tip is constantly oscillating like a damping spring.[62] The amplitude of oscillation reduces as it approaches the sample, where this decrease can be used to set the position of the tip by selecting a desired amplitude.[62] At this point the tip is "engaged" and a scan can commence. The piezo drive lowers and raises the cantilever in the Z direction so that the tip can interact with the surface. The deflection away from the sample based on the surface morphology can be measured with a sensor creating a "height" measurement. There are numerous feedback possibilities, but the most standard is a laser diode sensor. A laser is aligned to the cantilever during setup which focuses the reflection towards a

photodiode. As the cantilever moves, the photodiode can detect the movements by how far the laser spot moves from its original position. The piezo drive can then move the sample in both X and Y directions creating a raster profile as the tip measures a small area on the sample. A basic example of the described AFM setup is shown in Figure 2.10. AFM images are usually analyzing small areas (~1-100 nm^2) since each pixel in the image is generated through the "tapping" motion from the cantilever.

There are a few aspects to consider before collecting a scan to ensure that a useful image is collected. Tip specifications are what determine the image resolution and also whether collecting an image is even possible for some materials.[62] The smaller the radius of the tip, the higher resolution you can achieve in terms of mapping out details on the surface.[62] For example, if the goal of an experiment is to measure dispersed nanoclusters on a surface and the tip being used has a radius larger than numerous clusters adjacent to each other, only one large agglomeration will be seen instead of numerous individual clusters. Additionally, the tip material must be soft enough to not cause damage to the surface, but not too soft that it will be damaged upon contact. Once a tip is damaged, a new one is needed for reliable measurements. If a tip damages the surface the image will also be unreliable and can lead to a collection of debris on the tip further impacting image measurements. Another important aspect is potential noise from external influences. Tips should be designed with a high resonance frequency so that vibrations from buildings or other low frequency noise are not coupled.[62] AFMs are usually situated on a floating table to limit vibrations seen during the measurement.

Setting up an AFM prior to scanning can be tricky. Once a cantilever is mounted and a sample loaded, the laser must be aligned to the cantilever and then focused for maximum voltage measured by the photodiode. The cantilever is then tuned to obtain a resonant frequency of the cantilever. This is done by vibrating the cantilever as the software measures the cantilever amplitude and phase voltage with respect to frequency. Ideally, the amplitude will form a Gaussian profile and the phase will intersect the amplitude just before the peak. An example of what an ideal tune looks like is shown in Figure 2.11. The chosen resonance frequency is the frequency where the peak of the amplitude occurs, designated by the inverted triangle in Figure 2.11. A brand new tip with a good tune will have the phase intersect the amplitude with a steep slope. Over time as the tip deteriorates, the slope of the phase will broaden and sometimes develop fluctuations as well.

Data analysis of AFM often requires some data processing. From Figure 2.10, one can see that the cantilever is angled as it moves across the sample. This means the collected image will be sloped on the same plane and the cantilever angle. In order to display a flat image, a flatten algorithm must be used in an image processing software. Additionally, for large area scans, a bow shape can form in the image due to non-linearity in the piezo driven stage. If this happens, the image can be processed by applying a plane fit. Second or third order plane fits are commonly used to remove the bow effect. While some data processing can be required, it is still possible to over-process the image leading to manipulated data. Higher order plane fits, shades, or filters should only be done if one knows what resulting data is expected.

AFM studies are primarily executed for obtaining surface morphology information. In Chapter 3, the morphology of two nanocluster photoresists were analyzed using a Bruker Veeco Innova SPM to study film uniformity. The biggest advantage of AFM is that most samples can be measured as long as the sample remains stable through contact with the tip, unlike with other scanning probe techniques like scanning tunneling microscopy (STM) that requires conductive samples. AFM does have a few disadvantages though. High resolution scans can take long amounts of time (~30 min per scan) depending on the system design. Large unexpected debris on the sample forming sharp changes in height (>100 nm) can lead to tip crashes, which will require mounting a new tip. Overall, the ability to obtain nanoscale height profiles can provide useful information for thin film studies.

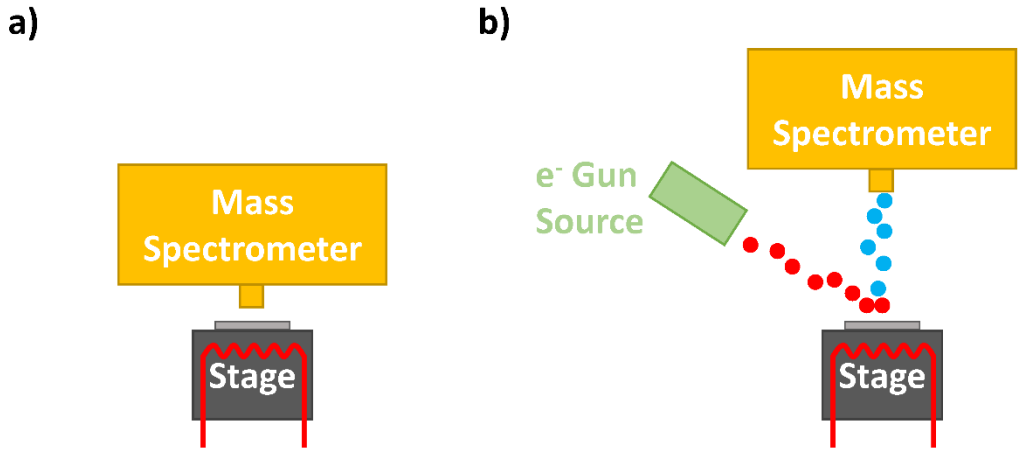

Figure 2.1. General schematic for the setup of the Hiden TPD Workstation. The sample is brought close to the mass spectrometer and heated through the stage for TPD measurements (a). An e^- gun source is focused onto the sample with the sample slightly retracted from the mass spectrometer for ESD measurements (b).

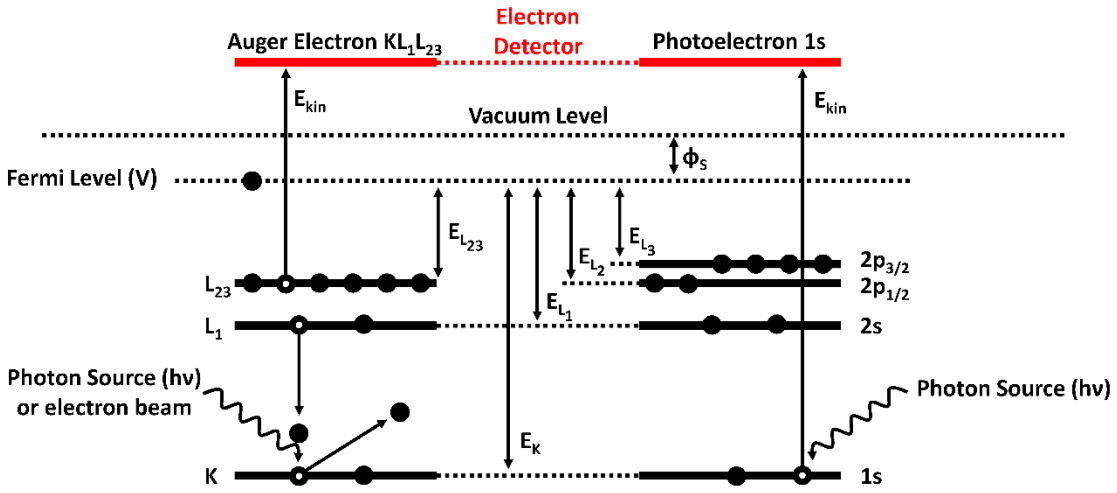

Figure 2.2. Schematic of electron excitation following exposure to either a photon source (X-rays) or electrons. On the left, an Auger transition occurs leading to the emission of a KL_1L_{23} electron for Auger spectra. On the right, the photoemitted 1s electron is measured to obtain core level XPS.

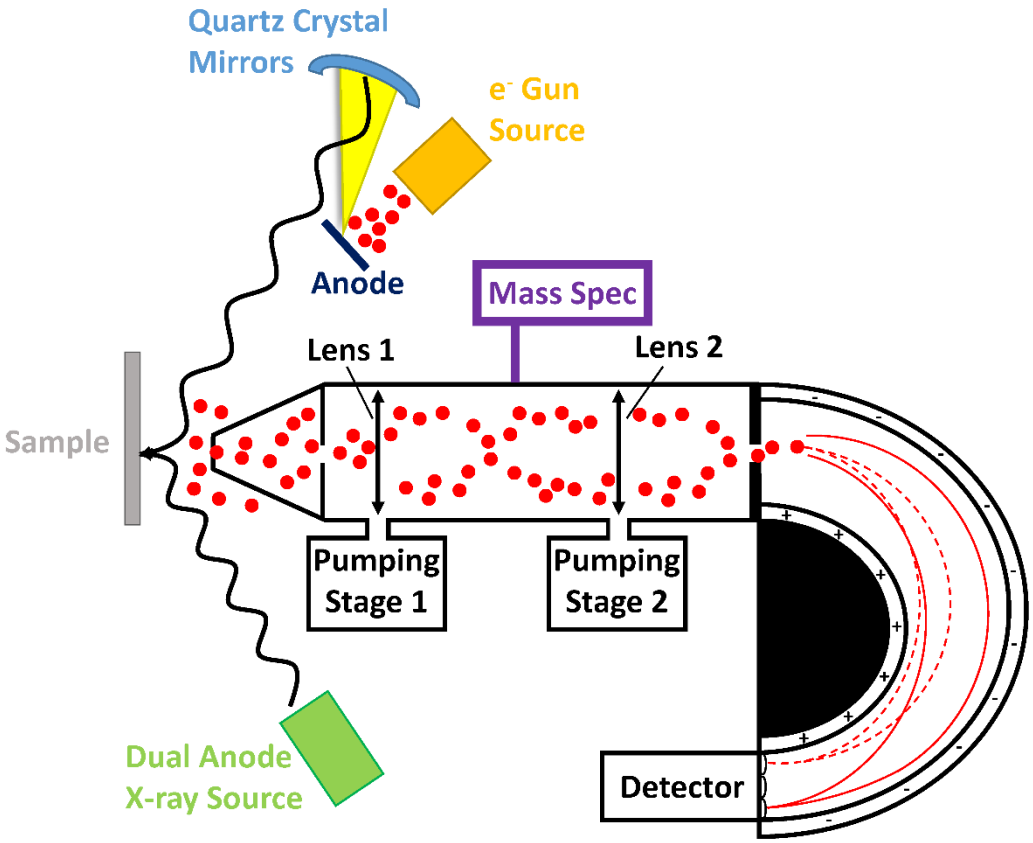

Figure 2.3. Diagram of a standard NAPXPS setup with both dual anode and monochromatized X-ray sources. Differential pumping stages are used to achieve lower vacuum pressures at the detector compared to what is seen by the sample. Electrostatic lens filters are utilized to focus the collected electrons leading to an increase the signal seen by the detector. A mass spectrometer can also be added in the lens chamber to measure the partial pressures of molecules in the chamber.

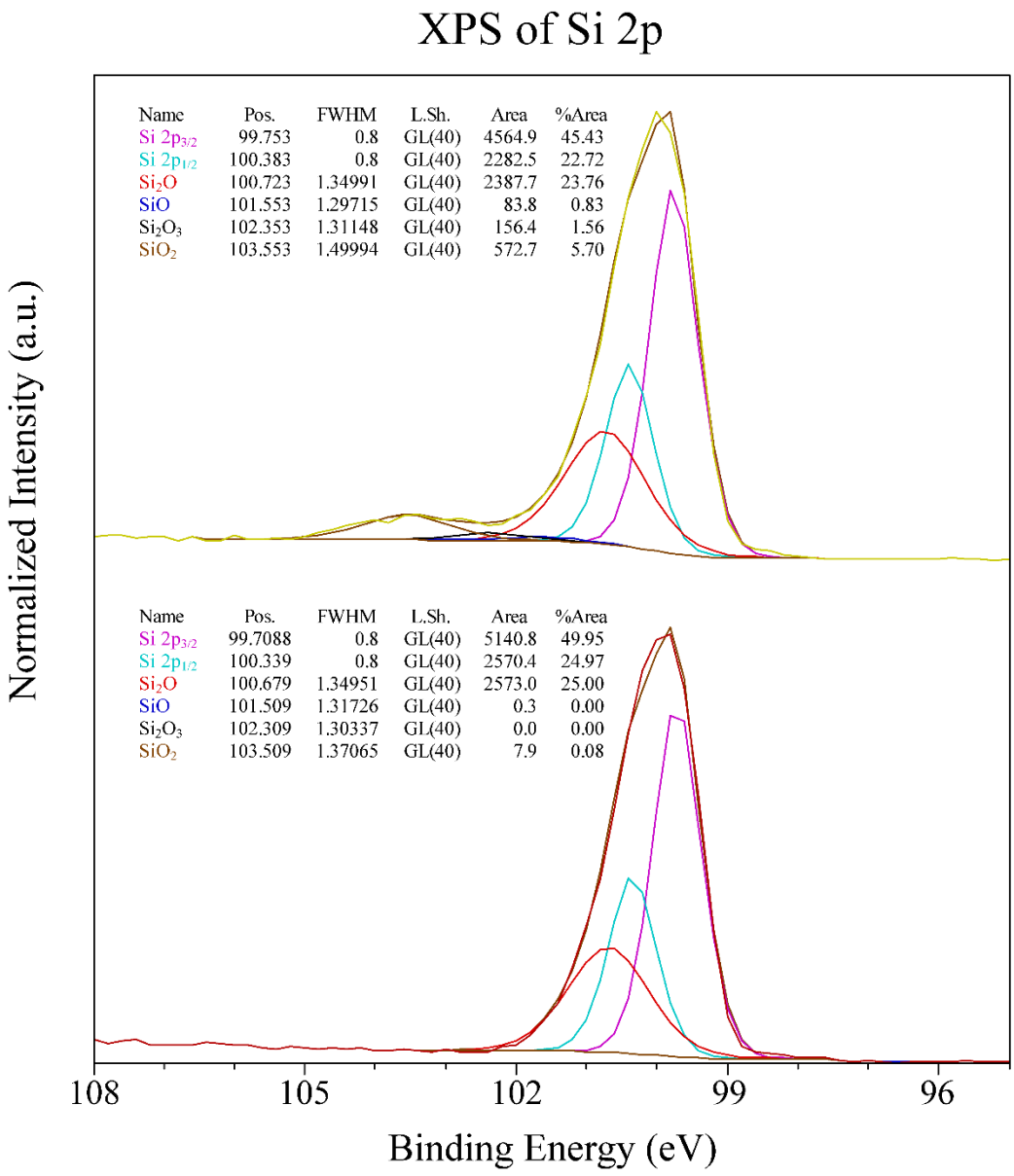

Figure 2.4. An example of peak fitted spectra using CasaXPS for Si 2p. On the bottom is spectra from HF etched Si, while the top is spectra after surface oxidation following exposure to 1 mbar O_2 at 573 K for ~4 hours.

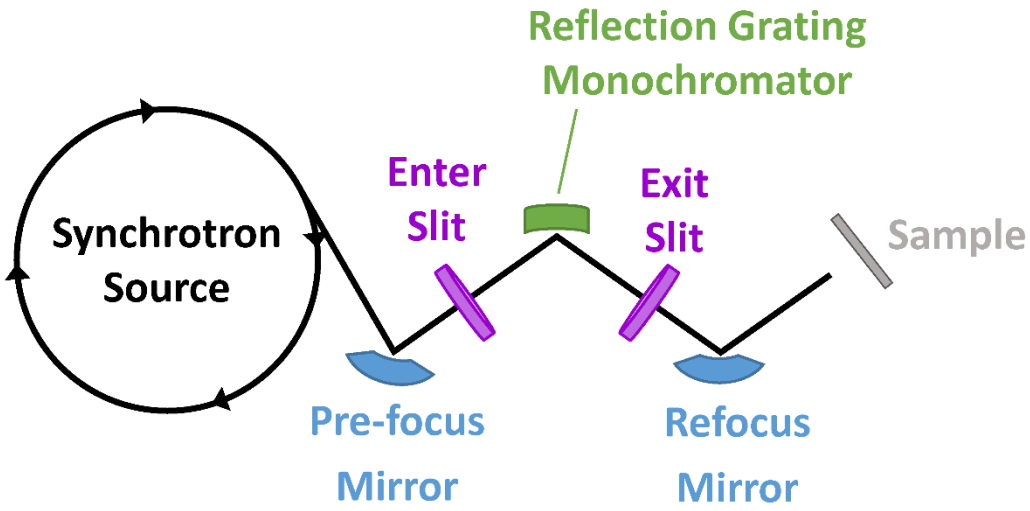

Figure 2.5. Setup for a standard synchrotron endstation. Electrons are accelerated in the synchrotron source ring resulting in photons that can reach the endstation. Slits are used to diffract the photons while mirrors are used to focus the photons. A spherical reflection grating is used as a monochromator to tune the energy of the photons.

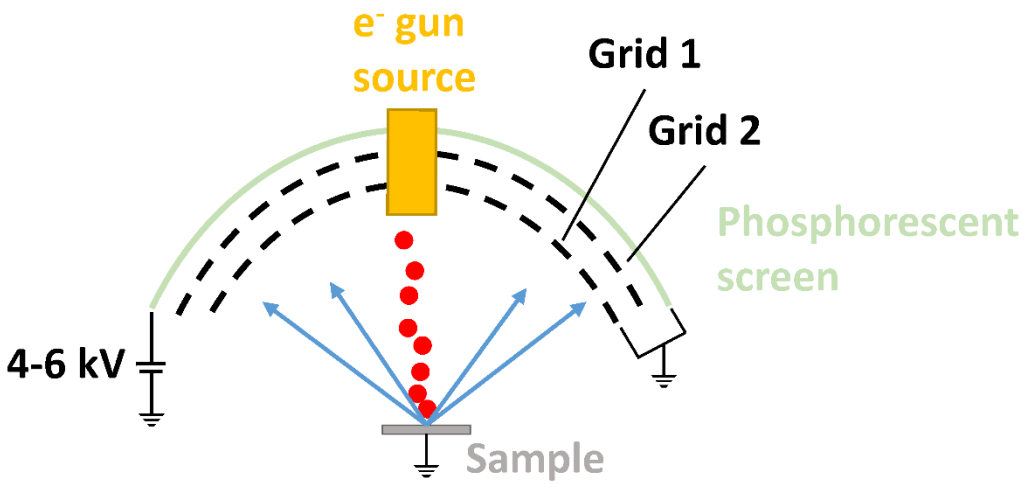

Figure 2.6. Schematic of a standard LEED setup. An e^- gun focuses a low energy electron beam onto a sample leading to electron diffraction. When the electrons hit the screen, diffraction spots are visible and correlate to the surface lattice in reciprocal space.

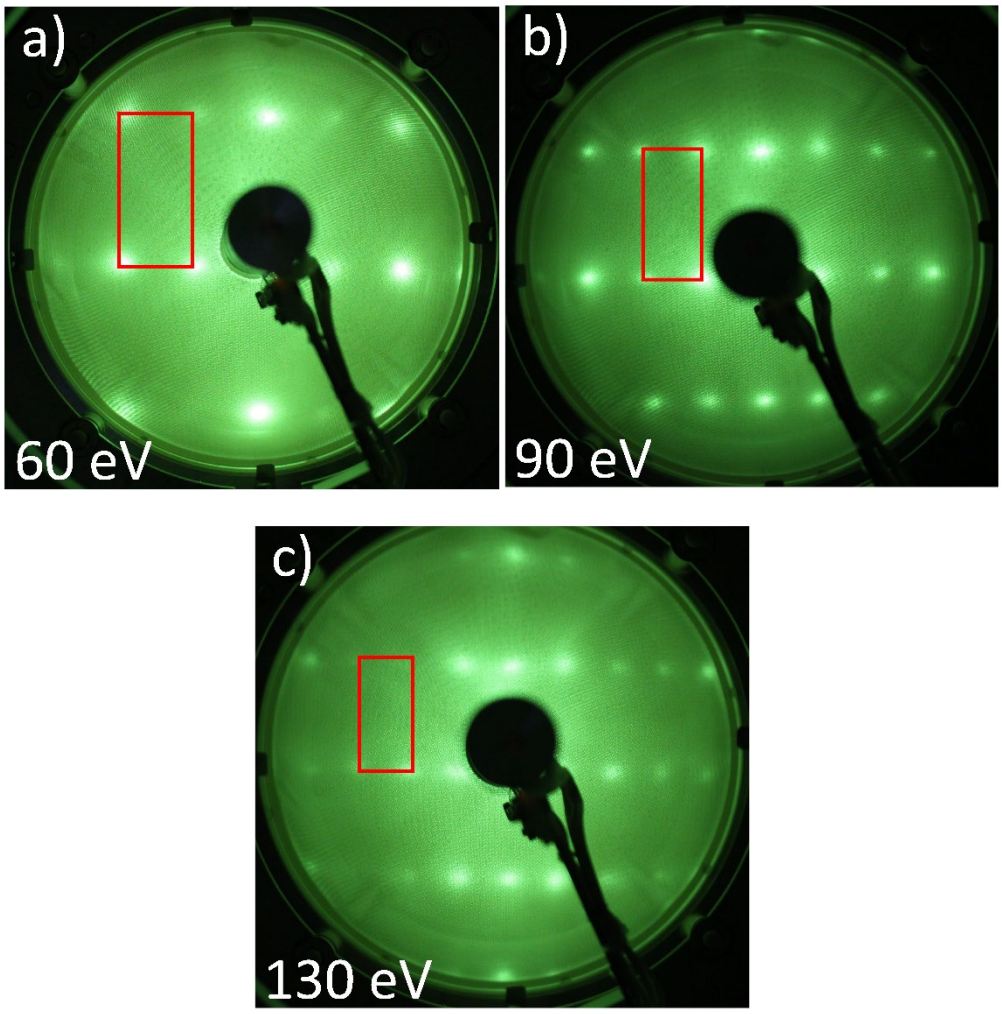

Figure 2.7. Images of a LEED diffraction pattern for stoichiometrically prepared SnO_2(110) using 60, 90, and 130 eV electron energies. The 1x1 pattern is seen for all three energies shown by the red rectangle.

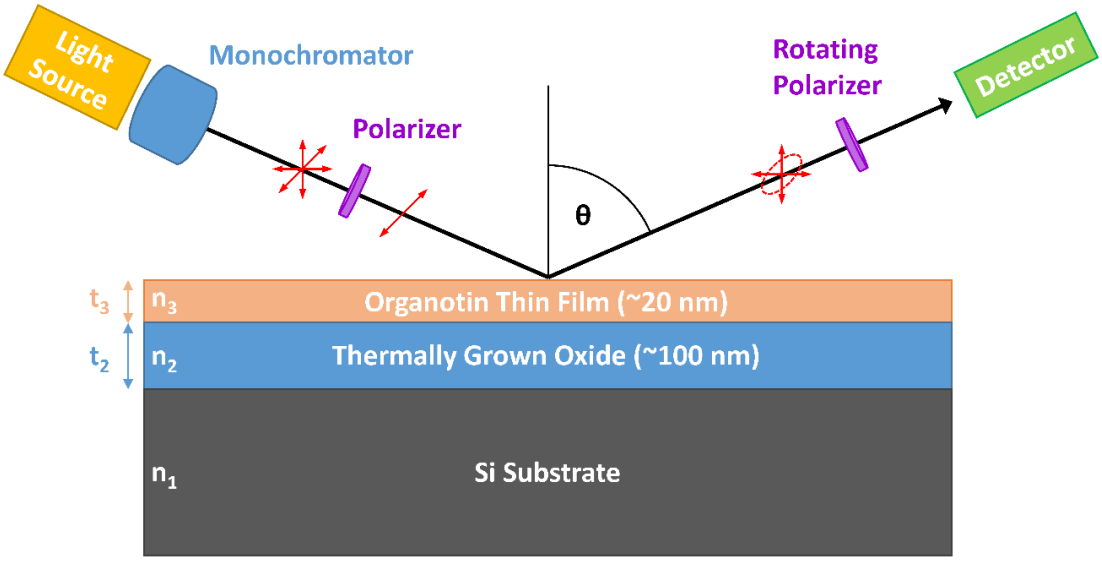

Figure 2.8. Standard setup for a spectroscopic ellipsometer measurement. Monochromated light passes through a linear polarizer and then reflects of the sample surface into a detector. The measurement is dependent on the number of layers in the sample, their refractive index (n) of each layer, and the thickness (t) of each layer.

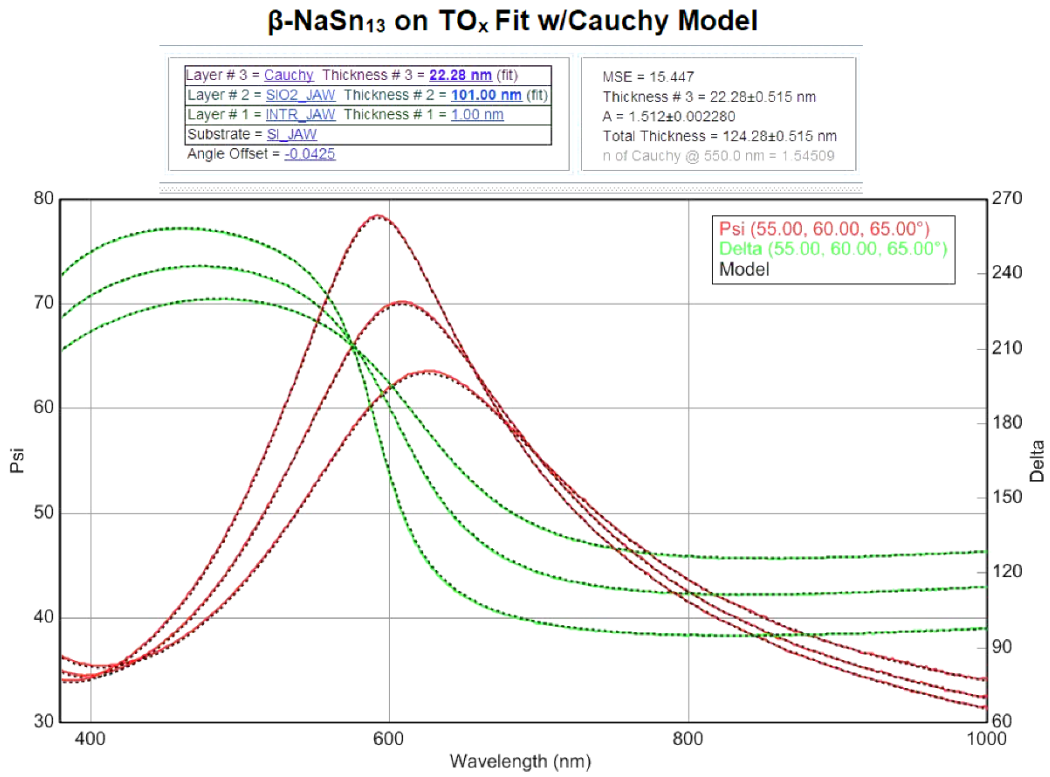

Figure 2.9. An example fit using the J. A. Woollam CompleteEASE software. The β-$NaSn_{13}$ on 100 nm TO_x sample thickness was measured using a Cauchy model. The model parameters are plotted as dashed black lines, while the Ψ and Δ are plotted as red and green lines, respectively. The MSE gives the goodness of fit of the model to the experimental data for both Ψ and Δ.

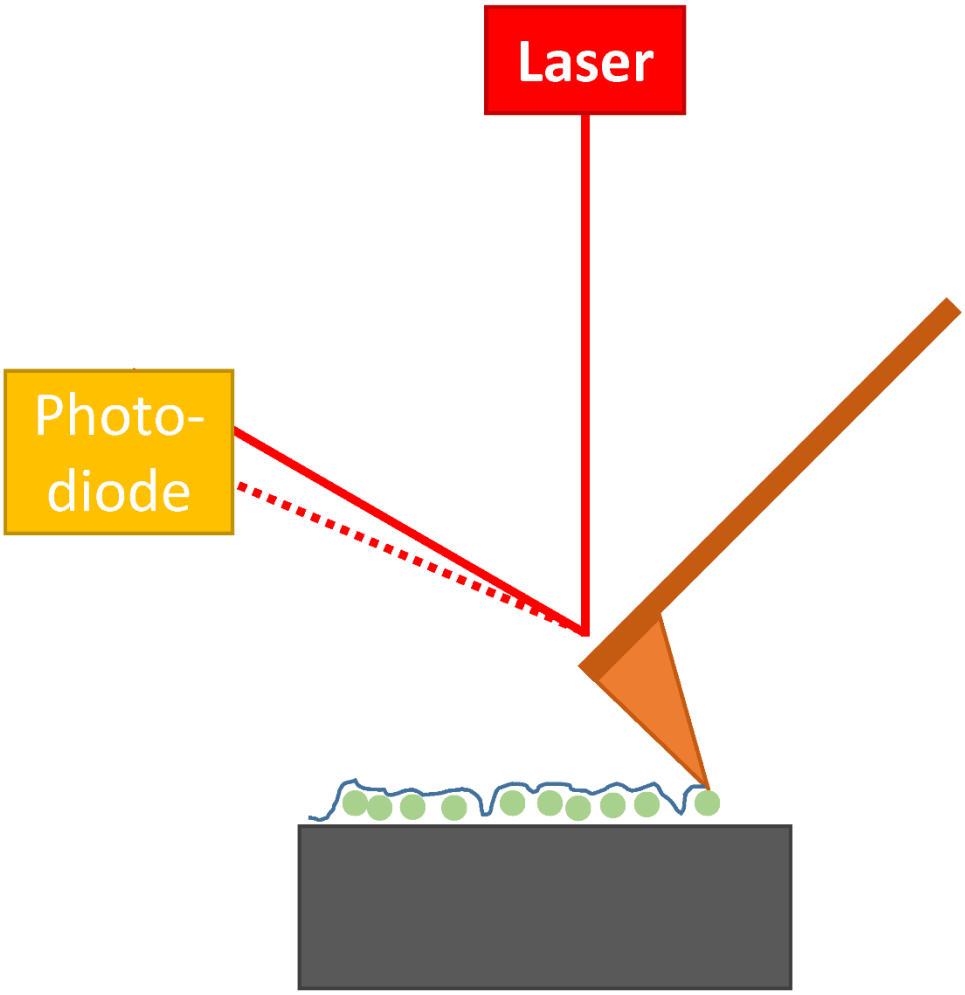

Figure 2.10. General setup for an AFM measurement. The laser is focused to the back of the cantilever and reflected to a photodiode detector. As the tip moves up and down while traveling across the sample, the movement of the reflected spot is measured by the photodiode and processed into an image.

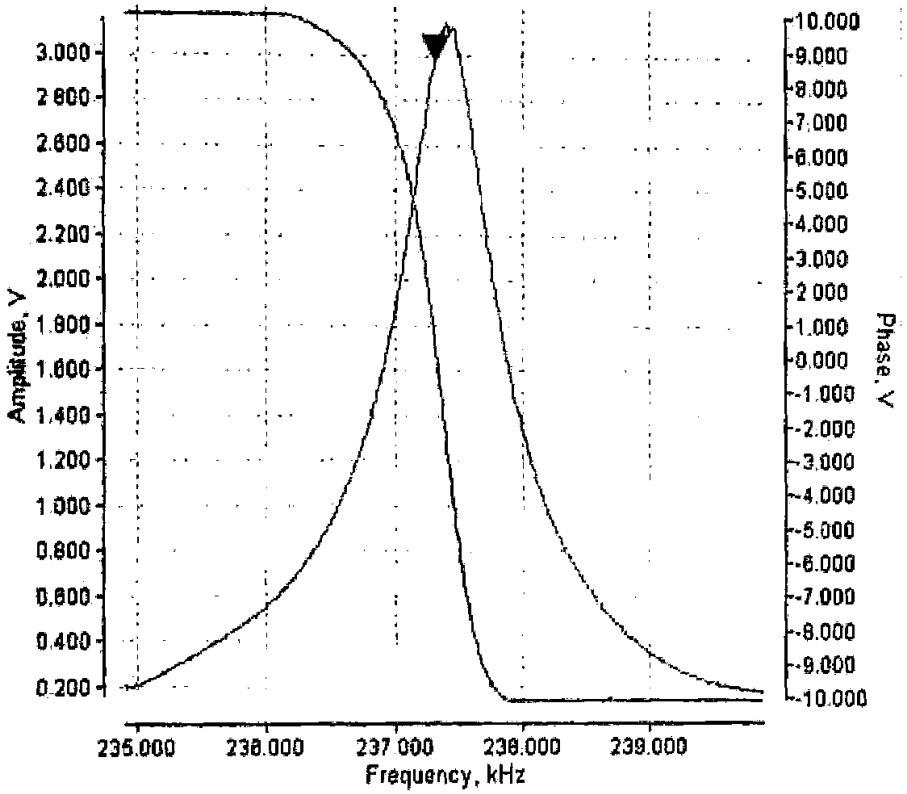

Figure 2.11. A screenshot image from Bruker Nanoscope software showing the ideal depiction of what a well-tuned cantilever phase and amplitude. The Gaussian peak represents the amplitude, while the negative slope line represents the phase. The inverted triangle shows the optimal resonant frequency chosen by the software.

CHAPTER 3:

CHARACTERIZATION OF ORGANOTIN PHOTORESIST MATERIALS

3.1 ABSTRACT

Significant advances in photoresists are necessary to improve throughput for extreme ultraviolet (EUV) photolithography for nanomanufacturing.[63] Organotin compounds are promising resist materials since tin has a high EUV absorption cross-section, which is ~30x higher than carbon.[33] Before implementing new materials into electronics processing, understanding material properties and establishing analysis methods for baseline measurements are imperative. Two synthesized organotin nanoclusters (Sn_{12} dodecamer and β-$NaSn_{13}$ Keggin) which are promising EUV photoresists will be discussed in more detail below. Both organotin nanoclusters were dissolved in 2-heptanone, spin coated onto silicon substrates, and then characterized with atomic force microscopy (AFM) and ellipsometry to determine uniformity and thickness. Thermal stability was measured through temperature programmed desorption (TPD) experiments, indicating that butyl-group desorption occurs at ~650 K and is the primary mechanism for thermal driven decomposition. Radiation sensitivity was studied with electron stimulated desorption (ESD), where low energy electrons with energies close to that of photoemitted, Auger, and secondary electrons during EUV were investigated. These electron interactions are what drives the solubility transition of organotin materials through cleavage of butyl-tin ligands. Atomic compositions of photoresist thin films were measured with X-ray photoelectron spectroscopy (XPS) experiments and found to be reasonably consistent with each compound structure. The combination of AFM, ellipsometry, TPD, ESD, and XPS techniques provide a standard for measuring and better understanding radiation induced

processes in organotin photoresist films, ultimately leading to mechanistic insights for tin and other metal-based inorganic resists.

3.2 INTRODUCTION

Improvements towards higher resolution photolithography are required for the field of microelectronics to continue to advance.[64] Extreme ultra-violet (EUV) lithography provides improved resolution due to the much shorter wavelength used compared to deep ultraviolet (DUV) lithography.[6,65] Further development of EUV lithography is required prior to industrial adoption for nanomanufacturing, where improvement of EUV photoresists that have high-resolution, low line-edge roughness (LER), and high sensitivity is critical.[5,64,65] Studies have recently indicated that organotin compounds can be promising inorganic photoresists.[5,64] This is, in part, due to the high EUV absorption cross-section for Sn, which is ~30x higher than carbon.[66] Organotin compounds have alkyl groups that render the compounds soluble in organic solvents, and allows them to remain stable against condensation in solution and in thin film form.

There are significant differences between various organotin nanoclusters. Two clusters have been suggested as potential model precursors for EUV implementation: the $\{(BuSn)_{12}O_{14}(OH)_6\}(OH)_2$ ("Sn_{12} dodecamer")[5] and the recently-discovered sodium-centered $[NaO_4(BuSn)_{12}(OH)_3(O)_9(OCH_3)_{12}(Sn(H_2O)_2)]$ ("β-$NaSn_{13}$ Keggin").[67] The Sn_{12} cluster is a charged cluster neutralized with hydroxyl counterions, while the β-$NaSn_{13}$ is charge neutral, meaning no counterions are required. The β-$NaSn_{13}$ also is templated with a Na atom at the center and includes some methoxy

ligands in addition to butyl ligands due to recrystallization in methanol as part of the synthesis.[67]

Determining the film deposition quality of both materials is required before detailed studies. As resolution increases, the film thickness of the resist must shrink to avoid pattern collapse following development.[68] When spin coating prior DUV resists, film thicknesses were typically on the order of hundreds of nm. In order for new materials to be utilized as photoresists for EUV, thin films of the cluster must be deposited onto a substrate. Ideally, deposited film thicknesses with the same height as the desired patterned feature is preferred. However, film quality can significantly deteriorate as the thickness is decreased. Obtaining smooth and uniform films is essential to photoresist pattering. Roughness or pinholes in the film can lead to unintentional etching of the substrate underneath. XPS data is used to verify the chemical composition and tin oxidation state for films of both clusters to ensure no chemical changes took place following spin coating.

The thermal or radiation induced removal of alkyl groups can significantly change the solubility of organotin compounds in organic solvents. This is potentially one of the mechanisms to enable contrast in photolithography using these compounds. Several other high-sensitivity inorganic photoresists have been studied, including $Hf(OH)_{4-2x-2y}(O_2)_x(SO_4)_y \cdot qH_2O$ (HafSOx).[6] Detailed characterization of the chemical changes that occur during processing HafSOx resists have provided insight into patterning reaction mechanisms. Due to the alkyl functionality of the butyl-tin precursors these photoresists should have significantly lower rates for condensation reactions compared to HafSOx. Since condensation reactions can limit the stability of

inorganic photoresist precursors, in solution and films, it is critical to understand the thermal induced chemistries and the stability of potential resist materials.

When organotin nanoclusters are exposed to EUV radiation, both photo- and Auger electrons are emitted, leading to inelastically scattered electrons that form lower kinetic energy secondary electrons. These electrons can interact with the atoms in the film, leading to homolytic cleavage between the Sn-C bonds from the butyl ligands.[45,47,49,50] Electron stimulated desorption (ESD) studies provide a route to assess this hypothesis. By utilizing an electron gun with an electron beam energy similar to the expected energies from the photoemitted low energy secondary electrons, the radiation sensitivity of the material can be determined. This has been done previously for commercial butyltin hydroxide oxide hydrate thin films have indicated that butyl ligands desorb upon exposure to low kinetic energy electrons. Due to the high cross section values obtained, homolytic cleavage of the butyl-tin bond was suggested.[45]

In this study, we examine and characterize two separate organotin photoresist precursors, β-$NaSn_{13}$ Keggin and Sn_{12} dodecamer. AFM and ellipsometry were used to measure film thickness and surface morphology of a spin coated thin film. XPS were used to characterize the chemical state information of the films and determine chemical composition. TPD experiments measured the thermal stabilities of both cluster films and calculated the thermal energy requirement for the cleavage of the butyl-tin bond. ESD experiments studied the radiation sensitivity of the films and quantified the number of electron interactions leading to desorption of butyl ligands. The complete characterization of both clusters provides information for future improvements to nanocluster design and establishes a basis for comparisons with new materials.

3.3 EXPERIMENTAL

The Sn_{12} dodecamer precursor was synthesized using the method outlined by Eychenne-Barron et al.[69] Following synthesis, tetramethyl ammonium hydroxide was used to replace tosylate counterions with hydroxyl counterions, and then crystallized. NMR with both ^{119}Sn and ^{13}C were utilized to ensure purity of the precursor. The synthesis for the β-$NaSn_{13}$ Keggin was outlined by Saha et al.[67] With both precursors, 20 mg/mL of precursor powder was dissolved in 2-heptanone (Alpha Aesar, 99% purity) and sonicated for 5 minutes. Si(100) wafers, with 100 nm thick thermal oxide (TOx), were used as substrates. For ESD experiments only, Si(100) with a native oxide were used instead to avoid charging effects from the thermal oxide layer. All substrates were pretreated using an acetone, 2-propanol, and deionized water rinse. The substrates were then exposed to a 50 watt O_2 plasma etch for five minutes. Approximately 7-10 drops of the solution were applied to the substrate surface and then spin-coated at 3000 RPM for 30 seconds. Samples were then annealed at 70 °C for 3 min in air to remove residual solvent. Each substrate was cleaved into 2x2 cm^2 squares and then cleaved into four 1x1 cm^2 squares for analysis.

All surface images were collected using a Veeco di-Innova AFM in tapping mode. The collection parameters for each experiment were set to 32 x 32 pixel resolution, using 5 μm/s scan rate over a 5 x 5 μm scan size. The aspect ratio for the images is 1.00 and the amplitude set point was 1716.62 mV. Each image was processed using a 3rd order plane fit and flattening filters with the Gwyddion 2.50 image

processing software. The tip was a RTESPA-300 probe with 40 N/m spring constant, 300 kHz resonant frequency, and 8-12 nm radius of curvature.

Ellipsometry data was collected using a JA Woollam MX-2000 ellipsometer. Data were collected over the interval from 400-1000nm, and modeled using the Cauchy equation. Mean square error (MSE) were used to determine goodness of fit. Data for MSE values above 30 were either recollected, recalculated with new estimates, or discarded. Thickness values were calculated through the software once an appropriate fit was determined. Measurements were collected in five locations (four corners and the center) on the sample and the values averaged.

TPD data were acquired with a Hiden Analytical TPD Workstation. All the measurements were performed at a chamber base pressure < 5 x 10^{9} Torr. A 1×1 cm^2 sample was heated from room temperature to 1173 K using a linear ramp rate of 15 °C/min. Mass spectra were obtained using a Hiden 3F series quadrupole mass spectrometer with a 20 μA emission current, electron impact ionization with a 70 eV ionization potential, a settle time of 50 ms, a dwell time of 200 ms, and a multiplier voltage of 2400 V.

Electron stimulated desorption was additionally acquired in the same Hiden Analytical TPD Workstation as TPD. A 1×1 cm^2 sample was positioned at the focal point of a low energy electron gun (Kimball Physics ELG-2 gun with EGPS-1022 power supply). A kinetic energy (E_{kin}) of 80eV was used as this energy corresponds to the approximate kinetic energy of photoemitted electrons following absorption of EUV photons. The electron beam current profile was determined using a Faraday cup with a circular pinhole (2 mm^2 area). During ESD measurements, the average current density

ranged from 0.5-0.8 μA/cm^2 and a 150 ms per m/z dwell time was used. Prior to both ESD and TPD experiments, the mass spectrometer was degassed for 10 min to achieve the lowest base pressure.

XPS was obtained using a PHI 5600 system (base pressure <2×10^{-10} Torr) with non-monochromatized Mg Kα radiation (hν=1253.6 eV). An electron analyzer pass energy of 29.35 eV, and a 45° emission angle were used for the measurements. The energy scale of the spectrometer was calibrated to Au $4f_{7/2}$ at 84.0 eV and Cu $2p_{3/2}$ at 932.7 eV. Atomic concentrations were calculated using instrument standard relative sensitivity factors for a 54.7° source-to-analyzer angle and corrected for the transmission function of the analyzer.[53] The XPS data were fit using CasaXPS, where the most intense peak in the spectrum was used to define the core-level full-width-half-maximum (FWHM) and Gaussian-Lorentzian mixing. A linear background was used to fit all spectra. All binding energies were charge corrected to the C 1s aliphatic carbon peak at 284.8 eV.[53]

3.4 RESULTS AND DISCUSSION

After film deposition, thickness of films were determined using ellipsometry. Data for the thickness measurements are shown in Table 3.1. Both films form with thicknesses of ~20 nm for the concentrations used. The MSE values for both suggest good fits, yet the Sn_{12} has about twice the MSE of the β-$NaSn_{13}$, suggesting the Sn_{12} film has additional roughness or other factors that lead to a worse fit. Assuming no more than 5 nm is removed from the exposure and development process, this would provide patterned film thicknesses of ~15-20 nm. Obtaining resist films with these

thicknesses allows for reducing potential pattern collapse when trying to obtain sub-10 nm half-pitch features.[64]

AFM studies were performed to determine spin coated film quality for both precursors. The ability for new resist materials to be deposited as uniform thin films is imperative. Poor film quality would lead to the material no longer being a candidate for photolithography, as the main importance is the ability to create a pattern in the underlying material below the thin film. Both precursors were spin coated onto Si substrates and characterized with AFM. Figure 3.1 shows two images of 5x5 μm scans for the Sn_{12} and β-$NaSn_{13}$ thin films. The β-$NaSn_{13}$ film in Figure 3.1a shows no features at all. The calculated mean squared roughness (R_q) roughness was only 0.46 nm. This is actually close to the noise of the tip, suggesting the film is exceptionally smooth. Numerous trials were carried out to make sure this result was real and not due to an improperly approached tip.

In Figure 3.1b, the Sn_{12} film shows a beadlike formation. The dark spots in the image reach a maximum of 36 nm below the highest point of the film. Since this height difference is larger than the suggested film thickness from ellipsometry, the dark spots likely represent the Si substrate. The radius of the beads are ~0.1 μm, which is significantly larger than an individual cluster radius that is ~5 Å. Therefore, we believe that the cluster is agglomerating on the surface and forming larger clusters with itself. Once a substrate is pretreated with a plasma O_2 etch, the surface is hydrophilic. Since the Sn_{12} precursor was dissolved in 2-heptanone, the solution will be hydrophobic. Surface functionalization was attempted with hexamethyldisilazane (HMDS), although this did not remove the beadlike formation and instead made larger clusters on the

surface. No difficulty was occurred when spin coating films with the β-$NaSn_{13}$ precursor, suggesting the problem with Sn_{12} could be related to the stability of the cluster and the counterions. Potentially the use of hydrophobic counterions may lead to more uniform films. Alternatively, using a different Si substrate may also improve film quality. All Sn_{12} films were spun onto either a native or thermally grown oxide, therefore the use of an HF etched surface may reduce surface roughness and improve adhesion. Another route would be to use Si(111) as the presence of dangling bonds may be advantageous for a charged cluster like Sn_{12}.[70]

While the film quality for the Sn_{12} precursor is not practical for nanolithography, we can still obtain useful information about the differences in thermal stability and radiation sensitivity compared to the β-$NaSn_{13}$ film. The thermal stability of both the Sn_{12} and β-$NaSn_{13}$ precursors were tested using TPD studies. First a mass survey was collected during a measurement to see what the main desorbing masses were during the experiment. Once the primary masses were determined, a higher resolution scan was collected. The primary masses tracked were for butyl desorption species (m/z 56 and 41) and oxygenate components (m/z 44 and 28) in addition to water (m/z 18). Figure 3.2a shows the TPD profile for each of the primary masses. The spectra were normalized to the tin density of the clusters in the film, which was calculated from Rutherford back scattering data. For the β-$NaSn_{13}$ film, the tin density was determined to be ~8.9×10^{15} cm^{-2}. For Sn_{12}, this value was 5.5×10^{15} cm^{-2}. Even though similar mass concentrations were used for both cluster solutions, the tin density in Sn_{12} is likely lower due to non-uniformity in the film compared to the β-$NaSn_{13}$.

The TPD spectra for both films are nearly identical and share the same primary desorption events. First there is a desorption event around 350 K where a peak is seen only for water (m/z 18). This is likely due to adsorbed water or hydroxyl recombination leading to water desorption.[45] Since both films are spin coated in atmosphere, there is likely to be some moisture present. The amount of water desorption from the β-$NaSn_{13}$ film is slightly greater, possibly due to more water being trapped in the film. The second desorption event occurs at 696 K where there is a sharp increase in m/z 41 and an increase for all other masses as well due to the butyl group cracking in the mass spectrometer. For these studies we use m/z 41 to represent butyl desorption. Where this desorption feature is most likely resulting from the thermal cleaving of the butyl ligand bound to Sn.[45] As this occurs, the film decomposes leading to the desorption of other species.

We can extract additional information from the TPD spectra using the Polanyi-Wigner inversion analysis. Using Eq. 2.2, we can calculate a range of desorption energies using estimates of pre-factors, and assuming first order desorption. The coverage (θ) was assumed to be the tin density in the film from Rutherford backscattering measurements. Pre-factor values can be determined using transition state theory, where the desorption temperature T = 696 K and chain length N = 4 were used.[71] Recent studies have shown that calculating ν with this method can overestimate the value by two to four orders of magnitude.[72] Adjusting the theoretical values to account for this overestimation provides a range of ν from 10^{16} to 10^{20}. Figure 3.2b shows the results of the inversion analysis for the specified ν values allowing for the calculation of the desorption energies. Both films show nearly an identical value for

each ν. The energy also remains mostly constant for both films, suggesting the bond strength is uniform for butyl-tin. The energy values range from 2.4-3.1 eV, which is consistent with literature for the heat of combustion for butyl-tin.[73] This means the film thermal stability is directly related to the strength of the butyl-tin bond.

ESD was used to determine the radiation sensitivity of both materials. Since low energy electrons from the photoemission process have been proposed to drive the solubility transition chemistry,[47,50,45] we can test this hypothesis using ESD with low energy electrons (80 eV). First a mass survey was collected, similar to TPD, during electron irradiation to determine the primary masses. The same masses from TPD were found to be the primary desorbing species during ESD. Figure 3.3a shows the spectra for ESD using a Gaussian beam profile. The spectra were additionally normalized to the tin density for the clusters in the film. No desorption occurs until the shutter is opened, leading to a sharp increase in signal measured by the mass spectrometer. Over time, this intensity slowly decays as there are less species available for the interaction with the impinging electrons. This decay is not seen for water (m/z 18), suggesting the water desorption is not related to electron-induced desorption. For the Sn_{12} there are more butyl species desorb compared to β-$NaSn_{13}$, although nearly identical desorption rates occur for oxygenate species with both films. This is likely due to the presence of methyl ligands on tin sites in the β-$NaSn_{13}$ that can also interact with an electron and result in desorption. This would explain the larger ratio of oxygenate desorption to butyl desorption in β-$NaSn_{13}$ compared to Sn_{12}.

We can also obtain quantitative information from the ESD spectra by calculating the cross sections. By obtaining a beam profile through current

measurements from a picoammeter, we can use Eq. 2.4 to create simulated data for the desorption decay. Comparing the simulated data to the measured data allows us to obtain an effective desorption cross section. Figure 3.3b shows the cross section analysis for both films where $Q = 1.1 \times 10^{-14}$ cm^{-2} for β-$NaSn_{13}$ and $Q = 1.7 \times 10^{-14}$ cm^{-2} for Sn_{12}. The cross section value Q represents the amount of desorption that occurs for a given area with each incident electron. The value is denoted as an "effective" desorption cross section due to the numerous additional events that can lead to desorption during e^- irradiation, like thermal excitation or radical abstraction, which are not accounted for. Obtaining this value is significantly useful in comparisons between materials or ambients.

Finally, we obtained XPS for both films to further characterize both materials. Figure 3.4 shows the spectra for C 1s (a), O 1s (b), Sn 3d (c), and Na 1s (d) core level transitions. The C 1s spectra was fit with three peaks for the β-$NaSn_{13}$, specifically C-H (E_b = 284.8 eV) C-O (E_b = 286.3 eV) and C=O (E_b = 288.6 eV).[53] Only two peaks were needed for Sn_{12}, where the C-O peak is absent since Sn_{12} has no methoxyl ligands like β-$NaSn_{13}$. Neither films should contain any C=O in the film, but this is due to contamination from exposure to atmosphere during spin coating. The O 1s spectra was fit with two peaks for both precursors, with O-Sn (E_b = 530.4 eV) and O-H (E_b = 532.0 eV).[53,74] There are O-C species present in the β-$NaSn_{13}$, as shown by the C 1s spectra, however the O 1s binding energy is difficult to distinguish from the O-H groups.[53] Therefore the higher binding energy peak for β-$NaSn_{13}$ is denoted O-C/O-H. The Sn 3d spectra is fit with two peaks representing the Sn $3d_{5/2}$ (E_b = 486.6 eV) and Sn $3d_{3/2}$ (E_b = 495.0 eV) spin-orbit splitting.[53,74,75] No noticeable differences are seen in the Sn

3d spectra for either film. Na is only present in the β-$NaSn_{13}$, as it serves to template the cluster.[67] The Na 1s in β-$NaSn_{13}$ was fit using one peak (E_b = 1072.2 eV). The Sn MNN Auger spectra were also collected for both films and show two peaks representing $M_4N_{45}N_{45}$ (E_{kin} = 432 eV) and $M_5N_{45}N_{45}$ (E_{kin} = 424 eV). Due to close energy values of peaks for the Sn^{2+} and Sn^{4+} oxidation states, Auger spectra is required to truly determine the oxidation state.[74] The Auger parameter is calculated by adding the binding energy of Sn $3d_{5/2}$ to the kinetic energy of Sn $M_4N_{45}N_{45}$, where we obtain 918.5 eV for Sn_{12} and 918.6 eV for β-$NaSn_{13}$. This is consistent with expected value for Sn^{4+} (918.3−918.4 eV) as opposed to Sn^{2+} (919.7 eV) or Sn metal (922.0−922.4 eV).[53,75]

We have also calculated atomic concentrations for both films using the XPS data. Calculated At % values are presented in Table 3.2 along with the theoretically calculated values from the crystal structure of both precursors. The ratio of C-H:C-O is much higher than the theoretical value for β-$NaSn_{13}$ primarily due to the presence of adventitious carbon. Adsorbed water is also likely due to the increase in O-H seen in β-$NaSn_{13}$. Due to the inability to focus on multiple spots on the sample with a dual anode source, there is likely some desorption that has occurred during the scan length. Using a monochromated source instead with the ability to obtain spectra on fresh locations for each transition would provide more accurate atomic composition data. This is evident as the Sn % is larger than theoretically expected, suggesting some desorption has already occurred.

Ultimately, this information paves the way for future studies. The primary goal is to be able to understand the chemical mechanisms that occur through EUV exposure.

But this can only be done after a baseline of data and standardized measurements are obtained and tested for repeatability. As more materials are synthesized moving forward, it is important to have a benchmark in place and reliable methods to compare to prior materials. Due to the film uniformity and stability of the β-$NaSn_{13}$ shown in this chapter, further studies were carried out using the β-$NaSn_{13}$. The focus of Chapters 4 and 5 is to better understand the chemical transition taking place leading to a change in solubility through photon exposure.

3.5 CONCLUSIONS

We have characterized the Sn_{12} dodecamer and β-$NaSn_{13}$ Keggin precursors as model photoresists for EUV lithography. AFM data shows that the β-$NaSn_{13}$ forms a smooth film with low roughness, while the Sn_{12} agglomerates on the surface following deposition, creating pinholes in the film. This suggests the Sn_{12} requires some improvements in film quality before it can be reliably used as a photoresist. TPD data for both clusters were similar and indicated that there were two main desorption events; water desorption (350 K) and butyl desorption (690 K). Calculated desorption energies were identical for both on the range of 2.5-3 eV, correlating to the cleavage of butyl ligands bonded to Sn. Thus, the thermal stability of the film is directly related to the butyl-tin bond strength. Both films are stable at temperatures well above standard industrial baking temperatures. ESD demonstrated low energy electrons can induce butyl desorption. Calculated ESD cross sections provide a benchmark for assessing the radiation sensitivity of organotin resist materials. XPS results indicated the oxidation

state of the Sn through Auger parameter analysis and verified the chemical composition for both materials following film deposition.

3.6 ACKNOWLEDGEMENTS

This research is supported by the Center for Sustainable Materials Chemistry, US National Science Foundation (grant number CHE-1102637), and the Semiconductor Research Corporation (contract number 2013-OJ-2438.001). We thank Eric Garfunkel and Feixiang Luo for insightful conversations related to XPS analysis of organotin compounds. Also, we thank David Marsh and Danielle Hutchison for their help with synthesizing the precursor material.

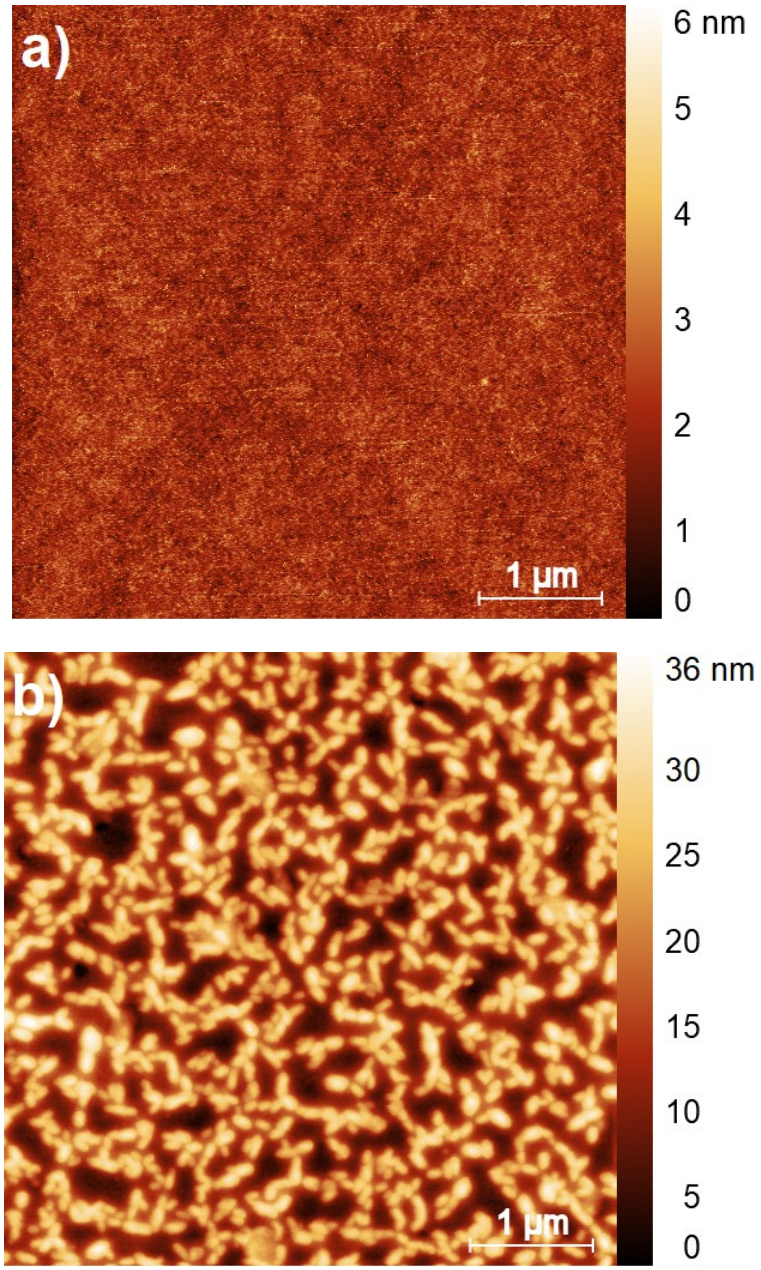

Figure 3.1. AFM images for 5x5 µm scans of β-$NaSn_{13}$ Keggin (a) and Sn_{12} Football (b) organotin precursors.

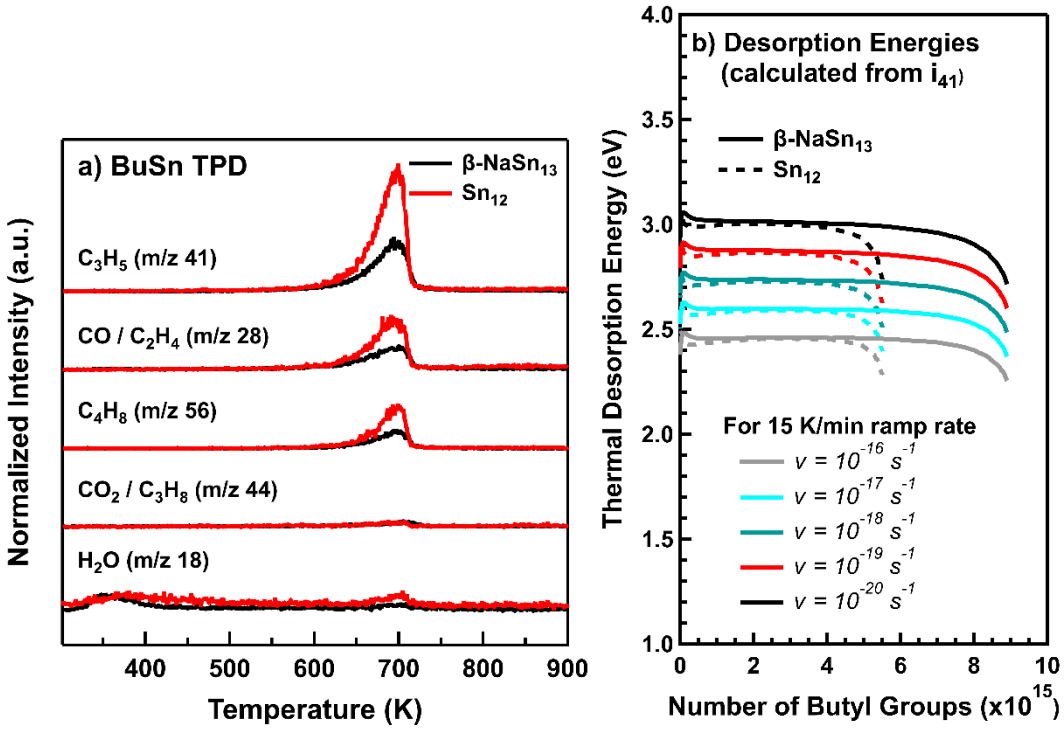

Figure 3.2. TPD studies showing the primary mass profiles (a) and the inversion analysis to calculate a thermal desorption energy for a range of pre-factors (b) for both the β-$NaSn_{13}$ Keggin and Sn_{12} Football precursors.

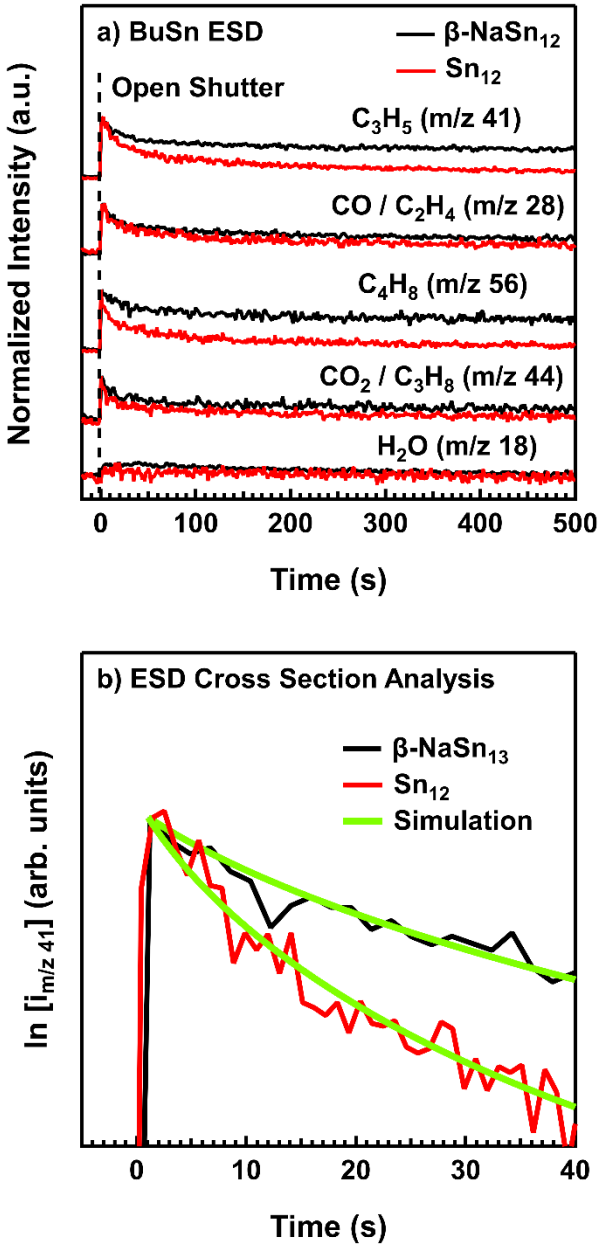

Figure 3.3. ESD studies showing the primary mass profiles (a) and the desorption cross section analysis using Gaussian beam simulations (b) for both the β-$NaSn_{13}$ Keggin and Sn_{12} Football precursors.

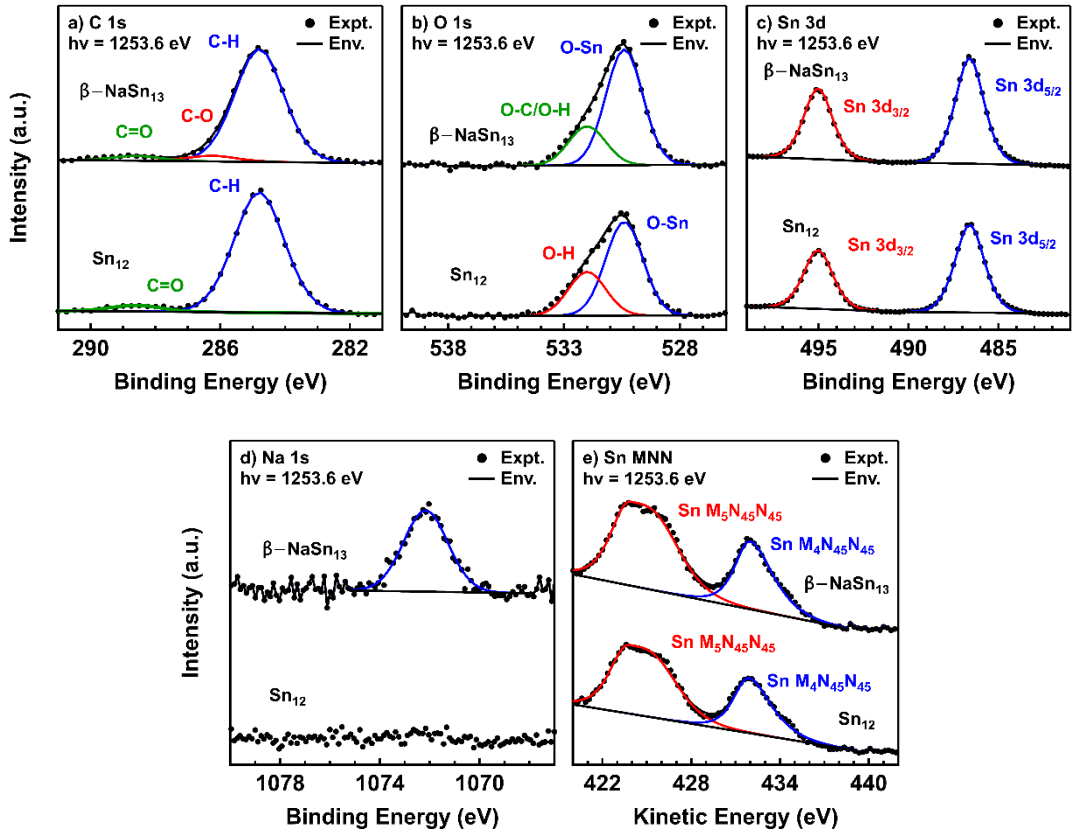

Figure 3.4. XPS characterization of both the β-$NaSn_{13}$ Keggin and Sn_{12} Football precursors, comparing C 1s, O 1s, Sn 3d, Na 1s, and Sn MNN Auger spectra using Mg Kα dual anode X-ray source.

Table 3.1. Ellipsometry thickness measurements for the β-$NaSn_{13}$ Keggin and Sn_{12} Football precursors spin coated as thin films.

Precursor	**Average Thickness (nm)**	**Average MSE**
β-$NaSn_{13}$	20.8	14.8
Sn_{12}	22.8	28.1

Table 3.2. XPS atomic percent calculations for the β-$NaSn_{13}$ Keggin and Sn_{12} dodecamer precursors. The Auger parameter is also calculated from the Sn $M_4N_{45}N_{45}$ kinetic energy.

	Sn_{12} Measured	**Sn_{12} Theoretical**	**β-$NaSn_{13}$ Measured**	**β-$NaSn_{13}$ Theoretical**
Element	**Atomic %**	**Atomic %**	**Atomic %**	**Atomic %**
Sn	**17 %**	**15 %**	**19 %**	**13 %**
C (Total)	**56 %**	**59 %**	**50 %**	**58 %**
C-H	53 %	59 %	46 %	47 %
C-O	0 %	0 %	2.3 %	11 %
C=O	2.7 %	0 %	1.9 %	0 %
O (Total)	**28 %**	**27 %**	**30 %**	**29 %**
O-Sn	19 %	17 %	22 %	24 %
O-C/O-H	8.9 %	10 %	7.5 %	5 %
Na	0 %	0 %	0.9 %	0 %
Sn $M_4N_{45}N_{45}$	431.9 eV		432.0 eV	
Auger Par.	918.5 eV		918.6 eV	

CHAPTER 4:

AMBIENT-PRESSURE XPS CHARACTERIZATION OF RADIATION INDUCED CHEMISTRIES OF ORGANOTIN CLUSTERS

J. Trey Diulus[1], Ryan T. Frederick[1], Mengjun Li[2], Danielle C. Hutchison[3], Morgan R. Olsen[3], Igor Lyubinetsky[1], Líney Árnadóttir[1], Eric L. Garfunkel[2], May Nyman[3], Hirohito Ogasawara[4], Gregory S. Herman[1,3*]

[1]School of Chemical, Biological and Environmental Engineering, Oregon State University, Corvallis, OR, 97331, USA

[2]Department of Chemistry and Chemical Biology, Rutgers University, Piscataway, NJ 08854, USA

[3]Department of Chemistry, Oregon State University, Corvallis, OR, 97331, USA

[4]SLAC National Accelerator Laboratory, Menlo Park, CA 94025 USA.

*Corresponding Author

Reprinted with permission from ACS Appl. Mater. Interfaces, vol. 11, issue 2, pp. 2526-2534, 2018.

4.1 ABSTRACT

Advances in extreme ultraviolet (EUV) photolithography requires the development of next-generation resists that allow high-volume nanomanufacturing with single nanometer patterning resolution. Organotin-based photoresists have demonstrated nanopatterning with high-resolution, high sensitivity, and low line edge roughness. However, very little is known regarding the detailed reaction mechanisms that lead to radiation-induced solubility transitions. In this study, we investigate the interaction of soft X-ray radiation with organotin clusters to better understand radiation-induced chemistries associated with EUV lithography. Butyltin Keggin clusters (β-$NaSn_{13}$) were used as a model organotin photoresist and characterization was performed using near ambient-pressure X-ray photoelectron spectroscopy (NAPXPS). The changes in relative atomic concentrations and associated chemical states in β-$NaSn_{13}$ resists were evaluated after exposure to radiation for a range of ambient conditions and photon energies. A significant reduction in the C 1s signal versus exposure time was observed, which corresponds to the radiation-induced homolytic cleavage of the butyltin bond in the β-$NaSn_{13}$ clusters. To improve resist sensitivity we evaluated the effect of oxygen partial pressure during radiation exposures. We found that both photon energy and oxygen partial pressure had a strong influence on the butyl group desorption rate. These studies advance the understanding of radiation induced processes in β-$NaSn_{13}$ photoresists and provide mechanistic insights for EUV photolithography.

4.2 INTRODUCTION

During the EUV photolithography process, the absorption of relatively high energy EUV photons results in the emission of photo- and Auger electrons, which inelastically scatter and result secondary electrons. Recent studies have indicated that low kinetic energy electrons are the active radiation species in EUV patterning,[8] and ultimately drive photoresist chemistries.[47,45,76,77] Electron stimulated desorption studies have found that the interaction of low energy electrons with butyltin hydroxide oxide hydrate resulted in desorption of the butyl ligand with fairly high cross sections, which is consistent with homolytic cleavage of the butyl-tin bond.[5,45] For organotin compounds the EUV photosensitivity can be inversely correlated with the C-H bond dissociation energies for phenyl, butyl and benzyl groups,[34] where the C-H bond dissociation energies were used to approximate trends in the C-Sn bond dissociation energies. Higher EUV photosensitivities were obtained for weaker C-H bond dissociation energies, which suggests that the homolytic cleavage of the C-Sn bond occurs during EUV exposure for organotin photoresists.

Another factor that influences organotin resist properties is the ambient during radiation exposure. Studies have shown that DUV exposures of organotin cage photoresists in various ambients resulted in significant carbon loss compared to unexposed films.[7] The carbon loss was correlated with cleavage of the butyl-tin bond. DUV exposures in air significantly decreased the amount of carbon compared to DUV exposures in N_2, but also increased the amount of oxygen incorporated in the film.[7] A major concern for EUV lithography is mirror contamination in EUV steppers by a range of species that can reduce the mirrors reflectivity. Prior studies have investigated

methods to minimize carbon contamination on the mirrors through the reactions of hydrocarbons with EUV radiation.[78,79] Low pressures of O_2 (~$1x10^{-4}$ Torr) were shown to successfully decreases the amount of carbon deposition.[78]

A more significant concern is Sn contamination on the mirrors from the EUV radiation sources (i.e., ablation of tin droplets). To minimize Sn contamination current EUV steppers operate with a hydrogen ambient. This results in the formation of volatile SnH_4 that then desorbs form the mirrors.[80,81] The interaction of metal containing resists with EUV radiation and the hydrogen ambient can lead to the formation of volatile metal hydrides from the resists that can further contaminate the EUV mirrors.[72] Based on the concern for resist outgassing ASML has introduced a dynamic gas lock (DGL) membrane for EUV steppers.[82] The DGL membrane is located between the projection optics and the wafer stage. A secondary benefit of the DGL technology is that it allows ambient conditions at the wafer stage to be modified to potentially improve photoresist performance while not effecting the projection optics. Obtaining a more complete understanding of radiation induced mechanisms in organotin photoresists, and the role of ambient environments during exposures, will potentially allow the design of more efficient EUV photoresists and can ultimately lead to improvements in EUV photolithography.[35]

In this study, we evaluated the effect of the X-ray photon energy and O_2 partial pressures on the radiation induced chemistries for β-$NaSn_{13}$ photoresists. We have used X-ray absorption spectroscopy (XAS) to measure the electron yield with respect to the X-ray photon energy and near ambient-pressure X-ray photoelectron spectroscopy

(NAPXPS) to perform *operando* characterization of the chemical and compositional changes with respect to exposure time, photon energy, and O_2 partial pressure.

4.3 EXPERIMENTAL

The β-$NaSn_{13}$ clusters were synthesized by a procedure described previously.[67] Si substrates (< 0.0055 Ω-cm) were prepared by rinsing with acetone, 2-propanol and deionized water, followed by etching the native oxide with hydrofluoric acid (48-51% ACS grade, VWR, diluted 1:5 with water) for two minutes. The substrates were immediately loaded into a VEECO 7700 Series thermal evaporator and pumped down to a base pressure of $1x10^{-6}$ Torr. Manganese chips (99.95%, KJ Lesker) were used to thermally evaporate ~100 nm Mn thin films onto the substrate. Mn film thickness was verified using a quartz crystal microbalance and profilometry.

Hexamethyldisilazane (HMDS) (99.2%, MP Biomedicals) was spin coated onto the Mn films to form a hydrophobic surface and improve cluster adhesion and film uniformity. The HMDS was puddled on the substrate for approximately 30 seconds and then spin dried at 3000 RPM for 30 seconds. To form the precursor solution, 20 mg/mL of β-$NaSn_{13}$ clusters were dissolved in 2-heptanone (99%, VWR) and mixed via ultra-sonication for five minutes to make a 90 mM (Sn-basis) solution. The β-$NaSn_{13}$ cluster solution was filtered through 0.45 μm PTFE syringe filter and puddled onto the substrate. A thin film was obtained by spin-coating at 3000 RPM for 30 seconds. Samples were then annealed at 70 °C for 3 min in air to remove residual solvent. Each substrate was cleaved into 5x10 mm^2 coupons for sample mounting.

Atomic force microcopy has indicated that similar procedures provide uniform films with low roughness[67] and spectroscopic ellipsometry has indicated that the films are ~20 nm thick.[77] Rutherford backscattering spectroscopy (RBS) analysis was performed on these films to determine the number of Sn atoms present in the film. RBS was performed using a 2 MeV He^+ beam from a 1.7 MV tandem accelerator and an ion current of 2-3 nA. Data fitting and modeling were performed using the SIMNRA 6.06 software package. These results indicate that there are $1.0x10^{16}$ Sn/cm^2.

NAPXPS and XAS were performed using beam line 13-2 at the Stanford Synchrotron Radiation Lightsource (SSRL). The endstation features a vacuum chamber with a differentially pumped electron spectrometer (VG-Scienta, SES-100) connected to an ambient-pressure gas cell. With this endstation NAPXPS can be performed for pressures up to approximately 10 Torr.[83] The distance between the sample and the beamline window was 10 mm. The beamline has an energy range of $h\nu$ = 180-1450 eV with a resolving energy of $E/\Delta E > 5000$.[83] The beamline uses a spherical grating monochromator along with Kirkpatrick-Baez focusing mirrors to obtain a spot size of 0.01x0.075 mm^2 and a flux between 10^{11}-10^{12} photons/second.[83] For NAPXPS and XAS experiments we used $h\nu$ = 472-640 eV and a 600 l/mm Ni coated grating.

Two separate mounting procedures were used for NAPXPS and XAS. For NAPXPS, two 5x10 mm^2 samples were mounted side-by-side by spot welding strips of Ta foil over the corners of the sample. For XAS, two 5x10 mm^2 samples were mounted side-by-side using double sided conductive carbon tape on top of the Ta foil. For both cases, the Ta foil sample holder was mounted to the translation arm using a 1 mm diameter platinum-rhodium alloy ($Pt_{87}Rh_{13}$) wire. After loading the samples, the

system was pumped down overnight to a pressure of $<1x10^{-9}$ Torr. The ambient-pressure gas cell was connected to a gas manifold containing an ultra-high purity O_2 lecture bottle (99.999% Purity Research Grade, Airgas). A high-precision variable leak valve (Vacuum Generators) was used to introduce and control the O_2 pressure in the ambient-pressure gas cell. A residual gas analyzer (RGA200, Stanford Research Systems) was used to obtain background mass spectra in order to ensure no other impurity gasses during dosing. XAS was performed for the Sn $M_{4,5}$, O K, and Mn L_3 absorption edges, where $h\nu$ was scanned from 480 to 640 eV with a 0.2 eV step size. The partial electron yield (PEY) was obtained by measuring the Sn MNN Auger electron intensity and the total electron yield (TEY) was obtained by measuring the sample current. The photon energy was further calibrated by measuring the kinetic energy of the C 1s peak at each photon energy.

NAPXPS spectra were collected from the β-$NaSn_{13}$ thin films at several photon energies and ambient conditions. For a typical set of experiments six C 1s spectra were obtained sequentially at a given photon energy ($h\nu$ = 472, 510, 530 and 626 eV). After these measurements a reference set of C 1s, O 1s, and Sn 3d spectra were obtained using $h\nu$ = 626 eV. Alternatively, six O 1s spectra were obtained sequentially using $h\nu$ = 626 eV, followed by a reference set of C 1s, O 1s, and Sn 3d spectra at $h\nu$ = 626 eV. Each series of spectra were performed at new sample locations by using a piezo drive to move the sample ~10 μm. This NAPXPS procedure was performed in UHV and at $P_{O_2} = 0.01$ and 1 Torr. The collection time interval in successive scans was set by the length of time required for the collection of one scan. The C 1s, O 1s, and Sn 3d spectra

were obtained using a 200 eV analyzer pass energy, 0.1 eV step size, 267 ms/step, and one sweep. All NAPXPS spectra were charge corrected to the aliphatic C 1s binding energy (E_b) at 284.8 eV.[53] The NAPXPS spectra were fit with CasaXPS, using Gaussian-Lorentzian line shapes and a linear background. We found that the amount of charge compensation varied between ambient conditions and photon energies and we therefore allowed the full width half maximum (FWHM) values of the fitted peak components to vary by $\pm$0.1 eV. The NAPXPS spectra were normalized to account for changes in flux from the beamline by using the average of the background intensity at low binding energies. This was done by averaging the intensities of three separate 1 eV energy windows shifted 0.5 eV apart below the main photoemission peak being analyzed. This normalization procedure additionally allowed us to assess the error with respect to the background noise. The film atomic concentrations (At%) were obtained by calculating relative sensitivity factors based on the known chemical composition of the β-$NaSn_{13}$ clusters (i.e., 13 At% Sn, 58 At% C, and 29 At% O).[77] The spectra obtained following exposure at 626 eV in UHV was used to estimate the sensitivity factors. The same factors were then applied to the spectra for other experimental conditions. In an XPS system with well quantified sensitivity factors we obtained At% for the β-$NaSn_{13}$ thin films that match the expected chemical composition.[77]

To estimate the photon dose during spectral acquisition we divided the beamline photon flux by the X-ray spot area, which resulted in 4.1×10^{15} photons/cm^2/s. The time to obtain C 1s, O 1s, or Sn 3d spectra was 420, 540 or 540 seconds, respectively. For the C 1s and O 1s series, the total exposure times were 2940 or 3780 seconds, corresponding to photon doses of ~1.2×10^{19} and ~1.6×10^{19} photons/cm^2, respectively.

4.4 RESULTS AND DISCUSSION

The interaction of low kinetic energy electrons with organotin photoresists drives much of the radiation-induced chemistries that lead to the required solubility transition. To better correlate the relative number of electrons at various photon energies for the NAPXPS experiments we have performed XAS. In Figure 4.1 we show the TEY XAS data from the β-$NaSn_{13}$ films, which were obtained for $h\nu$ = 480-640 eV. We have indicated the location of the Sn $M_{4,5}$, O K, and Mn L_3 edges and the photon energies used for the NAPXPS experiments. We find that as the photon energy increases the background intensity of the TEY also increases. The Sn M_5 and M_4 edges were located at 486.8 and 494.8 eV, respectively, which correspond well with values obtained for SnO_2 aerogels.[74,84] The O K edge was located at 531.2 eV, but also contains a significant pre-edge feature starting at 520.2 eV as well as multiple peaks extending from 535-600 eV. The pre-edge at 520.2 eV is due to an increase in the Sn 3d photoionization cross section where there is a maximum ~40 eV above the $M_{4,5}$ edges.[33] The peaks between 535-600 eV are from constructive and destructive interference due to multiple scattering from near neighbor atoms in the cluster.[85] It is important to note that radiation induced chemical changes in the cluster are expected to occur during the collection of the XAS data, which may result in changes to the edge energies and relative intensities.

To evaluate the effect of the photoelectron-emitting atom on radiation induced chemistries in β-$NaSn_{13}$ films, we have used photon energies either below, at, or above the absorption edges of Sn and O. We have also considered the role that the TEY has

on the radiation chemistries in the β-$NaSn_{13}$ films. For the four photon energies used in the NAPXPS experiments we can evaluate the TEY and the primary atomic origin of the electrons. At $h\nu$ = 472 eV, which is below both the Sn $M_{4,5}$ and O K edges, we have the lowest total absorption leading to a low TEY. At $h\nu$ = 510 eV, which is just above the Sn $M_{4,5}$ edge, we have increased the TEY. At $h\nu$ = 530 eV, which is on the O K edge, we have further increased the TEY. At $h\nu$ = 626 eV, which is above both the Sn $M_{4,5}$ and O K edges, we have the highest TEY. Compared to the TEY at $h\nu$ = 472 eV we find that the TEY for $h\nu$ = 510, 530, and 626 eV increase by factors of 1.6, 2.1, and 3.5, respectively.

To further evaluate radiation induced chemistries we have obtained NAPXPS data for $h\nu$ = 472, 510, 530, and 626 eV and for UHV, P_{O_2}= 0.01, and P_{O_2}= 1 Torr. The goal of adding oxygen during exposure is to determine if oxygen adsorbed in the film can result in the formation of reactive oxygen intermediates that can increase the rate of butyl ligand loss from the resists.[7,77] Based on mechanisms where the loss of the butyl group is necessary to form an insoluble film the incorporation of oxygen may potentially increase the sensitivity of the EUV photoresists.[86] In Figure 4.2 (a-c) we show C 1s, O 1s, and Sn 3d spectra, respectively, obtained at $h\nu$ = 626 eV in UHV and P_{O_2}= 1 Torr. The spectra are stacked for clarity and are normalized using the procedure described above. The signal to noise ratios in the spectra decreases with increasing O_2 pressure due to the additional inelastic attenuation of electrons in the gas phase at higher O_2 pressures.

In Figure 4.2a we show the C 1s spectra fit with three peaks at E_b = 284.8, 286.8, and 288.9 eV. These binding energies correspond to C-H, C-O, and C=O, respectively.[53] The most intense peaks at E_b = 284.8 and 286.8 eV can be correlated to the twelve butyl and methoxy ligands, respectively, that are coordinated to the β-$NaSn_{13}$ cluster.[53,87] The peak at E_b = 288.9 eV is likely due to contamination from exposure to the atmosphere.[53] Adventitious carbon may also be present due to exposure to the atmosphere, which could lead to an error in determining the film specific sensitivity factor.[53]

In Figure 4.2b we show the O 1s spectra fit with two peaks at E_b = 530.5 and 532.0 eV. These binding energies correspond to tin oxide and either methoxy or hydroxyl ligands, respectively.[75,87,88,89] Adsorbed organic carbonates (based on C 1s spectra) and water are also expected as potential contaminates. Unfortunately, the binding energies of these potential contaminates are similar to the values expected for methoxy or hydroxyl ligands, which makes it difficult to quantify the amount of contaminants.[74] Therefore, in the discussions below the O 1s components will be primarily identified as tin oxide (E_b = 530.5 eV, O-Sn) and methoxy/hydroxyls (E_b = 532.0 eV, O-C/O-H). The O 1s spectra obtained at P_{O_2}= 1 Torr also has peaks at E_b = 537.8 and 538.8 eV which correspond to the gas phase O_2 doublet.[90]

In Figure 4.2c we show the Sn 3d spectra fit to two peaks at E_b = 486.6 and 495.0 eV, which correspond to the Sn $3d_{5/2}$ and $3d_{3/2}$ spin-orbit split doublet. These binding energies are consistent with either Sn^{2+} or Sn^{4+}.[74,75,88,89,] Based on a prior Auger parameter analysis of these β-$NaSn_{13}$ clusters, we have determined that the oxidation

state is Sn^{4+}, which is consistent with the molecular formula and structure of the β-$NaSn_{13}$ cluster.[77]

To assess changes in the β-$NaSn_{13}$ films in different ambient conditions for increasing exposure times and different photon energies, we have fit the sequential C 1s and O 1s spectra using the procedure described above. Figure 4.3 shows NAPXPS spectra obtained with $h\nu$ = 626 eV. Figure 4.3 (a,b) show the C 1s spectra obtained at UHV and P_{O_2}= 1 Torr, respectively, while Figure 4.3 (c,d) show the O 1s spectra obtained at UHV and P_{O_2}= 1 Torr, respectively. The X-ray exposure time is indicted in the figures and corresponds to the time at the midpoint of the spectrum. The C1s and O 1s spectra labeled 3.5 and 4.5 minutes, respectively, were obtained immediately after the sample was moved to a new location. The other spectra were obtained at the indicated times. We found that the C 1s spectra obtained in UHV (Figure 4.3a) do not change significantly even after a 38.5 min radiation exposure. However, the C 1s spectra obtained in P_{O_2}= 1 Torr (Figure 4.3b) significantly decreased in intensity for the C-H component, while the intensity for the C-O and C=O components stayed approximately the same as the initial spectrum. As shown in Figure 4.3 (c,d), only minor changes were observed for the O 1s spectra whether the data were obtained in UHV or P_{O_2}= 1 Torr or for longer exposure times.

To better quantify the changes in the spectra shown in Figure 4.3, we have plotted peak intensity ratios with respect to X-ray exposure time. In Figure 4.4 (a-c) we show the intensity ratio of the C-H component for each spectrum divided by the C-H component from the initial spectrum with respect to X-ray exposure time. Plotting the

data in this manner highlights the relative changes in intensity during the X-ray exposure at each photon energy and ambient condition. In Figure 4.4a, we show the C-H intensity ratio versus X-ray exposure time for four different photon energies in UHV. For these data very little change in the C-H intensity ratio was observed where the maximum decrease was ~0.10 compared to the original C-H intensity ratio. In Figure 4.4b we show changes in the C-H intensity ratio versus X-ray exposure time for four different photon energies at P_{O_2}= 0.01 Torr. We find that there was a significant decrease in the C-H intensity ratio compared to the UHV data and that the decrease has a photon energy dependence. The maximum decrease in the C-H intensity ratio was ~0.37 compared to the original C-H intensity ratio. In Figure 4.4c, we show changes in the C-H intensity ratio versus X-ray exposure time for four different photon energies at P_{O_2}= 1 Torr. An even higher decrease in C-H intensity ratio (~0.52) was observed at this pressure. Again, the rate of decrease in the C-H intensity ratio was found to have a photon energy dependence.

The main path for the reduction in the C 1s intensity ratio is through the homolytic cleavage of the C-Sn bond, which leads to the loss of butyl ligands from the cluster.[5,45] Assuming that the observed reduction in the C 1s intensity correlates to the desorption of butyl ligands we can apply an exponential photon stimulated desorption (PSD) model to fit the data.[91] For this analysis, the coverage of the radiation sensitive ligand with respect to photon exposure time can be determined using Eq. 4.1:

$$I(t) = I_0 \exp[-\sigma\varphi t] + I_\infty \qquad \text{(Eq. 4.1)}$$

Where $I(t)$ is the peak intensity of the radiation sensitive ligand at time t, σ is the desorption cross section in cm^2, φ is the photon flux in photons/cm^2/s, I_∞ is the peak intensity of the radiation sensitive ligand at t = ∞, and I_0 is the peak intensity of the radiation sensitive ligand at t = 0. At t = 0 Eq. 4.1 simplifies to $I_0 = I(t=0) + I_\infty$ and can be normalized by dividing by $(I_0 + I_\infty)$ to obtain Eq. 4.2:

$$y(t) = A\exp[-\sigma\varphi t] + y_\infty \qquad \text{(Eq. 4.2)}$$

Where $y(t)$ is the peak intensity ratio of the radiation sensitive ligand at time t, y_∞ is the peak intensity ratio at t = ∞, and $A = 1 - y_\infty$. This model allows for a quantitative comparison of the change in the C 1s signal for each experimental condition, which we correlate to the loss of the butyl ligands.

The lines shown in Figure 4.4 (b,c) are based on the results of Eq. 4.2. By fitting the data to an exponential model and dividing the constant in the exponential term by the photon flux we can obtain σ. The absorption of incident X-rays results in the emission of photoelectrons, Auger electrons, secondary, and thermal electrons. It is these electrons that lead to the ligand desorption observed in our experiments. As a result the cross section includes the absorption of the incident X-rays and the emission of electrons by any atom in the cluster and not just a specific atom. However, by varying the photon energy we can enhance the relative X-ray absorption for specific elements. For P_{O_2}= 0.01 and 1 Torr, we find that σ ranges from $8\text{x}10^{-18}$ to $4\text{x}10^{-17}$ cm^2 where the lowest value was found for $h\nu$ = 472 eV at P_{O_2}= 0.01 Torr and the highest value was found for $h\nu$ = 510 eV at P_{O_2}= 1 Torr. Exponential fits were only used for fitting the C-H intensity ratio in P_{O_2}= 0.01 and 1 Torr. A linear model was used to fit the C-H

intensity ratio in UHV and is included in Figure 4a to provide a visual representation of the relative changes.

The calculated values for y_∞ were between 0.48 to 0.8, which indicates that up to half of the aliphatic carbon desorbed during the longest X-ray exposures. For the C 1s spectra obtained in P_{O_2}= 1 Torr there was also a slight increase in C-O and C=O, which suggests that some of the remaining carbon species were oxidized in the oxygen ambient. We found that a solubility change occurred after developing the β-$NaSn_{13}$ after the extended X-ray exposures used to collect the data in Figure 4.1(a-d) and even for X-ray exposures performed in UHV. It is likely that the beamline provides sufficient X-ray flux to cause radiation induced changes very rapidly in the films, which ultimately results in the formation of an insoluble product.

As mentioned above, we have found that the C-H intensity ratio depends on both the ambient conditions and the photon energy. This suggests that both of these factors influence the rate of butyl ligand desorption from the β-$NaSn_{13}$ resists. We believe that ambient O_2 is adsorbed in the β-$NaSn_{13}$ resists and that reactive oxygen species form during inelastic scattering of the emitted and secondary electrons. For the expected electron kinetic energy range (< 90 eV) molecular oxygen has high cross sections for electronic excitations, ionization and dissociation, which can lead to the formation of reactive oxygen species.[92,93] A recent study has demonstrated that the introduction of an oxygen ambient during e-beam lithography allows the direct patterning of single- and bilayer graphene with a resolution better than 20 nm.[94] Due to the high resolution patterning that was obtained, the authors proposed that secondary

electrons produced during e-beam lithography led to the reactive oxygen species that etched the graphene.

In our studies the O_2 ambient provides two potential reaction pathways: the electrons emitted from the β-$NaSn_{13}$ resists can interact with O_2 adsorbed in the film, resulting in the formation of reactive oxygen species that preferentially interact with the butyl ligands; or the gas phase O_2 can absorb the X-rays, leading to electron emission in the gas phase, which would simultaneously reduce the X-ray flux at the β-$NaSn_{13}$ resist. An increase in the number of emitted electrons or the presence of reactive oxygen species is expected to result in a larger loss of butyl ligands from the β-$NaSn_{13}$ resist. To assess the total number of emitted electrons at a given photon energy we used the TEY XAS data from Figure 1. In Table 4.1 we provide normalized TEY for β-$NaSn_{13}$ films at each photon energy using the TEY at $h\nu$ = 472 eV. These data indicate that both $h\nu$ = 530 and 626 eV have much higher TEY than either $h\nu$ = 472 and 510 eV. For P_{O_2}= 0.01 Torr we find that $h\nu$ = 530 and 626 eV have the largest C-H loss, and these photon energies correspond to the highest TEY in Table 1. However, for P_{O_2}= 1 Torr we find that $h\nu$ = 626 eV still has the largest C-H loss, but $h\nu$ = 510 eV has a larger C-H loss compared to $h\nu$ = 530 eV. This may be due to an increase in the absorption of the photons by gas phase O_2 at the O K edge ($h\nu$ = 530 eV). To evaluate this we have calculated the expected X-ray attenuation at each photon energy compared to UHV and these results are also provided in Table 4.1. At P_{O_2}= 0.01 Torr this analysis indicates only minor X-ray attenuation at $h\nu$ = 626 eV, and effectively no attenuation at the other photon energies. However, at P_{O_2}= 1 Torr X-ray attenuation occurs for all

four photon energies. The largest decrease is observed for $h\nu$ = 626 eV, while the attenuation for $h\nu$ = 510 and 530 eV are essentially the same. Experimental gas phase X-ray absorption spectra for O_2 indicates that the main absorption transition occurs at $h\nu \sim 532$ eV.[95] If we modify our absorption cross sections for $h\nu$ = 530 eV by assuming we are on the main absorption transition of O_2 in the gas phase we can recalculate our X-ray attenuation. By doing this we find that the X-ray attenuation for $h\nu$ = 530 eV at P_{O_2}= 1 Torr is now 0.9881. This value is only slightly reduced compared to the estimates in Table 4.1. As such, we suggest that the X-ray attenuation at the different oxygen partial pressures should result in only a minor variation in the X-ray flux at the sample and does not explain the observed differences in C-H loss at the different photon energies.

To evaluate the effect that radiation exposure time has on the oxygen species in the β-$NaSn_{13}$ clusters we have performed an analysis similar to what was done for the C 1s data. We have calculated an O 1s intensity ratio by dividing the intensity of each O 1s spectrum by the intensity of the initial O 1s spectrum after the indicated X-ray exposure time. In Figure 4.4d, we show the O 1s intensity ratio obtained using $h\nu$ = 626 eV for β-$NaSn_{13}$ resists in UHV and at P_{O_2}= 0.01 and 1 Torr for different X-ray exposure times. The O 1s intensity ratio obtained in UHV decreased for longer X-ray exposure times, while the O 1s intensity ratio obtained in P_{O_2}= 0.01 and 1 Torr slightly increased for longer X-ray exposure times. We found that the O 1s intensity ratio obtained in UHV decreased by ~0.23, while the O 1s intensity ratio obtained in P_{O_2}= 0.01 and 1 Torr increased by ~0.05. The same PSD model described above was used

to fit the O 1s data obtained in UHV and is indicated by the solid black line. A linear model was used to fit the O 1s data obtained in P_{O_2}= 0.01 and 1 Torr and these are indicated by the solid blue and red lines, respectively.

To gain further insight into how the chemical composition of the β-$NaSn_{13}$ films change we have determined the At.% before and after X-ray exposures. In Figure 4.5 we show At.% for spectra obtained after a 42 minute X-ray exposure with $h\nu$ = 626 eV. It should be noted that similar results were obtained for $h\nu$ = 472, 510 and 530 eV. These results indicate only negligible changes for Sn At.% in UHV or as a function of P_{O_2}. This is expected since the likely Sn species are not expected to be volatile at room temperature. Furthermore, there was a significant reduction in the C At.% for increasing P_{O_2} compared to UHV, which is due primarily to the reduction in the C-H component. As already mentioned above a reduction in C-H component suggests the desorption of butyl ligands from the β-$NaSn_{13}$ films. Both the C-O and C=O components are found to increase with P_{O_2} compared to UHV, which indicates that some butyl ligands are oxidized during X-ray exposure in the presence of O_2 and these species remain in the film. There was only a negligible increase in the total O atomic concentrations for increasing P_{O_2} compared to UHV. We found that the O-Sn component increased when going from P_{O_2} = 0.01 to 1 Torr and that there was an increase in O-C/O-H at P_{O_2} = 0.01 Torr and a decrease at P_{O_2} = 1 Torr. The ratio of O-Sn:O-C/O-H also increases for higher P_{O_2}. When P_{O_2}= 1 Torr the conversion to SnO_2 is maximized and the O-C/O-H component makes up a much smaller portion of the total O 1s intensity. These results suggest we are increasing the rate at which β-$NaSn_{13}$

converts to SnO_2 through exposure to a higher ambient pressure of O_2. Furthermore, there is an increase in oxygenates on the surface which provides another route to Sn oxidation. These species could possibly act as intermediates during the reaction, which is why they make up a larger component of the film in the lower O_2 ambient pressure.

Figure 4.6 provides a visual representation of mechanisms that occur in the β-$NaSn_{13}$ resist when exposed to radiation in different ambient conditions. A portion of the β-$NaSn_{13}$ cluster is shown Figure 4.6a, and shows one Sn ion bound to structural oxygen and methoxy/hydroxyl groups. Figure 4.6 (a,b) illustrate that two different reaction pathways can occur during EUV exposure in UHV and P_{O_2}= 1 Torr, respectively. When the clusters absorb EUV radiation both photo- and Auger electrons are emitted from the atoms in the cluster. Inelastic scattering of these electrons leads to formation of both low energy secondary and thermal electrons. These electrons have enough kinetic energy to drive reactions that further modify the cluster chemistries. During this process, ambient oxygen molecules also interact with the emitted electrons leading to an increase in the number of reactive oxygen species that are formed.[77] The C-Sn bond is the weakest bond in the cluster[5] and butyl ligands undergo homolytic cleavage as shown in Figure 4.6d due to inelastic scattering of the electrons.[5] In UHV the only oxygen available to oxidize the Sn is from within the cluster. This process requires additional energy to break the bond between the hydrogen or methyl group and oxygen. The resulting O ion may form a double bond in order to restore charge neutrality. In an oxygen ambient three additional reaction pathways are possible. In Figure 4.6e, the reactive oxygen species can enhance the removal of methoxy/hydroxyl ligands which leads to an increase in the rate of conversion to SnO_2. In Figure 4.6f, the

reactive oxygen species can react directly with Sn, which results in oxidation without a change in coordination. In Figure 4.6g, reactive oxygen species can react with two Sn groups in adjacent clusters leading to Sn-O-Sn linking.

We find that removal of less than half of the butyl groups from the β-$NaSn_{13}$ cluster results in a change in solubility.[86] It is expected that further removal of butyl ligands or oxidation of Sn occurs during the development process which includes a 170 °C anneal in air and soaking in 2-heptanone. Further investigation of the composition following both the anneal and developer soak are necessary to obtain a complete understanding of the solubility transition mechanism.[50] By investigating ambient gasses with different oxidative strength we can also determine how they could be added during the EUV processes using a DGL membrane or how related species could be integrated into the resist to improve EUV sensitivity.

We have demonstrated that the addition of oxygen during β-$NaSn_{13}$ radiation exposure enhances the rate at which the cluster desorbs butyl groups. The addition of O_2 during EUV lithography may reduce the necessary dose to achieve the solubility transition, and thereby reduce the time required to pattern a wafer. This also likely holds true for other polyoxometallic nanocluster resists where the chemical mechanism relies on creating secondary and thermal electrons that result in homolytic bond cleavage through inelastic scattering. Further studies are still required to determine the mechanisms that take place through each step of the EUV lithography process. For our NAPXPS studies, the photon dose used (~$1x10^{19}$ photons/cm^2) is likely several orders of magnitude higher than the dose required to achieve the solubility transition. Performing similar experiments with a lower photon flux and EUV radiation should

provide further information on the distinct chemical changes occurring during EUV exposures.

4.5 CONCLUSIONS

Through this study we were able to show that carbon is removed from β-$NaSn_{13}$ during X-ray exposures and we were able to monitor radiation-induced changes in chemistry. The emitted and inelastically scattered electrons have enough kinetic energy to drive the homolytic cleavage of the Sn-C bond. We show that increasing electron yield due to increasing X-ray photon energy leads to a greater loss in carbon, which we correlate to the desorption of butyl ligands from the β-$NaSn_{13}$ cluster. The observed changes in the PSD cross sections with photon energy was closely related to the TEY as measured by XAS. An oxygen ambient resulted in a significantly higher rate for butyl group desorption, which we propose is due to the formation of reactive oxygen species through the interaction of O_2 with emitted electrons. Investigating the role gases play on the chemical mechanism allow for a better understanding of the chemistry taking place during radiation exposures. This study also suggests that introducing oxygen during radiation exposure may increase resist sensitivity and increase process efficiency.

4.6 ACKNOWLEDGEMENTS

This research was funded by the Semiconductor Research Corp. (SRC) Contract Number 2013-OJ-2438 and the Center for Sustainable Materials Chemistry

(CSMC) supported by the U.S. National Science Foundation under grant number CHE-1606982. This work was performed, in part, at the Northwest Nanotechnology Infrastructure, a member of the National Nanotechnology Coordinated Infrastructure, which is supported by the National Science Foundation under grant number NNCI-1542101. Use of the Stanford Synchrotron Radiation Lightsource, SLAC National Accelerator Laboratory, is supported by the U.S. Department of Energy, Office of Science, Office of Basic Energy Sciences under Contract No. DE-AC02-76SF00515.

We thank Dr. David Marsh and Prof. Darren Johnson for discussions on synthesizing organotin clusters, and Joe Bergevin for help with film characterization.

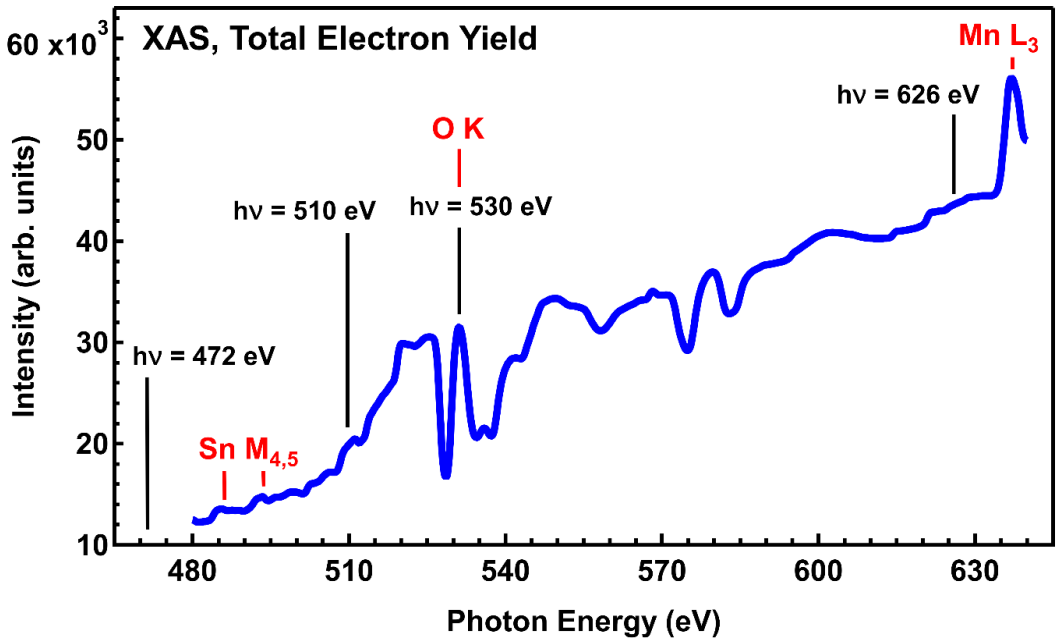

Figure 4.1. TEY XAS obtained from a β-NaSn13 film.

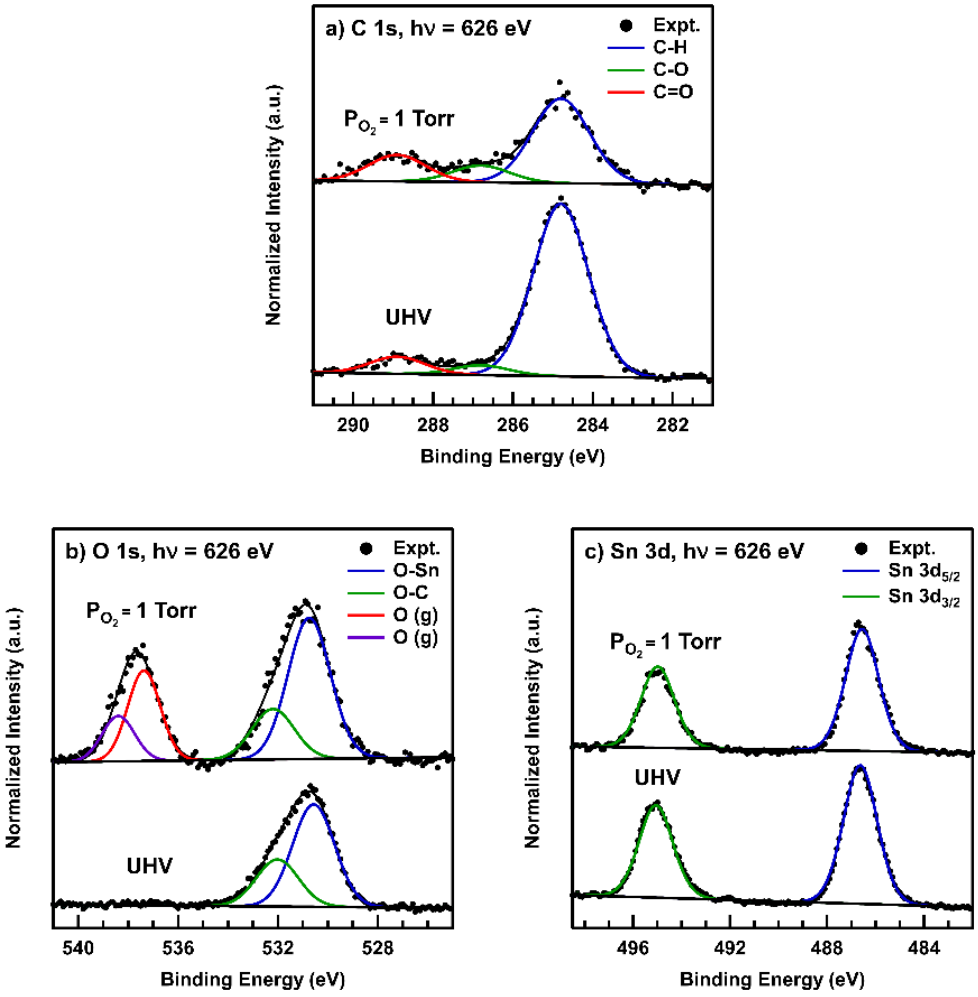

Figure 4.2. NAPXPS obtained for β-$NaSn_{13}$ in both UHV and $\boldsymbol{P_{O_2}}$ = 1 Torr using hν = 626 eV. (a) C 1s, (b) O 1s, and (c) Sn 3d core levels.

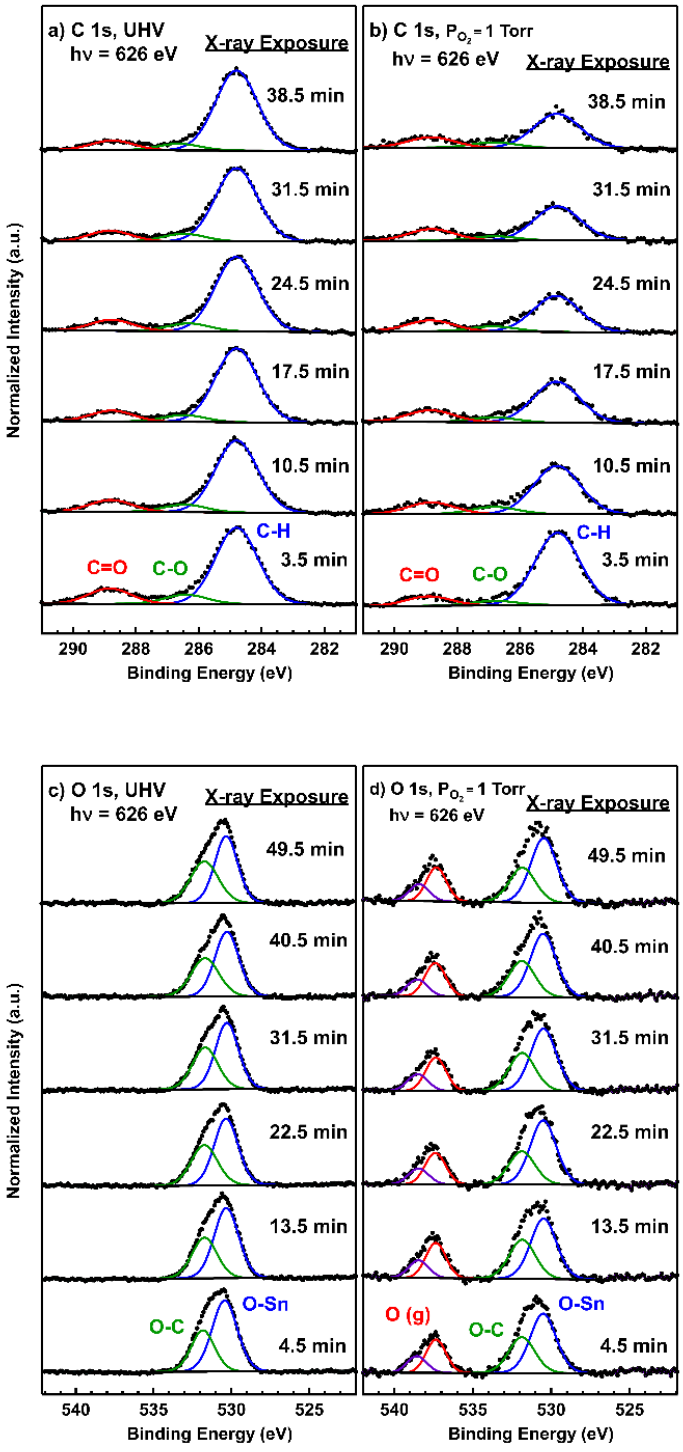

Figure 4.3. NAPXPS data obtained for different X-ray exposure times for C 1s in (a) UHV and (b) $\boldsymbol{P_{O_2}}$ = 1 Torr, and O 1s in (c) UHV and (d) $\boldsymbol{P_{O_2}}$ = 1 Torr.

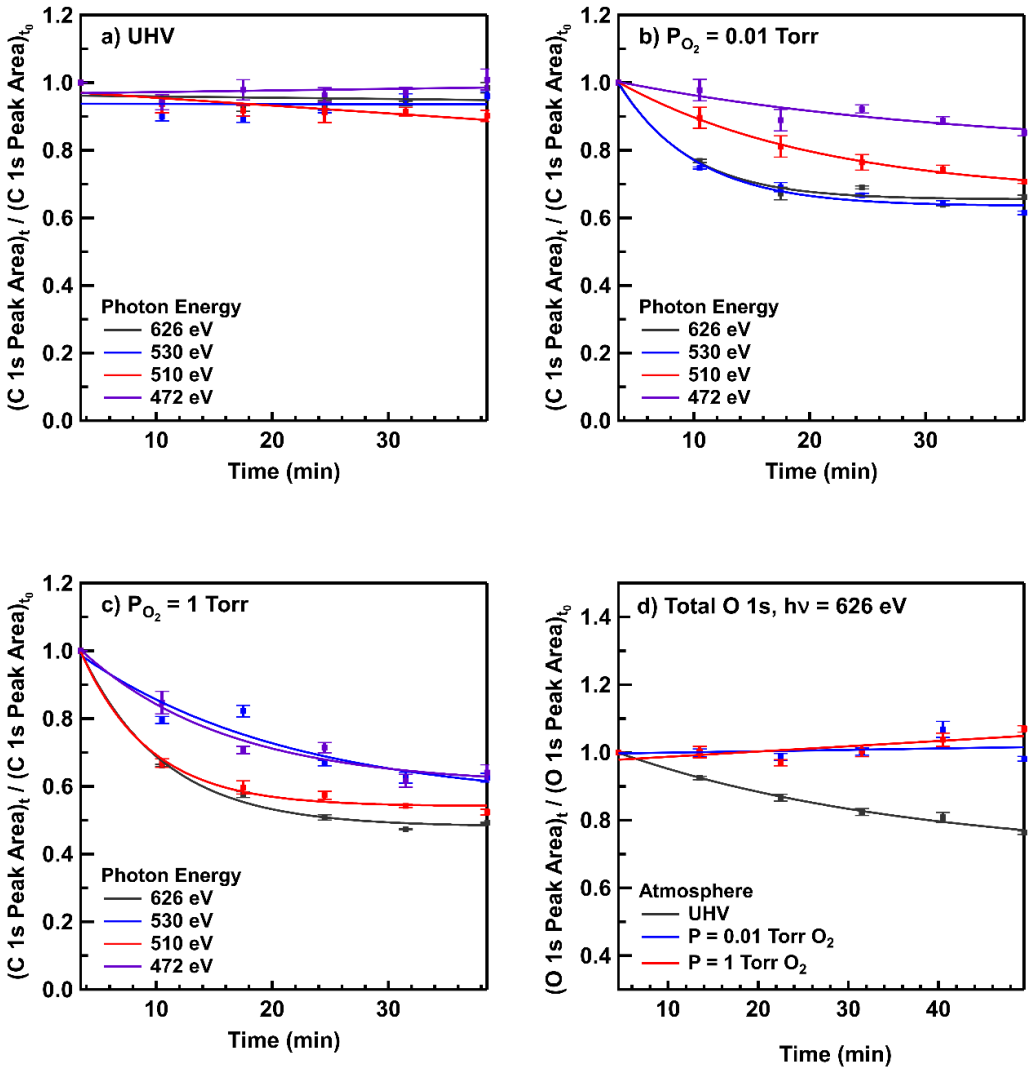

Figure 4.4. X-ray induced change in peak intensity ratios: C-H component of the C 1s spectra obtained in (a) UHV, (b) P_{O_2}= 0.01 Torr, (c) P_{O_2}= 1 Torr, and (d) Total O 1s spectra at hν = 626 eV for indicated oxygen pressures. The curves in the figure (b,c) are fits to equation 1, while the lines in figure (a) are fits to a linear function. In figure (d) the UHV data are fit to equation 1, while the ambient oxygen data are fits to a linear function.

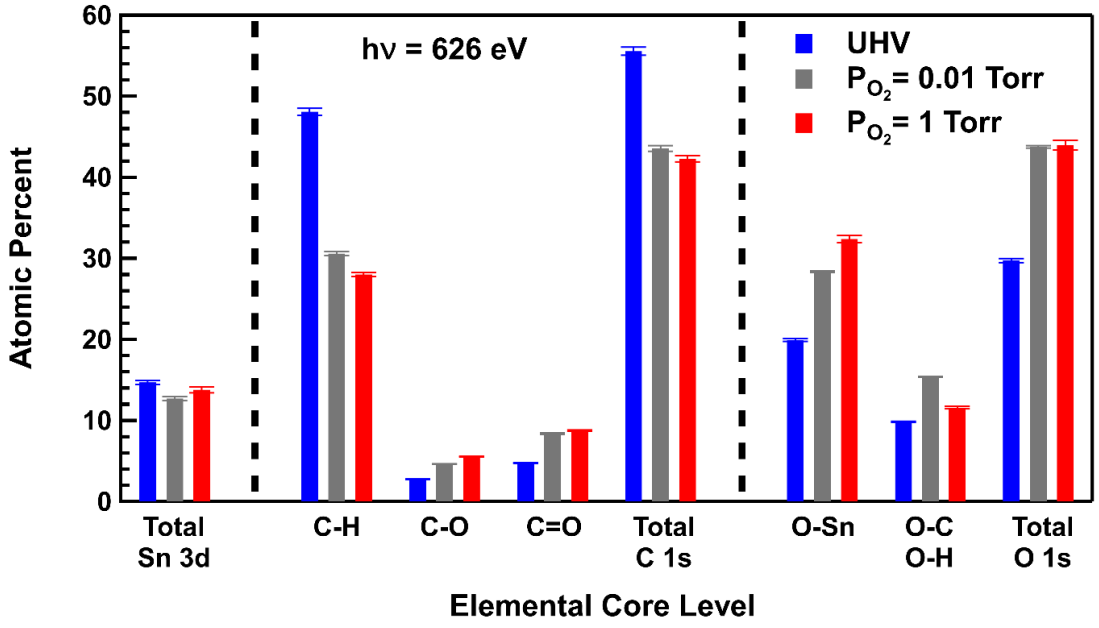

Figure 4.5. Atomic percent calculations showing the compositional changes for C 1s, O 1s, and Sn 3d core levels and their respective chemical states after sequential C 1s scans (42 min of exposure) at $h\nu$ = 626 eV.

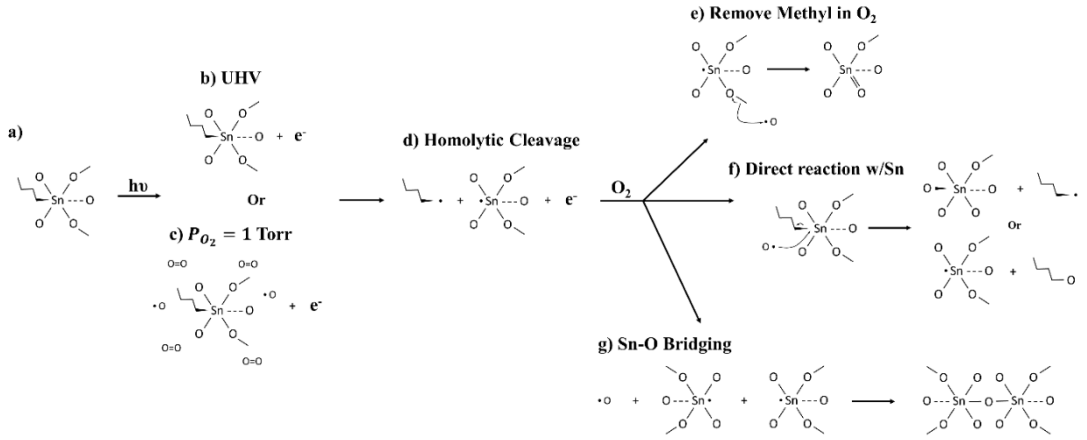

Figure 4.6. Proposed mechanism showing the conversion from β-$NaSn_{13}$ to SnO_2. Photons are absorbed leading to photoemission (a), followed by electron scattering and generation of secondary electrons (b and c). The homolytic cleavage of butyl ligands (d) is enhanced in the presence of oxygen and provides a more efficient route to SnO_2 (e, f, and g).

Table 4.1. Ratio of TEY from β-NaSn13 resists normalized to $h\nu$ = 472 eV. Ratio of X-ray attenuation for different photon energies and oxygen partial pressures normalized to UHV. Photoabsorption cross section values obtained from Henke et al.[66]

hν (eV)	**UHV Normalized TEY Intensities**	**Attenuation of X-rays Normalized to UHV**	
		0.01 Torr	**1 Torr**
472	1.0000	1.0000	0.9973
510	1.5934	1.0000	0.9978
530	2.1454	1.0000	0.9980
626	3.4893	0.9997	0.9745

CHAPTER 5:

EFFECT OF AMBIENT CONDITIONS ON ORGANOTIN EUV PHOTORESIST RADIATION CHEMISTRIES

J. Trey Diulus[1], Ryan T. Frederick[1], Danielle C. Hutchison[2], Igor Lyubinetsky[1], Rafik Addou[1], May Nyman[2], Gregory S. Herman[1,2,3*]

[1]School of Chemical, Biological and Environmental Engineering, Oregon State University, Corvallis, OR, 97331, USA

[2]Department of Chemistry, Oregon State University, Corvallis, OR, 97331, USA

[3]Department of Physics, Oregon State University, Corvallis, OR, 97331, USA

*Corresponding Author

Manuscript in preparation

5.1 ABSTRACT

Solution-based organometallic nanoclusters are unique nanoscale precursors due to the ability to precisely control their size, shape, structure, and assembly. The interaction of extreme ultraviolet (EUV) or X-ray photons with these organometallic nanoclusters can result in processes where organic ligands are modified and can lead to a change in solubility. This makes organometallic nanoclusters prime candidates for next-generation photoresists for EUV nanolithography. In this study, we investigate the interaction of X-ray radiation with a charge neutral, sodium templated, butyl-tin Keggin (β-$NaSn_{13}$) nanocluster. This cluster is used as a model EUV photoresist to better understand the radiation induced solubility transition. Near ambient pressure X-ray photoelectron spectroscopy (NAPXPS) was used to characterize the β-$NaSn_{13}$ thin films, where Sn 3d, O 1s, and C 1s core-levels where measured under a range of ambient conditions, including ultrahigh vacuum and 1 mbar of oxygen, water, methanol, or nitrogen. A photon dose array was obtained for each ambient condition to determine their effect on the photon induced chemistries which result in the observed solubility transition. The resulting contrast curve indicate that an oxygen ambient significantly reduces the required photon dose relative to UHV, while all other ambients increases the required photon dose relative to UHV. We performed in-situ XPS after annealing post-exposure β-$NaSn_{13}$ thin films in multiple ambients to study the chemistry that occurs after a post exposure bake (PEB). The β-$NaSn_{13}$ thin films retained a significant amount of aliphatic carbon following the PEB in all the ambients we studied. Based on our studies, we propose that the solubility transition for β-$NaSn_{13}$ thin films occurs through radical hydrogen abstraction and radical–radical coupling

reactions. These studies further improve the understanding of photon induced chemistries in a β-$NaSn_{13}$ model resist and provides mechanistic insights for EUV lithography processing with organometallic nanomaterials.

5.2 INTRODUCTION

As integrated circuits continue to decrease in size, photolithography is often pushed to its resolution limits to meet the required device scaling.[32] In order for integrated circuits to continue on the International Roadmap for Devices and Systems, sub-10 nm ½ pitch are required. [31,96,97] By reducing the wavelength of light the ½ pitch can be achieved without resorting to quadruple patterning or beyond.[32,96] Currently, a transition from deep ultraviolet (DUV, λ=193 nm) nanolithography to shorter wavelength extreme ultraviolet (EUV, λ=13.5 nm) nanolithography is commercially underway.[32] Although EUV nanolithography is being adopted this transition still has several issues that need to be addressed, including increased EUV source power, higher tool uptime, lower mask defects, improved pellicle design, reduced stochastic effects, and photoresists that manage the resolution, line edge roughness (LER), and sensitivity tradeoff.[32,35,96]

Recent advances to improve high-resolution EUV photolithography have focused on the development of new photoresist materials. One promising class of EUV photoresist materials include organometallic nanocluster photoresists. [31,96,98,99] When these organometallic nanoclusters are exposed to radiation the bond between the organic ligands and the metal group can undergo homolytic cleavage. The reaction of

the resulting radicals can result in a change in solubility.[5,8,50,45] A benefit of these organometallic nanocluster resists is that they can be synthesized with precise control over their size, shape, structure, composition, and ligand chemistries, which allows the development of a wide range of materials that can be optimized for EUV nanolithography. [28,17] The highest performing materials include elements that have high photon absorption cross sections for EUV radiation (λ=13.5 nm and hν=92 eV).[96,100] These organometallic cluster photoresists can potentially replace the industry-standard polymer photoresists for EUV photolithography with the goal to provide higher resolution, lower LER, higher sensitivity, and higher etch resistance.[31,5,50,96]

Organotin nanoclusters are promising for numerous applications, including inorganic photoresists for EUV photolithography.[67,101] Synthetic approaches for organotin nanoclusters allow precise atomic-scale control, where a range of chemical compositions and properties can be obtained through manipulation of size, shape, or structure.[16] We have previously studied a charge-neutral sodium templated butyltin Keggin cluster [$NaO_4(BuSn)_{12}(OH)_3(O)_9(OCH_3)_{12}(Sn(H_2O)_2)$] ($\beta$-$NaSn_{13}$) as a model organotin photoresist to better understand radiation induced reaction mechanisms.[86,102] A benefit of the β-$NaSn_{13}$ system is that tin has a high photon absorption cross section for EUV radiation (~20x greater than carbon).[67] Furthermore, β-$NaSn_{13}$ is charge-neutral and does not need counterions,[5] which allowed us to focus primarily on the butyltin chemistries.

When photoresists are exposed to EUV radiation both photo- and Auger electrons are emitted, and these primary electrons can inelastically scatter to form secondary electrons with lower kinetic energy. These secondary electrons have been

shown to be the primary radiation species responsible in driving photoresist chemistries during EUV exposures.[8,50,45] Electron stimulated desorption (ESD) studies from butyltin hydroxide oxide hydrate thin films have indicated that butyl ligands desorb upon exposure to low kinetic energy electrons. This process occurs with high cross sections, and was correlated with the homolytic cleavage of the butyl-tin bond.[45] Recent studies have used contrast curves to study the photosensitivity of tin-oxo cluster resists.[34,103] These contrast studies can also be used to hypothesize on the mechanisms that take place in the photoresist. For example, recent studies have indicated that the bond strength of the hydrocarbon ligand attached to the tin atom was inversely proportional to the photoresist sensitivity, which suggests that cleavage of the Sn-C bond is the rate limiting reaction.[34] It has also been determined that the post exposure bake (PEB) conditions can also affect photoresist performance, which indicates that further reactions of photo-generated products take place by the addition of thermal energy.[103]

To reduce the risk of photoresist outgassing on contaminating the reflective optics in EUV steppers ASML has introduced a dynamic gas lock (DGL) membrane. The DGL membrane separates the projection optics from the ambient in the wafer handling system. The DGL membrane also allows EUV radiation to pass through with negligible aberration effects.[104] In addition to protection from ambient exposure, the DGL membrane setup additionally allows for alternative molecules to be intentionally introduced into the photoresist side of the membrane, providing an additional variable in optimizing photolithographic performance. Thus obtaining an understanding of

ambient interactions with resist materials can provide an important role in industrial applications.

Varying the ambient conditions during photon exposure has been shown to affect photosensitivity. DUV exposures of organotin cage photoresists showed an increase in the amount of carbon loss for exposures in air versus N_2, with a corresponding increase in oxygen incorporation for exposures performed in air.[7] Multiple studies have recently shown that oxygen can increase photoresist sensitivity.[86,102] For example, an increase in ESD cross sections for hydrocarbons during low kinetic energy electron exposure in O_2 has been demonstrated for β-$NaSn_{13}$ thin films, which suggests that reactive oxygen species affect the radiation chemistries.[86] A significant increase in carbon loss from β-$NaSn_{13}$ thin films was demonstrated after exposure to soft X-rays in ~1.3 mbar of O_2 versus ultra-high vacuum (UHV).[102] Adjusting the photon energy, and thus controlling the total electron yield, indicated that a direct relationship could be made with the reaction rate and amount of carbon loss. These results imply that reactive oxygen species can be formed through interaction of O_2 with secondary electrons and the reactive oxygen species can result in an increase in photoresist sensitivity.[102]

Prior studies following post exposure bakes indicated that a significant amount of carbon remained in the organotin photoresists.[105] Following an exposure in 1 mbar of O_2, which was high enough to change the photoresists solubility, there was a decrease in the total C 1s atomic percent (at %) to 49 % from the original films 57 %.[105] There was little to no change in the total C 1s at % after annealing to 170 °C in vacuum for locations that were exposed to radiation versus those that were unexposed. Further

analysis with other molecules is needed to better understand the radiation induced reaction mechanisms and processes that occur following exposure and the PEB.

In this study, we evaluated the effect of ambient conditions during exposure on the sensitivity of β-$NaSn_{13}$ photoresists. Contrast curves were generated to estimate the change in photoresist sensitivity with respect to ambients with different gases. We used near ambient-pressure X-ray photoelectron spectroscopy (NAPXPS) to characterize the chemical and compositional changes *in-situ* for each ambient used. We additionally studied the chemical changes following *in-situ* PEBs of β-$NaSn_{13}$ photoresists in multiple ambients to determine the effect thermal energy has on the contrast mechanism. Finally, we provide a possible mechanistic description of the lithographic process for β-$NaSn_{13}$ photoresists.

5.3 EXPERIMENTAL

The β-$NaSn_{13}$ clusters were synthesized by a procedure described previously.[67] To form the precursor solution, 20 mg/mL of β-$NaSn_{13}$ clusters were dissolved in 2-heptanone (99%, VWR) and mixed via ultra-sonication for five minutes to make a 90 mM (Sn-basis) solution. Si substrates with a 100 nm thermally grown oxide (TOX) were pretreated by sonicating separately in acetone, 2-propanol, and deionized water for 2 min, followed by a 50 watt O_2 plasma etch for five minutes. Hexamethyldisilazane (HMDS) (99.2%, MP Biomedicals) was spin coated onto the Si substrates to create a hydrophobic surface and improve cluster adhesion and film uniformity. The HMDS was puddled on the substrate for approximately 30 seconds and then spin dried at 3000 RPM for 30 seconds. The β-$NaSn_{13}$ cluster solution was filtered through 0.45 μm PTFE

syringe filter and then puddled onto the Si substrate. A thin film of β-$NaSn_{13}$ was obtained by spin-coating at 3000 RPM for 30 seconds. Samples were then annealed at 70 °C for 3 min in air to remove residual solvent. Atomic force microcopy has indicated that this procedure provides uniform films with low roughness and spectroscopic ellipsometry has indicated that the films are ~20 nm thick.[45] Each substrate was cleaved into ~5x10 mm^2 coupons for sample mounting. Several samples were coated and those that were not immediately used were stored under vacuum in a sealed desiccator.

Experiments were performed with a SPECS NAPXPS system with a base pressure $<2\times10^{-10}$ mbar. Monochromatized Al Kα radiation (hν = 1486.6 eV, 50W, 15kV) was used as the radiation source for obtaining contrast curves in UHV and $P_{O_2} = P_{D_2O} = P_{MeOH} = P_{N_2} = 1$ mbar, as well as for measuring high resolution C 1s, O 1s, and Sn 3d core level spectra in each ambient. Spectra were obtained with an electron analyzer pass energy of 38 eV, and normal emission. The X-ray beam diameter on the substrate was ~300 μm. XPS data were charge corrected to the C 1s aliphatic carbon binding energy (E_b) at 284.8 eV. The spectra were fit using Gaussian-Lorentzian line shapes and a linear background. Since β-$NaSn_{13}$ is dynamically changing during exposure to X-rays the full width half maximum (FWHM) values were allowed to vary up to ±0.05 eV. Changes in charge compensation from differing ambients is also considered with this variation in fitting constraints.

The gas manifold for the ambient pressure cell has connections to both an Edwards nXDS6i scroll pump and a Hi Cube 80 Pfeiffer Turbo. A base pressure of $< 1 \times 10^{-5}$ mbar was achieved for the manifold. The manifold was also connected to an O_2

lecture bottle (99.997% Matheson Purity, Matheson), a N_2 300 CF cylinder (99.999% Ultra High Purity, Airgas), and Schlenke vials (Wilamed Lab Glass) that contain either anhydrous methyl alcohol (Absolute AR ACS Grade, Macron Fine Chemicals) or deuterated water (99.9% Sigma-Aldrich). A high-precision variable leak valve was used to control the pressure in the ambient pressure cell. A residual gas analyzer (RGA200, Stanford Research Systems), located in the differentially pumped portion of the analyzer, was used to collect background mass spectra and verify the purity of each molecule.

For contrast studies, the ambient pressure cell was stabilized at a fixed ambient condition ($P_x = 1$ mbar) or kept at UHV before exposing the β-$NaSn_{13}$ photoresist to X-rays. An automated manipulator drive was used to move the sample so that the X-ray exposure times can be precisely controlled. The exposure time began once the X-rays spot was moved to a new location on the β-$NaSn_{13}$ thin film. Each location was exposed for increasing lengths of time (Δ = 100 sec). For longer dose times, XPS data were collected during the exposure. The O 1s, C 1s, and Sn 3d spectra were separately obtained immediately after moving to a new sample location, denoted as "Initial," so that chemical changes during exposure in one location would not affect the initial spectra for each core-level. Slight intensity changes can occur from moving to different a location on the sample due to small changes in the distance of the sample to the analyzer. Therefore a reference Sn 3d spectrum was collected in the same location following each initial spectrum to assist in normalizing the spectra. A C 1s, Sn 3d, O 1s, Sn 3d sequence was obtained in the same location after an 1800 sec exposure and these spectra are labeled "After 30 min." All "After 30 min" spectra were additionally

normalized by a reference Sn 3d peak collected after the main sequence. All spectra were normalized by dividing the spectra by the total peak area of the Sn $3d_{5/2}$ reference spectra.

For annealing studies three locations were chosen to obtain C 1s, O 1s, and Sn 3d spectra, each followed by a Sn 3d reference spectra. All three locations were exposed to X-rays to achieve 1800 s exposures. The ambient pressure cell was stabilized for a given pressure and gas ($P_x = 1$ mbar) or kept at UHV. Samples were annealed for 5 min at 170 °C (±5°) in each ambient and then cooled back to room temperature. The ambient gas was slowly pumped from the ambient pressure cell once the sample was < 130 °C. The X-ray spot was then moved back to the saved manipulator positions for the previous three 1800 s exposures. A C 1s, Sn 3d, O 1s, Sn 3d sequence was obtained at each of these locations and are labeled "After 30 min, 170 °C Anneal." Three additional locations which were not exposed to X-rays were analyzed after the anneal to monitor the changes in the spectra related to just the annealing process.

Photoresist films were developed immediately after removing the samples from the XPS system after X-ray exposure. Photoresist films were baked for 5 min at 170 °C on a temperature controlled hot plate. For the samples annealed in the SPECS system, no external bake was used. The photoresist films were then immersed in a 2-heptanone bath for 60 seconds and then blow dried with compressed N_2. A J. A. Woollam M-2000 spectroscopic ellipsometer was used to measure the thickness of the insoluble film that remains after development. Developed spot sizes varied depending on the different ambient used and length of time exposed. Therefore, the thickness of the center region for the developed spot is what was used for the contrast curves. The thickness

measurements were normalized by subtracting the smallest measured thickness and then dividing by the difference between smallest and largest measured thickness. An average of three normalized thickness measurements were used to determine the thickness for each exposure time. Error bars were determined by calculating a 95% confidence interval.

An estimate the photon dose was made by using the manufacturer specified photon flux for a Specs μ-FOCUS 600 X-ray monochromator, which is $9x10^{10}$ photons/s. With a spot size of ~370 μm and assuming 90% transmission through the SiN window on the ambient pressure cell. This resulted in a photon flux of $2.5x10^{13}$ photons/cm^2/s. For an exposure time of 1800 seconds, the corresponding photon dose is ~$4.5x10^{16}$ photons/cm^2.

Each contrast curve was further analyzed by fitting three lines to the curve. A low exposure line was fit from time 0 to the time (dose) before a significant increase in thickness (>0.05 increase) occurs. A high exposure line was fit from the time (dose) at which a maximum normalized thickness of 1 is reached, to the final measured time. The third line is the linear slope in the region between the endpoint of the low exposure line and the beginning of the high exposure line. The intersection of the linear slope and low exposure line is the energy density D_0, while the intersection of the linear slope and high exposure line is the energy density D_{100}. A contrast parameter (γ) can be calculated using Eq. 5.1 from Campbell et al.[106]

$$\gamma = \frac{1}{\log_{10}(D_{100}/D_0)} \qquad \text{(Eq. 5.1)}$$

To estimate the at % relative sensitivity factors we determined attenuation lengths and differential cross sections for each XPS transition. To calculate the attenuation length we used Equation 15 from Cumpson et al.[107] The differential cross section was calculated using equation 89 from Fadley et al.[108] where we used published photon absorption cross sections values from Yeh et al.[33] and a 60° X-ray source-to-analyzer-angle. Rewriting equation 115 from Fadley et al. and assuming negligible differences from the solid angle, specimen area, and detection efficiency between spectra gives Eq. 5.2:

$$\frac{\rho_2}{\rho_1} = \frac{I_2 \Lambda_1 (d\sigma_1/d\Omega)}{I_1 \Lambda_2 (d\sigma_2/d\Omega)} \qquad \text{(Eq. 5.2)}$$

Where we can calculate the atomic densities (ρ) using the peak intensities (*I*), attenuation lengths (Λ), and differential cross sections $\left(\frac{d\sigma}{d\Omega}\right)$.[108] Similar at % were obtained for samples measured in a Perkin Elmer PHI 5600 XPS system that has published sensitivity factors for a 90° angle between the X-ray source-to-analyzer-angle.[86]

5.4 RESULTS AND DISCUSSION

To better understand the solubility transition mechanism for β-$NaSn_{13}$ we have plotted contrast curves to evaluate how the resist sensitivity changes for different ambient conditions. The contrast curve for β-$NaSn_{13}$ photoresists from exposure to Al Kα X-rays in multiple ambients is shown in Figure 1. In this figure the normalized film thickness after development is plotted with respect to exposure time. While Al Kα X-rays have a higher photon energy than EUV radiation, secondary electrons will still be

the dominant energetic species generated during exposure and have been shown to drive the solubility switch.[45,86,105] Therefore, Al Kα X-rays can be used to study the solubility change during exposure and investigate the detailed chemical reaction mechanisms.

β-$NaSn_{13}$ is a negative photoresist and the contrast curve provides an estimate of the minimum dose required to fully convert the photoresist to an insoluble film. The maximum thickness data point is the time where the photoresist is no longer soluble in organic solvents. By using the calculated photon density and exposure time, a photon dose can also be obtained. It is important to consider that the dose measurement is specific to the radiation source used. Lower doses are expected for EUV radiation due to higher photon absorption cross sections (generating more secondary electrons) for Sn, O, and C at 92 eV compared to 1486.6 eV for Al Kα, and the higher photon flux for EUV steppers. The calculated doses allow us to have a numerical comparison between different ambients and are specific to our experimental system.

In Figure 1, a shift to lower exposure time (lower dose) was observed for exposures in P_{O_2}= 1 mbar compared to UHV. These results were expected based on prior studies that have shown a lower dose requirement, and thus higher sensitivity, for exposure in O_2 ambients.[105] Two other molecules containing oxygen were studied to assess how the photoresist sensitivity may change during exposure. Both deuterated water (D_2O) and methanol (MeOH) were used as potentially reactive species after interacting with secondary electrons. Furthermore, it is expected that D_2O would primarily interact with the hydrophobic surface of the β-$NaSn_{13}$ thin film, while MeOH would diffuse through the thickness of the thin film since it is the solvent used to purify

β-$NaSn_{13}$ during synthesis.[67] Oxygen gas molecules can also diffuse through the thickness of the thin film.

The interaction of D_2O or MeOH with low energy photoelectrons (40-100 eV) could lead to the production of reactive hydroxyl species that could oxidize components in the resist and potentially increase resist sensitivity. However, we found that both D_2O and MeOH required an increase in the necessary dose for the solubility transition, and as a result decreased the resist sensitivity. Literature reported electron induced ionization cross sections for both water and molecular oxygen species provide the probability of generating excited species. Both water and molecular oxygen have similar total ionization cross sections of ~$2x10^{16}$ cm^2 for electron energies of 40-100 eV.[109,110] The primary excited species for water are H_2O^+, OH^+, and H^+, where H_2O^+ has the largest ionization cross section of ~$1x10^{-16}$ cm^2 from 40-100 eV.[109] OH^+ and H^+ have nearly identical cross section values at ~$3x10^{-17}$ cm^2 for the same energy range.[109] Comparing to oxygen, O_2^+, O^+, and O^{++} are the main species produced from electron induced ionization.[110] O_2^+ has an ionization cross section of ~$1.5x10^{-16}$ cm^2 while O^+ has a cross section of ~$0.7x10^{17}$ cm^2.[110] While the total cross sections are similar for both molecules and both have oxidizing species generated, the generation of H^+ from exposure to water can interact with the film and create hydrolyzed species. The β-$NaSn_{13}$ cluster has been shown to be sensitive to hydrolysis in solution through exchange of the bridging hydroxyl ligands.[111] This reaction is additionally expected for exposure in MeOH, where the primary species CH_3OH^+, CH_2OH^+, CHO^+ all have ionization cross sections of ~$1x10^{-16}$ cm^2 from 40-100 eV, as well as H_2^+ with an ionization cross section of ~$3x10^{-17}$ cm^2, which can all act as hydrogen donors.[112]

Nitrogen was chosen as an inert molecule to determine whether the presence of gaseous molecules has a distinct and separate effect on the photoresist sensitivity. Assuming that no oxidizing or reducing species interact with the film when exposed to N_2, then the contrast curves in N_2 and in UHV should be similar. However, we found that an increase in exposure time was necessary for exposures in N_2 relative to UHV. This suggests that N_2 may absorb photons or scavenge secondary electrons thereby causing a decrease in sensitivity. Photon transmittance through each molecule can be calculated using mass attenuation coefficients for $h\nu$ = 1500 eV which are provided by NIST.[113] Assuming room temperature, 1 mbar pressure, and a 1 cm X-ray path length we can estimate that the percent of photon transmission to the sample surface is ~99.8% with a standard deviation of ±0.05%. Therefore, the reduction in photon flux for Al Kα X-rays due to photon absorption is minimal and should be similar for all four gas molecules. The interaction of secondary electrons with the gas phase species is therefore the most likely reason for the decrease in sensitivity. The integral electron elastic scattering cross sections in each ambient has been reported. For energies ranging from 1-30 eV, O_2 has the lowest electron elastic scattering cross sections[114] followed by N_2,[115] D_2O,[116] and MeOH.[117] At 2 eV, there is a significant difference in electron elastic scattering cross sections where N_2 is ~3x larger and D_2O and MeOH are ~5x larger than O_2.[114,115,116,117] Looking at the total scattering cross sections, which includes multiple inelastic electron scattering events, the same trend is observed which matches the contrast curve results.[109,110,118]

In addition to obtaining a visual representation of the changes in dose requirements, a contrast parameter (γ) was calculated using equation 1. This numerical

value is representative of how sharp the soluble to insoluble transition is for β-$NaSn_{13}$. Table 1 shows the calculated D_0, D_{100}, and γ parameters for each of the ambients used for these studies. Typical γ values for commercial photoresists range from 2 to 4, which means D_{100} is ~2-3 times greater than D_0.[106] Large values for γ correspond to a material with a high contrast, however high numbers can also signify low sensitivity if D_0 and D_{100} values are high.[106] For β-$NaSn_{13}$, we found that UHV had the lowest contrast where γ = 3.3, however UHV also had the second highest sensitivity with D_{100} = 1100 s ($5.4x10^{15}$ ph/cm^2). For P_{MeOH} = 1 mbar, the contrast is the highest at γ = 4.4, and also had the lowest sensitivity where D_{100} = 1700 s ($8.1x10^{15}$ ph/cm^2). For extended exposures in all ambients, there is a decrease in the maximum thickness after reaching D_{100}. Exposure in O_2 had the largest decrease in thickness, which we attribute to further desorption of the butyl groups from the photoresist during interaction with the X-rays.

C 1s XPS spectra were obtained for all five ambient conditions both before X-ray exposure (initial) and after 30 min of X-ray exposure. The spectra are shown in Figure 2. Three peaks can be fit to each of the spectra, where aliphatic carbon (C-H) has E_b = 284.8 eV (blue), carbon atoms singly bound to oxygen (C-O) has E_b = 286.4 eV (green), and carbon atoms doubly bound to oxygen (C=O) has E_b = 288.6 eV (red).[53] The most intense C-H peak is correlated to butyl ligands, while the C-O peak is correlated to the methoxy ligands,[53] both of which are components bound to the β-$NaSn_{13}$ nanocluster. C=O is not expected in the film, therefore we believe this component is due to contamination from exposure to atmosphere. Adventitious carbon may also be present on the surface of the thin film and would lead to an overestimation

of the C-H:C-O intensity ratio. A fourth peak is also seen in Figured 2d, which corresponds to gas phase C-H (labeled as MeOH (g) in the figure) with E_b = 287.8 eV.

The attenuation of electrons due to the gas phase is evident in the C 1s spectra, where the initial C-H peak intensity is highest for spectra obtained in UHV. Otherwise, all the initial C 1s spectra intensities shown in Figure 2 are very similar for each of the conditions except for P_{MeOH} = 1 mbar. For P_{MeOH} = 1 mbar (Figure 2d) there is a larger oxygenate peak intensity. This is partly due to the presence of a gas phase C-O peak, however the fit for C-O at E_b = 286.4 eV is still largest under these experimental conditions. This increase in C-O potentially suggests the presence of adsorbed MeOH in the film. An increase in C-O on the surface could also result in an exchange reaction between methoxy with hydroxyls in the photoresist thin film. A similar reaction occurs during the purification synthesis of the β-$NaSn_{13}$ nanoclusters. For all other ambients there was no evidence that the film chemistry was different for the initial spectra. After a 30 min X-ray exposure, a significant decrease in the C-H peak intensity was observed for P_{O_2}= 1 mbar (Figure 2b), which has previously been shown.[86,102,105].

XPS spectra for Sn 3d and O 1s were also obtained for each experimental condition. The Sn $3d_{5/2}$ peak is located at E_b = 486.6 eV, along with the Sn $3d_{3/2}$ peak located at E_b = 495 eV.[53] No change in chemical state information was observed for the Sn 3d peaks, where there was only an increase in the relative intensity as carbon desorbs from the film. Figure 3 shows the O 1s XPS spectra for all ambient conditions both before a X-ray exposure (initial) and after a 30 min X-ray exposure. The most intense peak from E_b =528 to 534 eV corresponds to the oxygen that is incorporated in the β-$NaSn_{13}$ clusters, while the higher binding energy peaks correspond to gas phase oxygen

which is independent of the film. Two peaks were used to fit the O 1s spectra that correspond to the film, where tin oxide (E_b = 530.5 eV, O−Sn) and methoxy/hydroxyls (E_b = 531.9 eV, O−C/O−H) are the two primary components.[53] Due to the similar binding energies for the O-C and O-H peaks, only one peak was used to represent contributions from both species.[53,74] We have previously observed that the methoxy groups can exchange with hydroxyls when the films are exposed to moisture. As such, we expect that there may be some O-H contamination in the films, as well as other oxygenates (based on the C 1s spectra). This contamination may lead to overestimation of the O-Sn:O-C/H ratios. For the gas phase spectra, two peaks are used to fit the O 1s (g) at E_b = 538.2 eV and 539.83 eV, one peak at E_b = 535.1 eV for D_2O (g), and one peak at E_b = 534.3 eV for MeOH (g). While it appears that the gas phase spectral intensity is changing in the data, this is due to the normalization procedure used for the spectra, where the gas phase peak intensity is independent from the film.

The initial O 1s spectra are all very similar with approximately a 2:1 O-Sn:O-C/H ratio. After the 30 min exposure in UHV there was an increase in the O-Sn peak intensity and a slight decrease in the O-C/O-H peak intensity which led to a 2.5:1 O-Sn:O-C/H ratio. After the 30 min exposure in P_{O_2} = 1 mbar there was a further increase in the O-Sn peak intensity and decrease in O-C/O-H peak intensity resulting in a 3:1 O-Sn:O-C/H ratio. These results suggest that the incorporation of oxygen with Sn is enhanced in presence of O_2, while also reducing the O-C/O-H component. This also suggests that exposures in O_2 results in the direct oxidation of Sn sites, which was also observed in prior studies.[86,102] After the 30 min exposures in P_{D_2O} = 1 mbar and

P_{MeOH} = 1 mbar there was virtually no change in the O-Sn, peak intensity while the O-C/O-H peak intensity increased. Since the O-Sn peak intensity does not decrease, it is unlikely that hydrogenation of the Sn sites after homolytic cleavage of the butyl-tin bond occurs. However, hydrogenation of the butyl radical could be occurring through hydrogen radical abstraction from butyl groups still bound to the β-$NaSn_{13}$ clusters. After the 30 min exposure in P_{N_2}= 1 mbar, we observe results similar to UHV and O_2 where there is an increase in O-Sn peak intensity. However, in N_2 there is an increase in O-C/O-H as well, which is the opposite compared to both UHV and O_2. Since no nitrogen was detected in the film using XPS we believe that N_2 is not directly interacting with the buytl ligands. From these results we find that the ambient during exposure can affect the desorption of butyl ligands, and modify the O-Sn and O-C/H chemistries.

To gain more insight into the photoresist chemistries we have determined the relative at % values from the XPS data. Table 2 shows at % values for each ambient condition before (Initial) and after (After 30 min) the solubility transition takes place. Based on the structure of the β-$NaSn_{13}$ cluster the expected at % are 13% Sn, 58% C (47% C-H, 11% C-O, and 0.0% C=O), and 29% O (24% O-Sn and 5% O-C). The at % values obtained for the elements using the initial spectra are a good match to these expected values, which suggests that our analysis was appropriate. In all cases we find that there is a reduction in the C at % after the 30 minute exposure, where the largest reduction was for the experiment with P_{O_2}= 1 mbar. The corresponding O and Sn at % also increased after the 30 minute exposure. This change is likely due to the desorption

of butyl groups during exposure, which was noted previously for organotin photoresists.[77] To obtain more information regarding the β-$NaSn_{13}$ cluster chemistries we have evaluated the changes in at % for the chemical states in the C 1s and O 1s core level spectra. We find that the C-O component for the C 1s spectra for the Initial measurements was highest for MeOH and lowest for D_2O. This could be due to ligand exchange from hydroxyl to methoxy in MeOH, and from methoxy to hydroxyl in D_2O. The C-O component for the C 1s spectra for the Initial measurements was also high for O_2 which could be due to reaction of oxygen radical species with the butyl groups. Finally, the C-O component was fairly constant for the Initial measurements obtained in UHV, D_2O, and N_2. We find that the C-O component for the C 1s spectra for the After 30 min measurements was highest for MeOH and lowest for UHV and D_2O. This could be due to a similar mechanism which we discussed above. The O-C/O-H component for the O 1s spectra for the Initial measurements did not change significantly for the various ambients. However, we found that O-C/O-H component for the O 1s spectra for the After 30 min measurements increased for D_2O, MeOH, and N_2 likely signaling some hydrolysis taking place.

One model that can be considered for the observed solubility transition for the photoresist could occur through the homolytic cleavage of the butyl-tin bond during exposure to radiation and then accompanying reactions that link clusters through Sn-O-Sn bonds during PEB. For this model it would be expected that a significant amount of butyl groups would need to desorb from the photoresist to link the clusters together. For our studies we found a 20% decrease in total C 1s intensity for exposures in P_{O_2}= 1 mbar. However, these films still contain ~40% carbon following exposure to a dose

that results in the solubility transition. Previous studies have suggested that the excess carbon is removed from organotin photoresists due to the thermal energy provided during the PEB.[119] Since the PEB is typically performed under atmospheric conditions, the O_2 and/or H_2O present in air could assist in desorption of the organic ligands or the formation of Sn-O-Sn network bonds.

We have performed *in-situ* NAPXPS studies to characterize the chemistries that occur after a PEB. We have used the three primary components found in air to provide further insight in the solubility transition of β-$NaSn_{13}$. Prior thermal characterization studies have shown that β-$NaSn_{13}$ thin films are stable up to ~350 °C,[86] and that decomposition of the β-$NaSn_{13}$ is not expected at typical PEB conditions (anneals up to 170 °C). Figure 4 shows both C 1s and O 1s spectra "Before Anneal" (identical to "Initial") and after a 30 min exposure and anneal to 170°C in UHV. Figure 4 also shows C 1s and O 1s spectra for anneals in P_x= 1 mbar of O_2, D_2O, and N_2. MeOH was omitted from annealing studies as there is not expected to be a significant MeOH partial pressure during PEBs. All XPS peak fit parameters and peak identities are the same as used for our contrast studies.

The after exposure and anneal in UHV spectra are nearly identical to Figure 2 and 3 after exposure in UHV and no anneal. Relative at % were calculated for these spectra and the values are provided in Table 3 for PEBs in UHV, P_{O_2}= 1 mbar, P_{D_2O} = 1 mbar, and P_{N_2}= 1 mbar. The results indicate that for all conditions lower total O 1s intensities were obtained compared to the After 30 min spectra. This is likely due to removal of hydroxyl ligands either from adsorbed water or infused water in the

film.[45,86] There was also lower Sn 3d intensities after the PEB compared to the After 30 min spectra. Most notable is that there was a significant increase in the C 1s intensity after the PEB. This increase in C 1s intensity after the PEB may be due to the diffusion of carbon chain radicals from the bulk of the film to the surface. Another difference that we noticed was that the PEB in P_{O_2}= 1 mbar led to an increase in the O 1s component assigned to the O-C/O-H, but there was no decrease in C 1s compared to UHV. The PEB in P_x= 1 mbar of D_2O and N_2 also show an increase in the O 1s component assigned to the O-C/O-H which was greater than what was seen in P_{O_2}= 1 mbar. Additionally, there was an increase in total C 1s intensity for both D_2O and N_2 compared to UHV. This suggests that carbon was not being removed from the photoresist due to chemical reactions with air. We found that there was a noticeable drop in the C 1s component assigned to C-O for PEBs performed in D_2O, which suggests that hydroxyls are exchanging with methoxys in the film.

Combining the results of both the contrast and anneal studies, along with prior literature, we propose a mechanism for the solubility transition of β-$NaSn_{13}$ which is shown schematically in Figure 5. We illustrate this mechanism specifically for exposure in O_2, as this condition results in the highest photoresist sensitivity. First, the photoresist is exposed to radiation (hν) leading to electron emission. These electrons can scatter in the photoresist and result in homolytic cleavage of the butyl-tin bond, as well as the formation of reactive oxygen species. Reactive oxygen species can react directly with undercoordinated tin in adjacent clusters which can lead to Sn-O-Sn networks bridging the clusters. We expect that this is a minor contributor to the

solubility change, and that the interaction of reactive oxygen species with butyl ligands resulting in radical hydrogen abstraction is the primary reaction process. Polymerization of butyl groups can occur through radical–radical coupling reactions during the PEB step. The resulting polymerization results in a film that is no longer soluble in organic solvents.

The formation of a metal polymer formed after the PEB step has recently been suggested for butyl-tin based precursors.[120] The resulting film is dependent on the ligands present in the film during exposure, which provides an opportunity to adjust the density of the oxide by changing the ligands of the precursor.[120] The ambient can also be utilized to tune the performance of the resist during patterning. Specifically for β-$NaSn_{13}$, oxygen can act similarly to a photoacid generator while nitrogen or water can act as a quencher. Adjusting the ligand chemistry would likely affect how the ambient modifies the sensitivity, which would allow for the design of resist materials that can be optimized for a specific pattern or feature size.

We have shown that ambient gasses can play a significant role in resist chemistry, and thus the sensitivity of the resist. Oxygen can be used to reduce the dose requirement for patterning β-$NaSn_{13}$ while water, methanol, and nitrogen increase the dose requirement. This response could potentially be similar for other metal containing photoresists. Following exposure and development of the β-$NaSn_{13}$ resist, there is still significant amounts of carbon remaining in the developed film. While this shows no negative effect in the ability to induce a solubility transition, there could be a negative impact on the desired etch resistance of the film. One of the primary factors in utilizing metal oxide resists is the poor etch resistance found for polymer resists.[121] Ultimately,

further studies on resist performance are necessary to conclude if β-$NaSn_{13}$ can meet the specifications desired for an EUV photoresist.

5.5 CONCLUSIONS

We have shown that the ambient can affect resist sensitivity. An O_2 ambient decreased the dose requirement while D_2O, MeOH, and N_2 all increased the dose requirement compared to UHV. The change in sensitivity is due to the interaction of electrons with the ambient molecules leading to the generation of excited species. In the presence of O_2, reactive oxygen species react with butyl ligands through hydrogen abstraction which then leads to radical-radical coupling reactions. Annealing the sample in vacuum to simulate a PEB, we found essentially no difference in the at % whether we were measuring a portion of the sample exposed to radiation or a portion which was not. The PEB did not remove any carbon from the films. Annealing separately in O_2, D_2O, and N_2 ambients (the three primary molecules in air) also did not remove any carbon from the films. We believe that during the PEB step, that polymerization of the butyl ligands occurs through radical-radical coupling. The resulting film is a metal oxide polymer, which is no longer soluble in organic solvents.

5.6 ACKNOWLEDGEMENTS

This research was funded by the Semiconductor Research Corp. (SRC) Contract Number 2013-OJ-2438 and the Center for Sustainable Materials Chemistry (CSMC) supported by the U.S. National Science Foundation under grant number CHE-1606982. This work was performed, in part, at the Northwest Nanotechnology

Infrastructure, a member of the National Nanotechnology Coordinated Infrastructure, which is supported by the National Science Foundation under grant number NNCI-1542101. Acquisition of the Ambient-Pressure X-ray Photoelectron Spectroscopy/Ambient-Pressure Scanning Tunneling Microscopy system was supported by the National Science Foundation-Major Research Instrumentation program (grant DMR-1429765), the M. J. Murdock Charitable Trust, Oregon BEST, Oregon Nanoscience and Microtechnologies Institute, and Oregon State University.

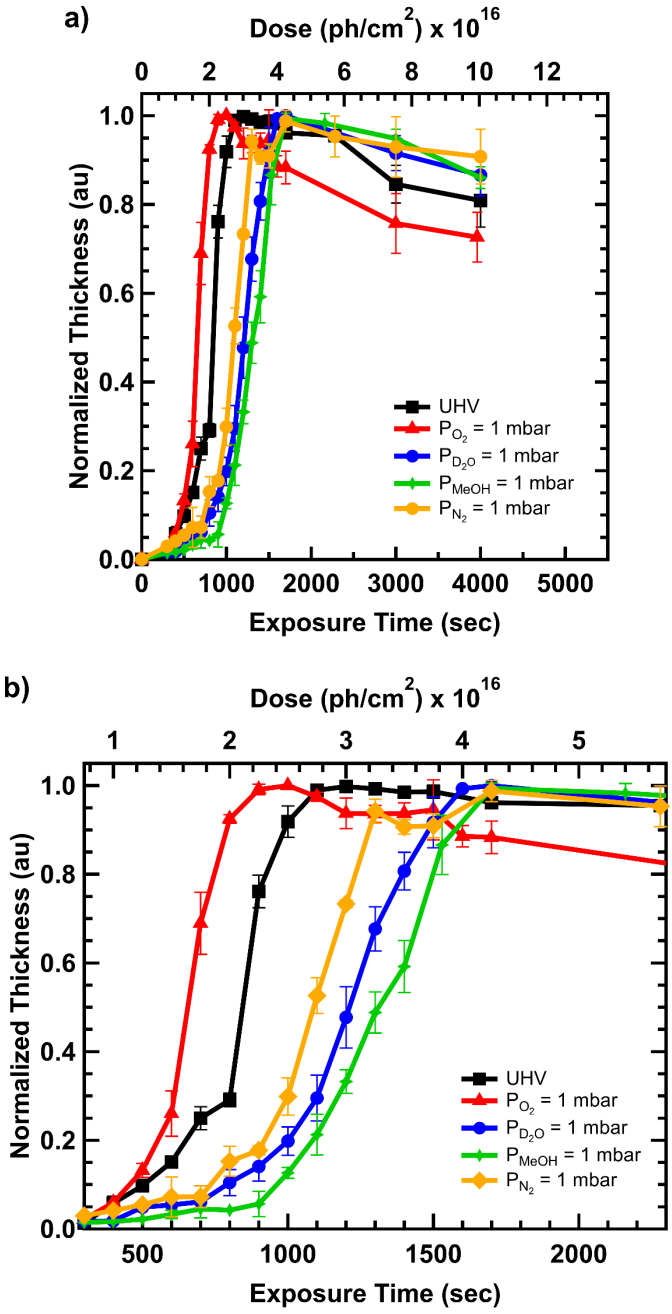

Figure 5.1. Extended (a) and zoomed in (b) β-$NaSn_{13}$ contrast curves using Al K_α X-rays (50 W, 15 kV, 30° impingement) for UHV, P_{O_2}= 1 mbar, P_{D_2O} = 1 mbar, P_{MeOH} = 1 mbar, and P_{N_2}= 1 mbar ambients. Error bars were calculated from an average of three ellipsometer thickness measurements.

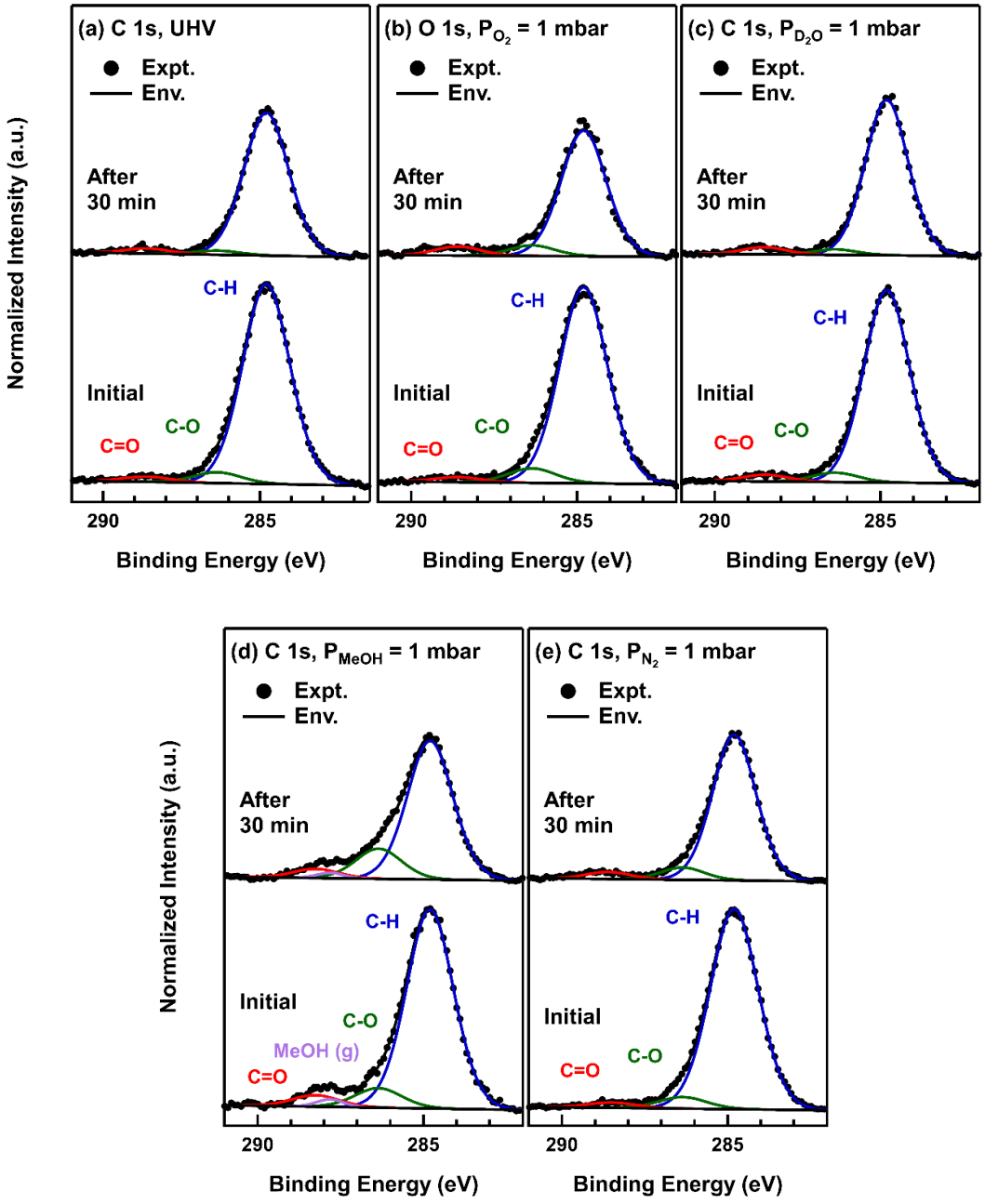

Figure 5.2. XPS for C 1s during exposure to UHV (a), P_{O_2}= 1 mbar (b), P_{D_2O} = 1 mbar (c), P_{MeOH} = 1 mbar (d), and P_{N_2}= 1 mbar (e) for both before X-ray exposure (initial) and after 30 min of X-ray exposure.

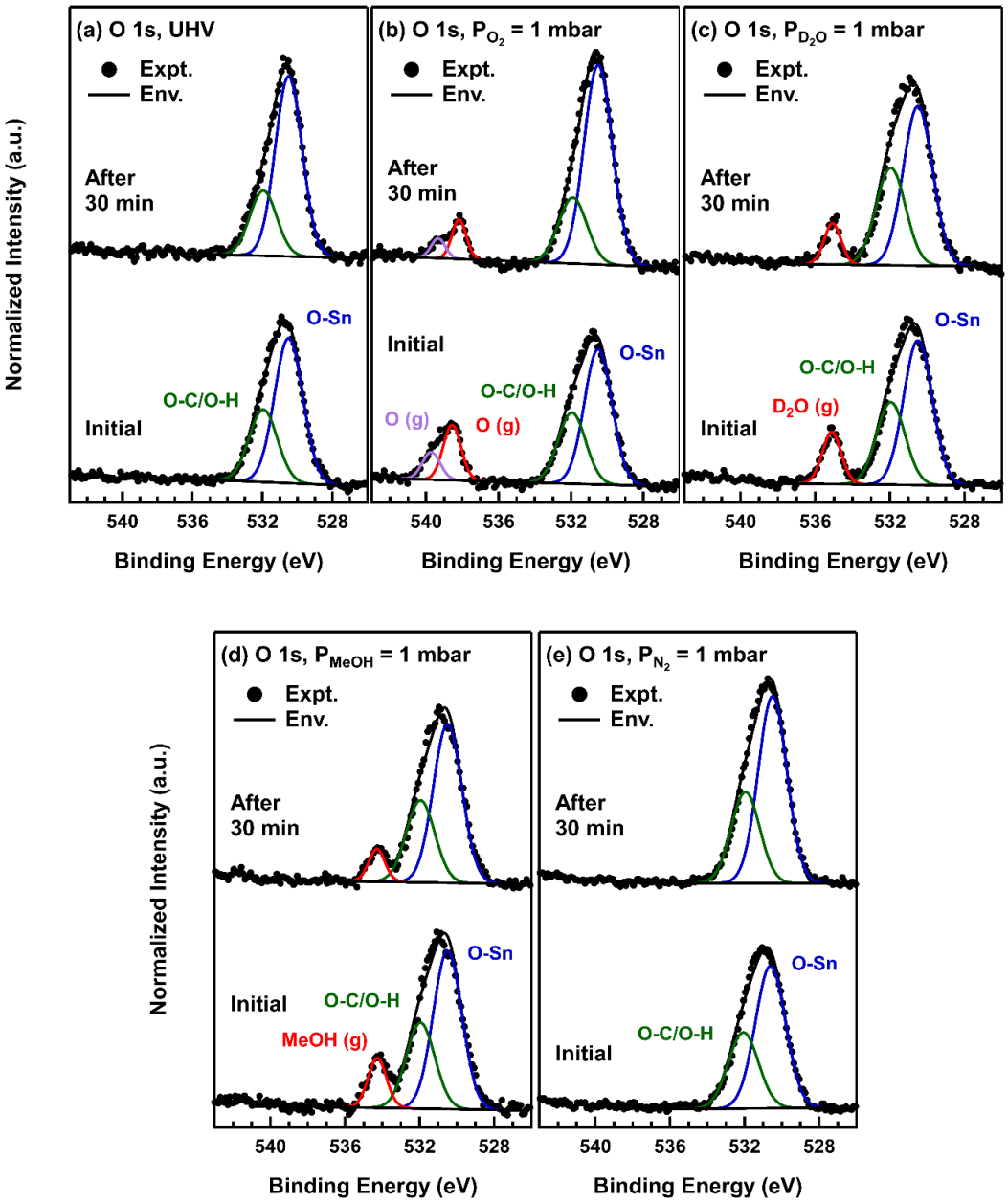

Figure 5.3. XPS for O 1s during exposure to UHV (a), P_{O_2}= 1 mbar (b), P_{D_2O} = 1 mbar (c), P_{MeOH} = 1 mbar (d), and P_{N_2}= 1 mbar (e) for both before X-ray exposure (initial) and after 30 min of exposure.

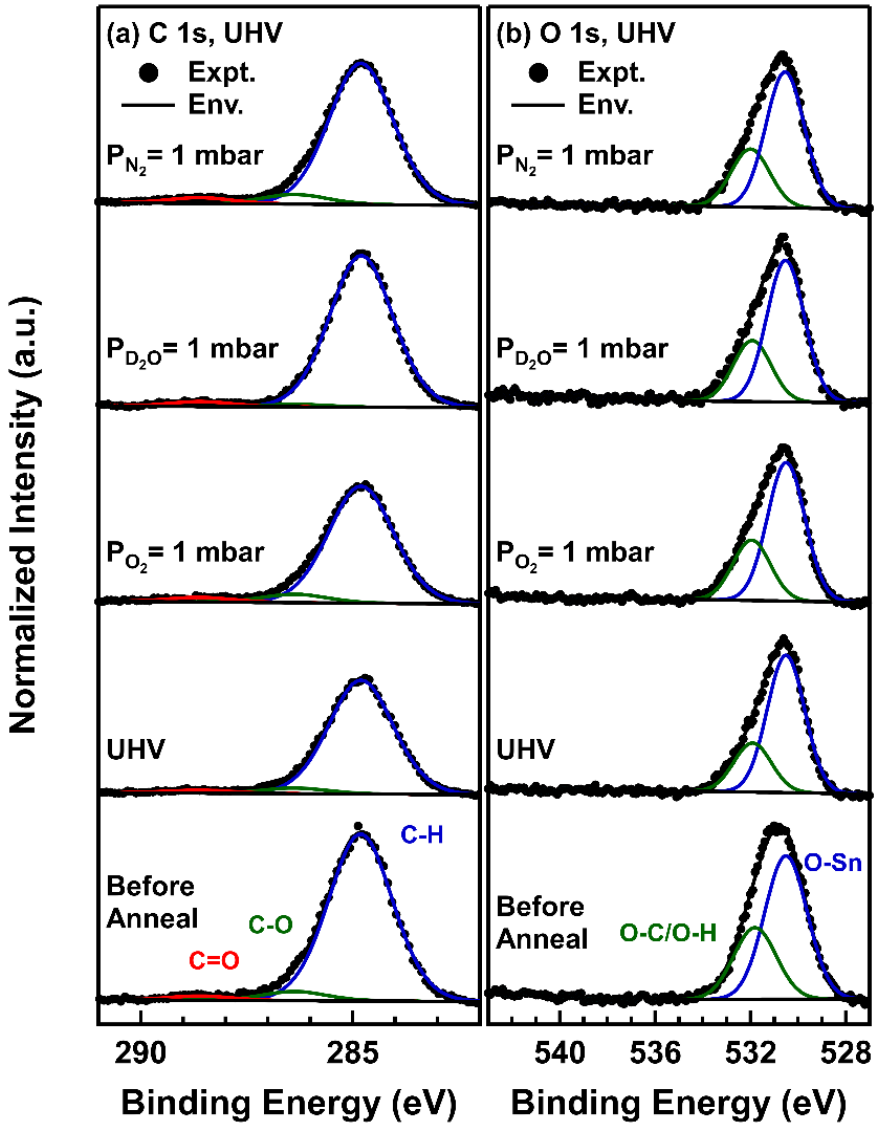

Figure 5.4. XPS for C 1s (a) and O 1s (b) before X-ray exposure and annealing designated "before anneal." Annealing was performed after 30 min X-ray exposure in ambients of UHV, P_{O_2}= 1 mbar, P_{D_2O} = 1 mbar, and P_{N_2}= 1 mbar, then cooled and pumped to UHV before the next set of spectra was collected.

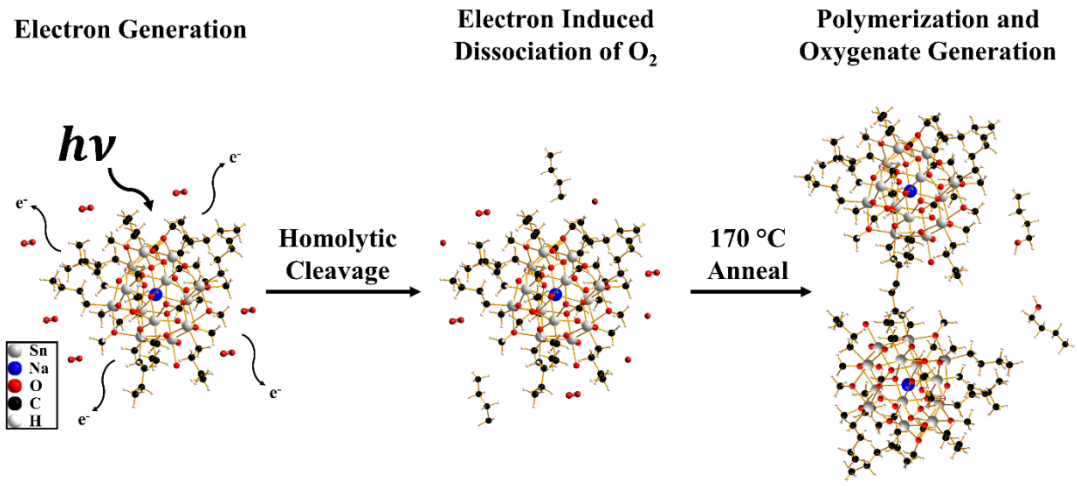

Figure 5.5. Suggested chemical mechanism for the full lithographic process of patterning β-$NaSn_{13}$ in the presence of O_2.

Table 5.1. Calculated D_0 and D_{100} parameters for both photon dose (ph/cm^2 x10^{16}) and exposure time (sec).

	D_0 (ph/cm^2) x10^{16}	D_{100} (ph/cm^2) x10^{16}	D_0 (sec)	D_{100} (sec)	γ
UHV	1.4	2.7	550	1100	3.3
P_{O_2}= 1 mbar	1.2	2.2	470	870	3.8
P_{D_2O} = 1 mbar	2.1	4.0	850	1600	3.7
P_{MeOH} = 1 mbar	2.5	4.1	980	1700	4.4
P_{N_2}= 1 mbar	2.0	3.4	810	1400	4.4

Table 5.2. Calculated XPS At % values for C, O, and Sn obtained from C 1s, O 1s, and Sn 3d spectra before X-ray exposure (Initial) and after 30 min of exposure in UHV, P_{O_2}= 1 mbar, P_{D_2O} = 1 mbar, P_{MeOH} = 1 mbar, and P_{N_2}= 1 mbar.

		UHV	**P_{O_2}= 1 mbar**	**P_{D_2O} = 1 mbar**	**P_{MeOH} = 1 mbar**	**P_{N_2}= 1 mbar**
	Element	**Atomic %**	**Atomic %**	**Atomic %**	**Atomic %**	**Atomic %**
Initial	**Sn**	**13 %**	**12 %**	**12 %**	**11 %**	**12 %**
	C (Total)	**61 %**	**62 %**	**62 %**	**62 %**	**62 %**
	C-H	57 %	56 %	57 %	54 %	57 %
	C-O	3.1 %	4.2 %	2.8 %	5.3 %	3.3 %
	C=O	1.5 %	1.4 %	2.0 %	3.1 %	1.5 %
	O (Total)	**26 %**	**26 %**	**26 %**	**27 %**	**26 %**
	O-Sn	17 %	17 %	17 %	17 %	17 %
	O-C/O-H	8.7 %	9.0 %	9.5 %	9.4 %	9.1 %
After 30 min	**Sn**	**17 %**	**15 %**	**14 %**	**13 %**	**14 %**
	C (Total)	**50 %**	**42 %**	**50 %**	**55 %**	**48 %**
	C-H	47 %	37 %	47 %	43 %	42 %
	C-O	1.3 %	3.1 %	1.7 %	9.3 %	3.6 %
	C=O	1.7 %	2.6 %	2.1 %	2.8 %	2.1 %
	O (Total)	**34 %**	**42 %**	**36 %**	**32 %**	**38 %**
	O-Sn	25 %	32 %	22 %	21 %	26 %
	O-C/O-H	9.0 %	10 %	13 %	11 %	12 %

Table 5.3. Calculated XPS At % information for C 1s, O 1s, and Sn 3d peaks post exposure after annealing to 170 °C for 5 min in UHV, P_{O_2}= 1 mbar, P_{D_2O} = 1 mbar, P_{MeOH} = 1 mbar, and P_{N_2}= 1 mbar.

		No Anneal	**After 170 °C Anneal**			
		UHV	**UHV**	**P_{O_2}= 1 mbar**	**P_{D_2O} = 1 mbar**	**P_{N_2}= 1 mbar**
	Element	**Atomic %**	**Atomic %**	**Atomic %**	**Atomic %**	**Atomic %**
After 30 min	**Sn**	**17 %**	**15 %**	**15 %**	**14 %**	**13 %**
	C (Total)	**50 %**	**57 %**	**56 %**	**61 %**	**62 %**
	C-H	47 %	53 %	51 %	58 %	56 %
	C-O	1.3 %	2.6 %	3.3 %	1.0 %	3.8 %
	C=O	1.7 %	1.4 %	1.7 %	1.9 %	2.3 %
	O (Total)	**34 %**	**28 %**	**29 %**	**25 %**	**25 %**
	O-Sn	25 %	21 %	20 %	18 %	18 %
	O-C/O-H	9.0 %	7.3 %	8.8 %	7.6 %	7.6 %

CHAPTER 6:

SURFACE CHEMISTRY OF 2-PROPANOL ON SnO_2(110) STUDIED WITH AMBIENT-PRESSURE XPS

J. Trey Diulus, Rafik Addou, Gregory S. Herman*

School of Chemical, Biological and Environmental Engineering, Oregon State University, Corvallis, OR, 97331, USA

*Corresponding Author

Manuscript in preparation

6.1 ABSTRACT

Tin dioxide (SnO_2) has been used for a wide range of applications due to its unique surface properties. The performance of SnO_2 can be strongly influenced by the Sn oxidation states on the surface. Recently the oxidation of volatile organic compounds (VOC) has been demonstrated using SnO_2, where 2-propanol (IPA) was used as a VOC probe molecule. In this study we have used near ambient pressure X-ray photoelectron spectroscopy (NAPXPS) to characterize the surface chemistry of IPA on a well-defined stoichiometric SnO_2(110). The prepared surface chemistry and structure were characterized with NAPXPS and low energy electron diffraction, respectively. NAPXPS was performed for IPA pressures up to 1 mbar and mixtures of IPA and O_2. These measurements allowed us to determine the chemical states of adsorbed species on the SnO_2(110) surface over a wide sample temperature range. We found that both the IPA/O_2 ratio and the sample temperature strongly influence the reaction chemistry. We found that reduction of the surface occurs when no ambient oxygen source is present as indicated by an increase in the Sn^{2+}/Sn^{4+} ratio. Based on these studies we have developed a reaction model that describes the oxidation of IPA on SnO_2(110) surfaces.

6.2 INTRODUCTION

Tin dioxide (SnO_2) is widely used for a range of applications, specifically as a gas sensor,[10,36,37,38] transparent conductor,[10,36] and oxidation catalyst.[10,11,12,36,40] All of its applications are based on the ability to easily reduce the oxidation state of the tin ions, which changes the materials conductance or creates reactive defects. The ideal

stoichiometric SnO_2(110) surface contains rows of bridging O atoms than can be removed simply by applying thermal energy or through ion bombardment.[36] When the bridging O atoms are removed, the oxidation state of the surface changes from exclusively Sn^{4+} to a mixture of Sn^{2+} and Sn^{4+}.[10,36] SnO_2 has been studied for the oxidation of CO, where the surface Sn^{2+}/Sn^{4+} ratio was found to strongly influence the catalytic activity.[10,122] Recently, SnO_2 has also been studied for the oxidation of volatile organic compounds (VOC), where the oxidation of 2-propanol (IPA) to CO_2 and H_2O was used to characterize the activity of the catalyst.[11]

VOCs are a primary pollutant in the atmosphere and have been shown to be correlated to brain and other nervous system cancers.[123] Many people are subject to IPA exposure as it is largely used in laboratories and industries as a cleaning solvent or antimicrobial agent.[124] A potential route to reduce environmental pollution from IPA is by combusting it to non-toxic molecules, however this reaction is thermodynamically expensive.[11] Literature has shown that metal oxide or metal oxide supported materials can be effective for the oxidation of VOCs at lower temperatures.[11,125,126,127,128] For example, a stainless steel tube with SnO_2 deposited on the surface has been shown to achieve 100% conversion of IPA at ~550 K, compared to a maximum of only ~50% conversion at 673 K on clean stainless steel using a reactive mixture of 1000 ppm IPA/20% O_2/9.9% He/70% N_2.[11]

While metal oxide and supported oxide materials have been well studied from a catalysis perspective, the mechanism for alcohol oxidation on pristine surfaces is still not fully understood.[126] The role of O_2 in alcohol oxidation has been debated between numerous pathways. The O_2 can either directly react with the surface or only with the

adsorbates on the surface.[126] In order to gain a fundamental understanding of alcohol decomposition, studies using well-defined surfaces and controlled alcohol exposures are essential. Obtaining a detailed reaction model for alcohol decomposition and oxidation allows for improvements in catalyst design.

In this study, we have used near ambient pressure X-ray photoelectron spectroscopy (NAPXPS) to further understand the surface chemistry of IPA on a well-defined SnO_2(110) surface. The stoichiometric surface was characterized using NAPXPS and low energy electron diffraction (LEED). NAPXPS was additionally performed to determine the effect of IPA pressure and sample temperature on the adsorbed species. Mass spectrometry was used to measure gas phase products and estimate the conversion of IPA to CO_2. Additionally, we have developed a mechanism that describes the oxidation of IPA on a SnO_2(110) surface.

6.3 EXPERIMENTAL

A 10x10 mm^2 natural SnO_2(110) (±0.5°) single crystal was purchased from SurfaceNet GmbH. The crystal was sonicated in IPA (ACS grade, >99.5%) for 5 min and mounted to a Ta sample holder. The sample holder had a type K thermocouple which was spot welded next to the sample. The sample was loaded into a SPECS NAPXPS system with a base pressure of $<2x10^{-10}$ mbar. Numerous cycles of Ar^+ sputtering at 1 kV for 600 s with a 1.5 μA sample current were performed with the sample at room temperature (RT). This procedure was followed by flashing to 700 K. This process was performed until no impurities were detected at the surface while using XPS.

The stoichiometric oxidized surface was prepared by Ar^+ sputtering for 600 s at RT flowed by annealing in the NAP cell to 580 K in UHV. The sample was then held at this temperature while O_2 was added to the cell until the O_2 pressure (P_{O_2}) was 1 mbar. The sample was oxidized by under these conditions for 10 min. The cell was pumped to UHV and the sample was then flash annealed to 780 K. Once the temperature cooled back to 600 K, the P_{O_2} was increased to 1 mbar. A second oxidation step was performed for 10 min at $P_{O_2} = 1$ mbar and 580 K. The sample was then cooled to 380 K while keeping the pressure at $P_{O_2} = 1$ mbar. The cell was pumped to UHV and then further cooled to RT. This process was performed to prevent any potential oxygen vacancies at the surface.

A SPECS ErLEED 150 was used to collect diffraction images of the prepared surface. A cathode current of 1.3 A and screen voltage of 5 kV were used. The beam energy was set to 90 eV, yielding a beam current of 1.1 uA. The sample was moved across the sample surface to ensure uniformity, which was performed by observation of a consistent LEED pattern. Beam energies 60 and 135 eV were additionally used to verify no surface reconstruction.

Ultraviolet photoemission spectroscopy (UVS) was collected using a SPECS UVS 10/35 operating at 1 x 10^{-7} mbar of He. XPS data were obtained using a SPECS XR 50 μ-Focus X-ray source with monochromatized Al Kα radiation (hν = 1486.6 eV, 50W, 15kV), an electron analyzer pass energy of 35 eV, and normal emission. Valence-level spectra were collected to verify the oxidation state of the surface.

For near ambient pressure IPA experiments, IPA was loaded in a glass bulb and several freeze-pump-thaw cycles were used to degas the IPA. A sequence of the C 1s, O 1s and Sn 3d core levels, Sn MNN Auger transition and valence-level spectra were obtained at each temperature and pressure. All XPS data were charge corrected to the C 1s aliphatic carbon binding energy (E_b) at 284.8 eV. The spectra were fit using Gaussian-Lorentzian line shapes and a linear background.

6.4 RESULTS AND DISCUSSION

Once a stoichiometric surface was prepared, LEED was used to characterize the surface structure. Figure 6.1 shows the 1x1 diffraction pattern for the SnO_2(110), which is consistent with an unreconstructed surface and prior literature.[129] An idealized model of the stoichiometric surface is also shown in Figure 6.1. Valence-level band spectra (Figure 6.2) were initially obtained using both XPS (a) and UPS (b) to confirm the surface oxidation state. The oxidized XPS valence spectra shows three main peak shapes followed by a steep drop around 4 eV, which was also consistent with literature.[130] The ion bombarded surface has an obvious edge feature in the band gap, that extends to ~2 eV. This is due to the presence of reduced tin on the surface from oxygen deficiencies.[131]

NAPXPS were collected for C 1s, O 1s, Sn 3d, Sn MNN and the valence band for the oxidized surfaces at RT with P_{IPA} = 0.1, 1, and 3 mbar. Spectra were also obtained while pumping IPA from the cell, and after transferring the sample to UHV. Figure 6.3a shows the C 1s spectra for the indicated sample conditions. No significant changes were observed for Sn 3d or Sn MNN spectra. During IPA exposure, adsorbed species were observed on the surface starting at P_{IPA} = 0.1 mbar. The adsorbed species

are stable on the surface, both during exposure and after pumping out the IPA. Gas phase C 1s peaks for IPA becomes apparent for P_{IPA} = 0.1 mbar, and overlaps with the adsorbed carbon peaks. We deconvoluted the spectra by constraining the area ratio of C-H:C-O to be 2:1 and fixing the full width half maximum to be identical for both peaks. No significant change occurs for different IPA pressures, other than an increase in overall peak area corresponding to an increase in adsorbate coverage. No change was seen in valence-levels for either surface after exposure to IPA, which suggests that IPA does not significantly change the surface oxidation state of SnO_2 at RT. Figure 6.3b shows the O 1s spectra for the oxidized surfaces at RT with P_{IPA} = 0.1, 1, and 3 mbar. A high E_b shoulder (~532.4 eV) is seen after oxidation possibly due to hydroxyls on the surface or adsorbed O_2.[74,132] No significant changes in the O 1s spectra take place as the IPA pressure is increased.

To study the decomposition of IPA on the stoichiometric surface, NAPXPS was performed at elevated temperatures. Initial studies focused on exposure to IPA only. The results are shown in Figure 6.4, for P_{IPA} = 0.5 mbar and T = 400, 500, 600 K. A pressure of 0.5 mbar was chosen since the C 1s intensity from the adsorbed species was significantly higher that C 1s intensity from the gas phase peaks, which allowed relatively straight forward deconvolution of the spectra. Figure 6.4a shows the C 1s spectra where the C-H:C-O ratio was again constrained to 2:1 for both adsorbed and gas phase species. No difference was seen at 400 K compared to the RT studies shown in Figure 6.3. At 500 K, a new higher energy peak (brown) is evident at E_B = 290 eV, which suggests the presence of a gas phase C=O species.[74,132] Once 600 K is reached, another peak (teal) forms at E_B = 288 eV, while the peaks associated to adsorbed IPA

(C-H blue, C-O red) significantly decreased. This new peak is associated with acetone that is adsorbing to the surface. No significant changes were detected in the O 1s spectra for Figure 6.4b for all the experimental conditions. In the valence band spectra shown in Figure 6.4c, we see that the surface is being slightly reduced as the band edge increases with temperature. This is a result of oxygen vacancies being formed through reactions with IPA at 600 K, leading to only a partial conversion of IPA to acetone.

By retracting the sample slightly during exposure, only the gas phase spectra are collected. In Figure 6.5, we show the gas phase spectra for C 1s (a) and O 1s (b). A small amount of C=O species (green) are initially present at 400 K in the C 1s spectra. As the temperature is increase, evidence of C=O is seen in both the C 1s and O 1s. Annealing to 600 K, we see a decrease in the C-O peak, as well as an increase in C=O for both the C 1s and O 1s spectra. We also see a new peak (green) at E_B = 533.8 eV in the O 1s spectra that is attributed to O-H, suggesting the formation of water.

Mass spectrometry was utilized to measure the partial pressures of gasses flowing out of the NAPXPS cell and into the analyzer to obtain further information of the chemical reactions. Figure 6.6 shows mass spectra for acetone (m/z 58, 43), CO_2 (m/z 44), water (m/z 18), hydrogen (m/z 2), oxygen (m/z 32), and IPA (m/z 45). At 400 and 500 K, no change was observed for the IPA signal. This is likely due to lower sensitivity compared to the products due to the mass spectrometers distance from the reaction cell. Once 600 K was reached, a noticeable change in the mass spectrometers signal was observed, where the IPA signal significantly decreased and the acetone and water signals increased. This correlates well with the XPS results and suggests acetone is indeed being formed through interaction with SnO_2. One concern during the studies

was the potential for the heater filament decomposing IPA as opposed to the SnO_2. In order to eliminate this possibility, we ran background experiment where the SnO_2 sample was not mounted on the sample holder. The mass spectrometer data from the background experiment was then subtracted from the experiment with the SnO_2 sample. Using the ratios of each mass to the IPA signal, the background spectra was subtracted and plotted in Figure 6.6. This subtraction method does not work ideally for dynamic changes in temperature, where the filament is temporarily hotter due to ramping, as such the data obtained during temperature changes do not represent the experiment. Additionally, moving the sample back for gas phase measurements (done towards the end of each temperature) affects the flow rate of gas through the cell leading to the slight change in IPA intensity which is observed just before each temperature change as seen in Figure 6.6.

Since we saw the surface being reduced during exposure to P_{IPA} = 0.5 mbar, we repeated the same experiment with 9:2 ratio of O_2:IPA which is based on the stoichiometry for the complete oxidation of IPA. Figure 6.7 shows the C 1s (a), O 1s (b) and valence band spectra (c) for P_{IPA}= 0.2 mbar and P_{O_2}= 0.9 mbar. At 400 K we already see the presence of C=O gas phase species. At 500 K we already see a similar spectra to Figure 6.4a, where C=O forms on the surface as the C=O gas phase peak increases and the C-O gas phase peak decreases. Once the cell is pumped to UHV, there is evidence of carboxylic acid (yellow) and acetone (teal) on the surface which were not seen in Figure 6.4a. Again, no significant conclusions can be drawn from the O 1s data. The valence band spectra also shows a different response in mixed IPA/O_2. We

see that little to no reduction of the SnO_2 surface occurs when an oxygen ambient is present, suggesting that oxygen vacancies from exposure to IPA are being replenished by the ambient oxygen.

We can additionally look at the gas phase XPS spectra for the 9:2 P_{O_2}:P_{IPA} ambient to analyze the reaction products. Figure 6.8 shows the gas phase spectra for C 1s (a) and O 1s (b). At 400 K, not much is different compared to the experiment with just IPA. At 500 K, the decrease of C-O, and increase of C=O is similar to the 600 K spectra with P_{IPA}= 0.5 mbar. Increasing to 600 K we can see the presence of a CO_2 gas phase peak at E_B = 294 eV. The O 1s also shows a doublet at E_B = 538 and 540.5 eV which corresponds to gas phase O_2. At 500 K, the spectra resembles the 600 K exposure with P_{IPA}= 0.5 mbar, similar to C 1s, where the presence of C=O and O-H gas phase peaks are present. At 600 K, we can see the presence of a new CO_2 peak (purple).

Mass spectrometry was additionally used for the 9:2 P_{O_2}:P_{IPA} exposure. Figure 6.9 shows the mass spectra for 9:2 P_{O_2}:P_{IPA} tracking the same masses as in Figure 6.6. No detection of reaction products were seen at 400 K. When annealed to 500 K, we see a decrease in IPA, and an increase in the water and acetone signals, with only a trace amount of CO_2 present. At 600 K, the IPA continues to decrease and water continues to increase. The acetone decreases slightly while a significant increase in CO_2 is also seen. During the entire experiment, the amount of O_2 is consistently decreasing. However, when the sample is allowed to cool the IPA and O_2 increase to nearly their original starting pressure. As the IPA oxidation takes place, ambient the O_2 is being consumed.

The role of oxygen in this reaction mechanism can be assumed to follow a Mars-van Krevelen mechanism.[40,42] Figure 6.10 shows a cartoon diagram for the suggested mechanism of IPA oxidation on stoichiometric SnO_2(110). First the IPA adsorbs to the surface, where the oxygen in the IPA binds to a Sn site and donates the hydrogen from the alcohol group to the bridging oxygen. When enough thermal energy is provided to the surface, the alpha carbon in the IPA can donate its hydrogen to another bridging oxygen. This then results in the formation of acetone that can desorb from the surface. Then either the protonated bridging oxygens can react to form water and an oxygen vacancy, or two hydrogens can combine to form molecular hydrogen. Both water and molecular hydrogen can then desorb from the surface. As noted, the bridging oxygens are consumed overtime through adsorption and reaction of IPA and desorption of water. Due to the limited amount of oxygen available at the surface only the partial oxidation of IPA to acetone occurs. If there is ambient oxygen present, these bridging oxygen vacancies can be replenished allowing for acetone desorption at lower temperatures. Additionally, adsorbed IPA can react with adsorbed O_2 forming acetic acid, CO intermediates, and ultimately CO_2.

NAPXPS studies in multiple environments provide significant insight towards the reaction mechanism for IPA combustion of CO_2 on the stoichiometric Sn(110) surface. A Mars-van Krevelen mechanism is suggested due to the inability to achieve full combustion of IPA without an ambient oxygen source. Obtaining basic knowledge of the chemical mechanism for alcohol combustion is extremely useful to the catalysis community.

6.5 CONCLUSIONS

We have shown that IPA adsorbs to a stoichiometrically prepared SnO_2(110) following exposures to P_{IPA} = 0.5 mbar at 400 K. Increasing the temperature to 600 K leads to the conversion of IPA to acetone. Using O_2:IPA ratios equivalent to 9:2 results in the formation of acetone at 500 K. Further increasing the reaction temperature to 600 K at the 9:2 O_2:IPA ratios leads to the rapid depletion of oxygen along with the formation of acetic acid and carbon monoxide intermediates. Once the oxygen is replenished, CO_2 and water are formed. This suggests a Mars-van Krevelen mechanism for the oxidation of IPA on stoichiometric SnO_2(110).

6.6 ACKNOWLEDGEMENTS

This research was funded by the Center for Sustainable Materials Chemistry (CSMC) supported by the U.S. National Science Foundation under grant number CHE-1606982. This work was performed, in part, at the Northwest Nanotechnology Infrastructure, a member of the National Nanotechnology Coordinated Infrastructure, which is supported by the National Science Foundation under grant number NNCI-1542101. Acquisition of the Ambient-Pressure X-ray Photoelectron Spectroscopy/Ambient-Pressure Scanning Tunneling Microscopy system was supported by the National Science Foundation-Major Research Instrumentation program (grant DMR-1429765), the M. J. Murdock Charitable Trust, Oregon BEST, Oregon Nanoscience and Microtechnologies Institute, and Oregon State University.

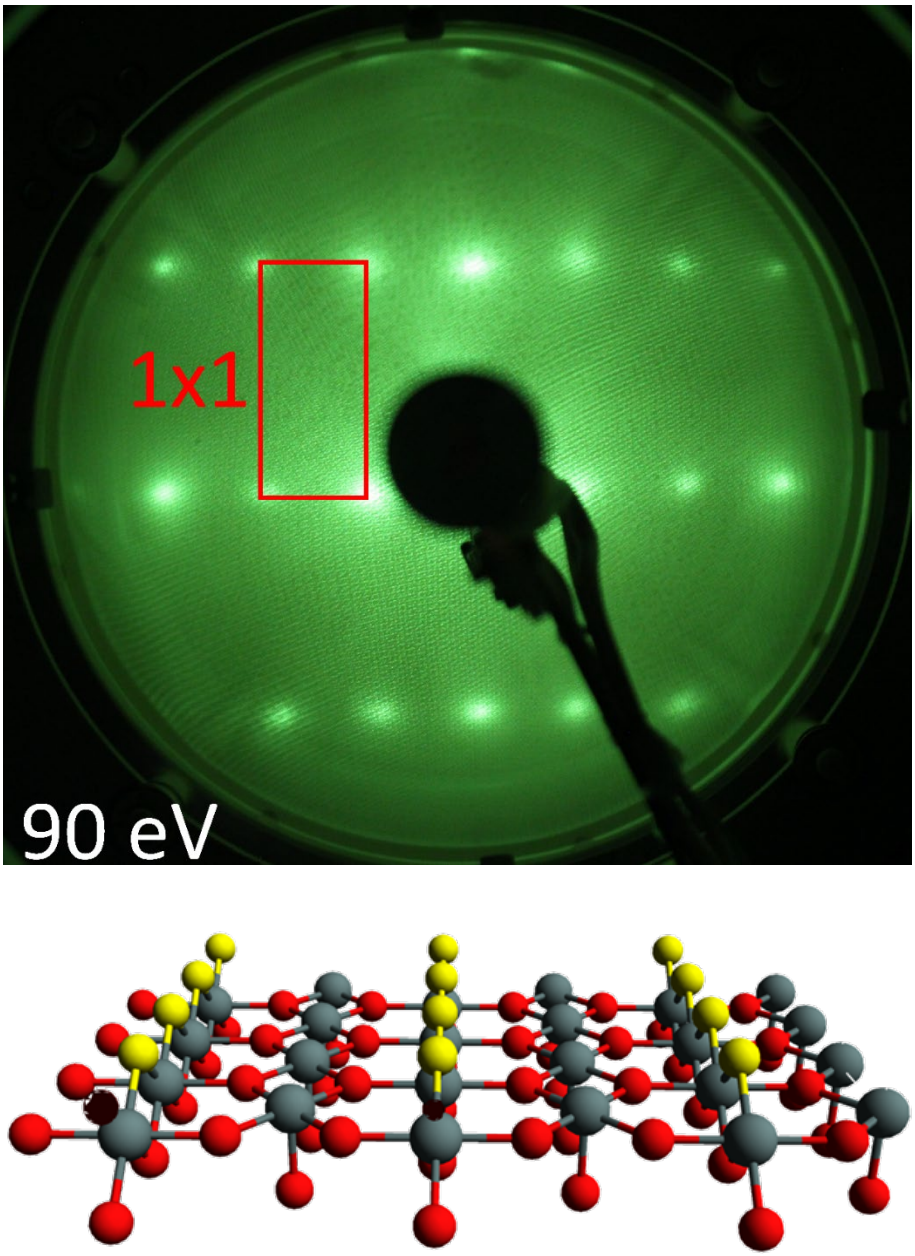

Figure 6.1. A photographed image of a LEED pattern for the prepared stoichiometric surface using an electron energy of 90 eV. A visible 1x1 pattern is highlighted in the red box. The suggested ideal surface structure is shown in the cartoon below, with Sn (grey), O (red), and bridging O (yellow) atoms.

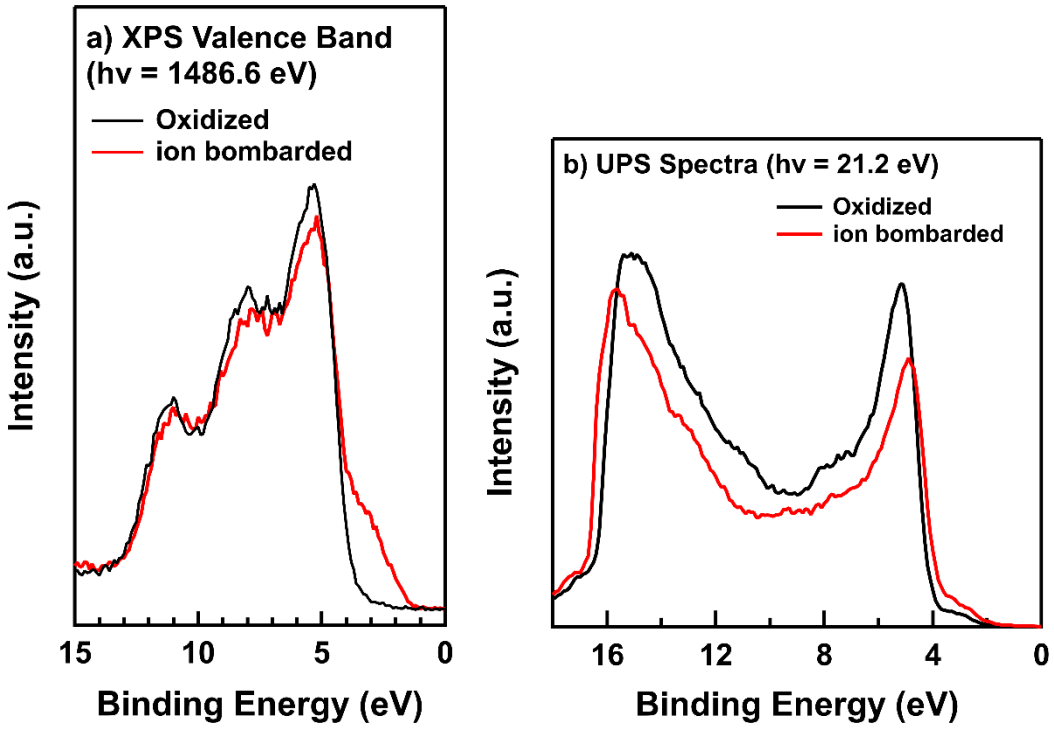

Figure 6.2. Valence band spectra using both monochromated Al kα X-rays (a) and He I UV light (b) for both the oxidized stoichiometric surface (black) and the reduced ion bombarded surface (red).

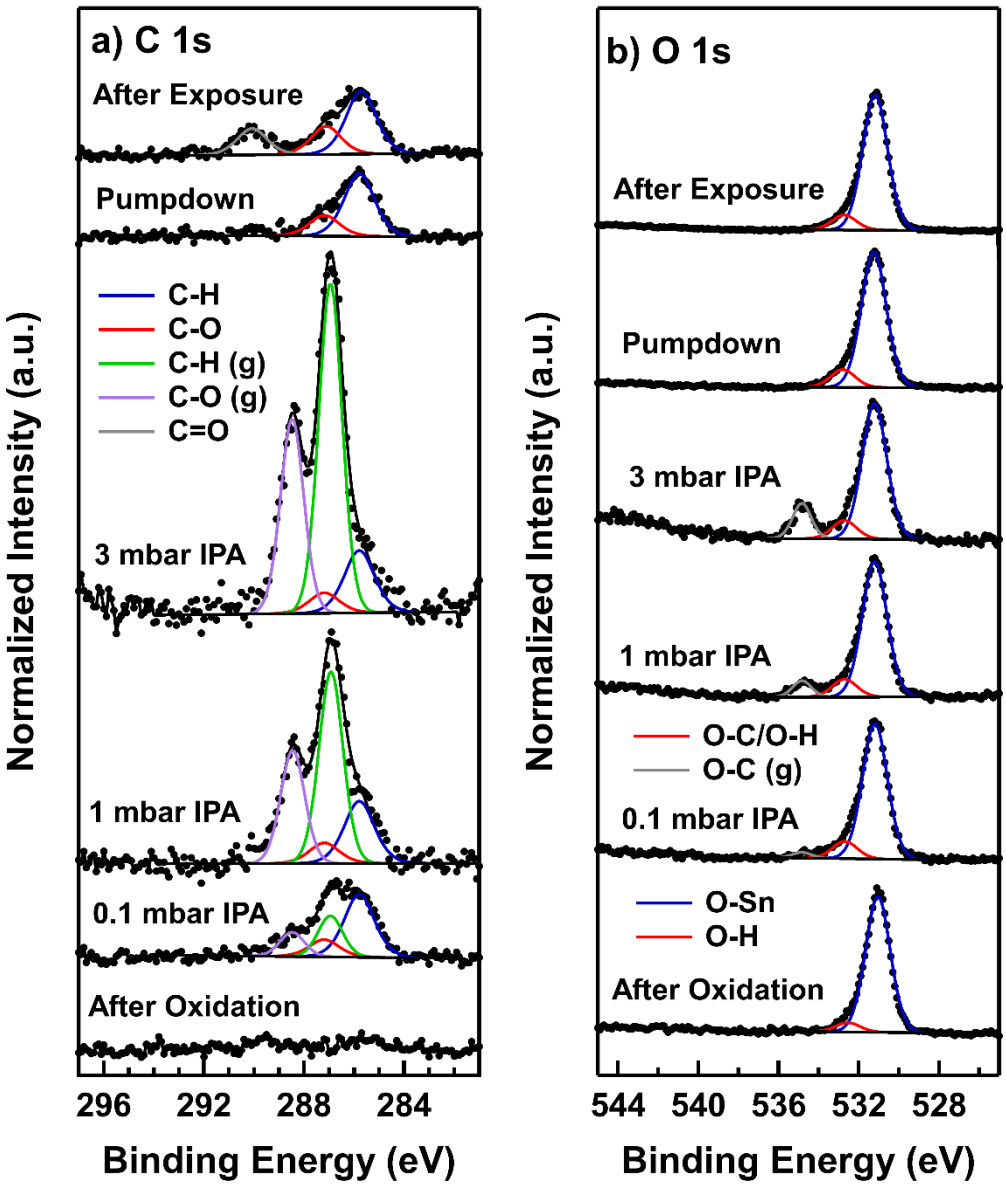

Figure 6.3. XPS of C 1s (a) and O 1s (b) of stoiciometrically oxidized SnO_2(110) after exposures to P_{IPA} = 0.1, 1, and 3 mbar at room temperature.

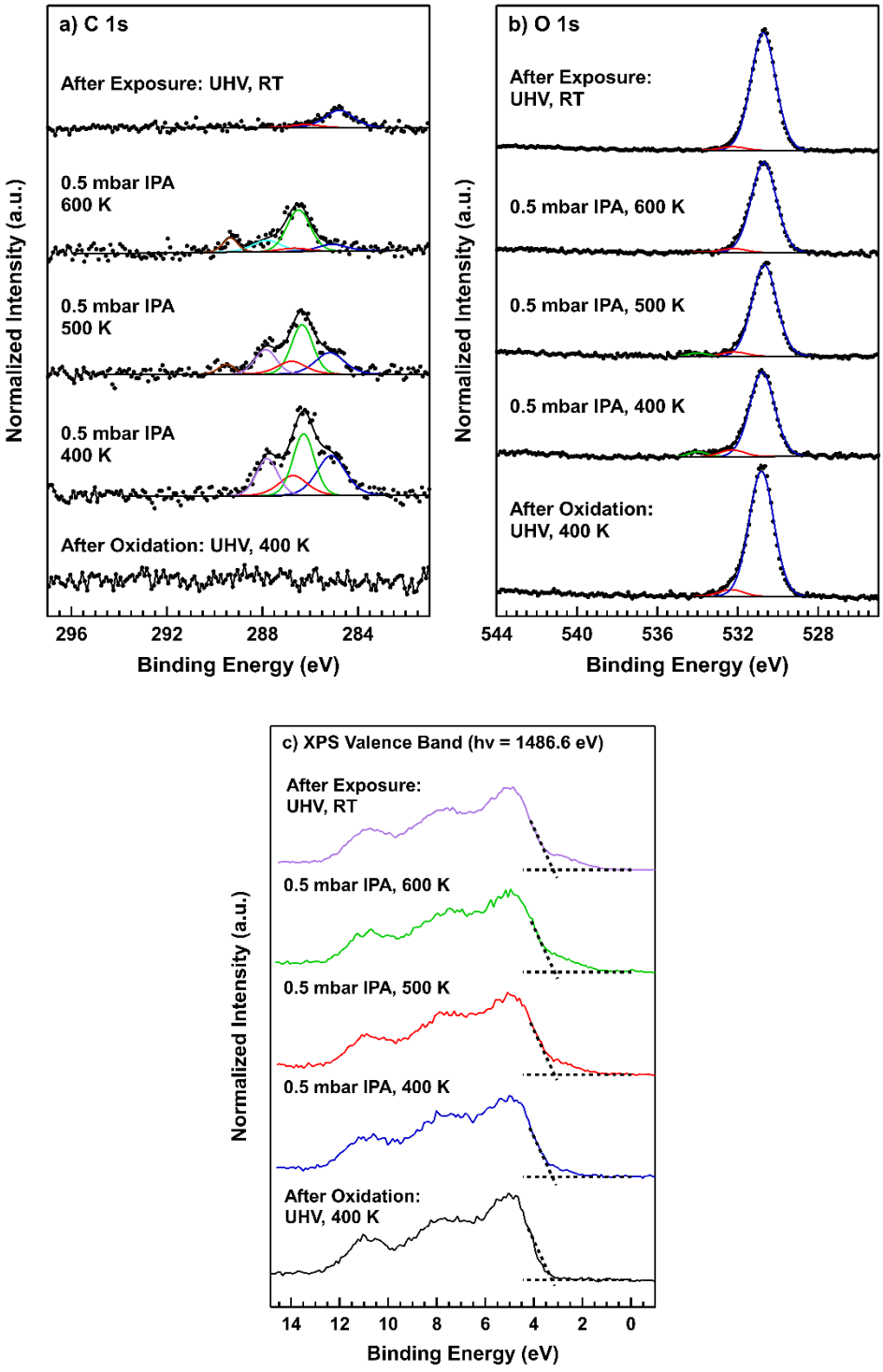

Figure 6.4. NAPXPS of C 1s (a) and O 1s (b) at P_{IPA} = 0.5 mbar for 400, 500, and 600 K, as well as after exposure at UHV.

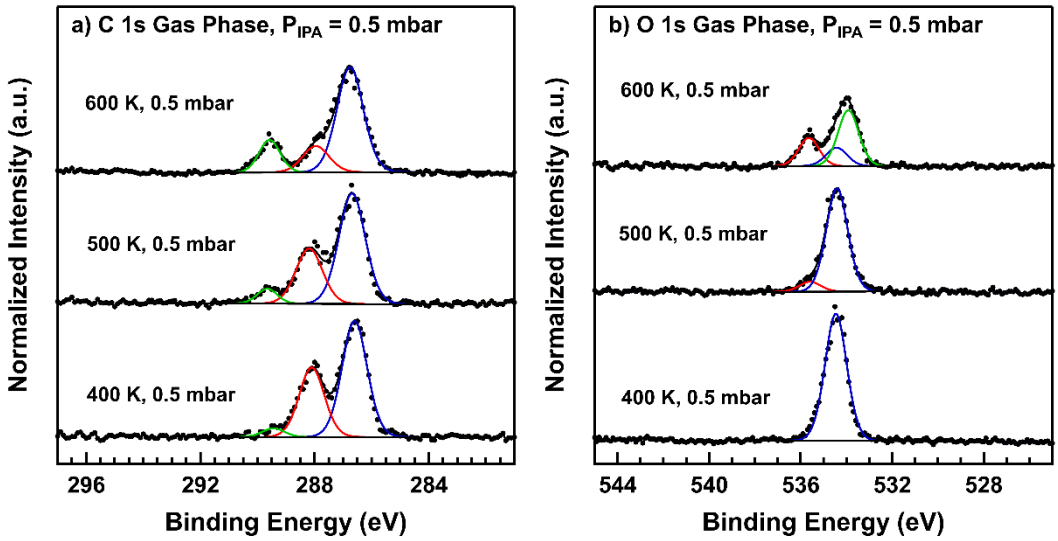

Figure 6.5. Gas phase NAPXPS spectra of C 1s (a) and O 1s (b) at P_{IPA} = 0.5 mbar for 400, 500, and 600 K.

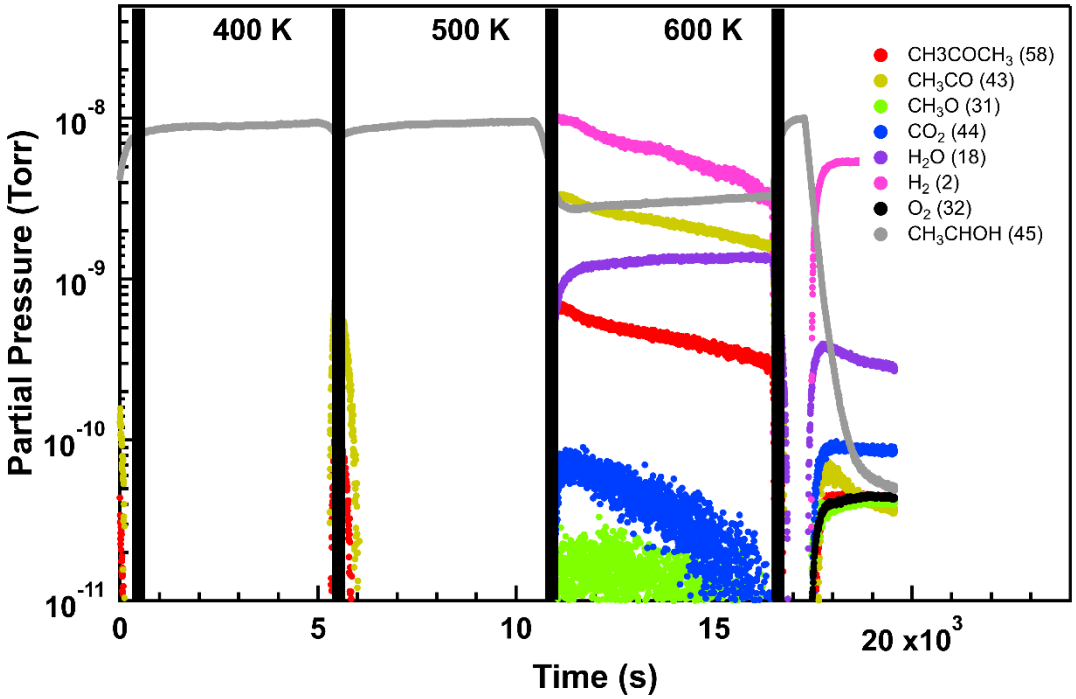

Figure 6.6. Subtracted mass spec data for acetone (m/z 43, yellow and m/z 58, red), CO_2 (m/z 44, blue), water (m/z 18, purple), hydrogen (m/z 2, pink), O_2 (m/z 32, black), and IPA (m/z 45, grey) at P_{IPA} = 0.5 mbar.

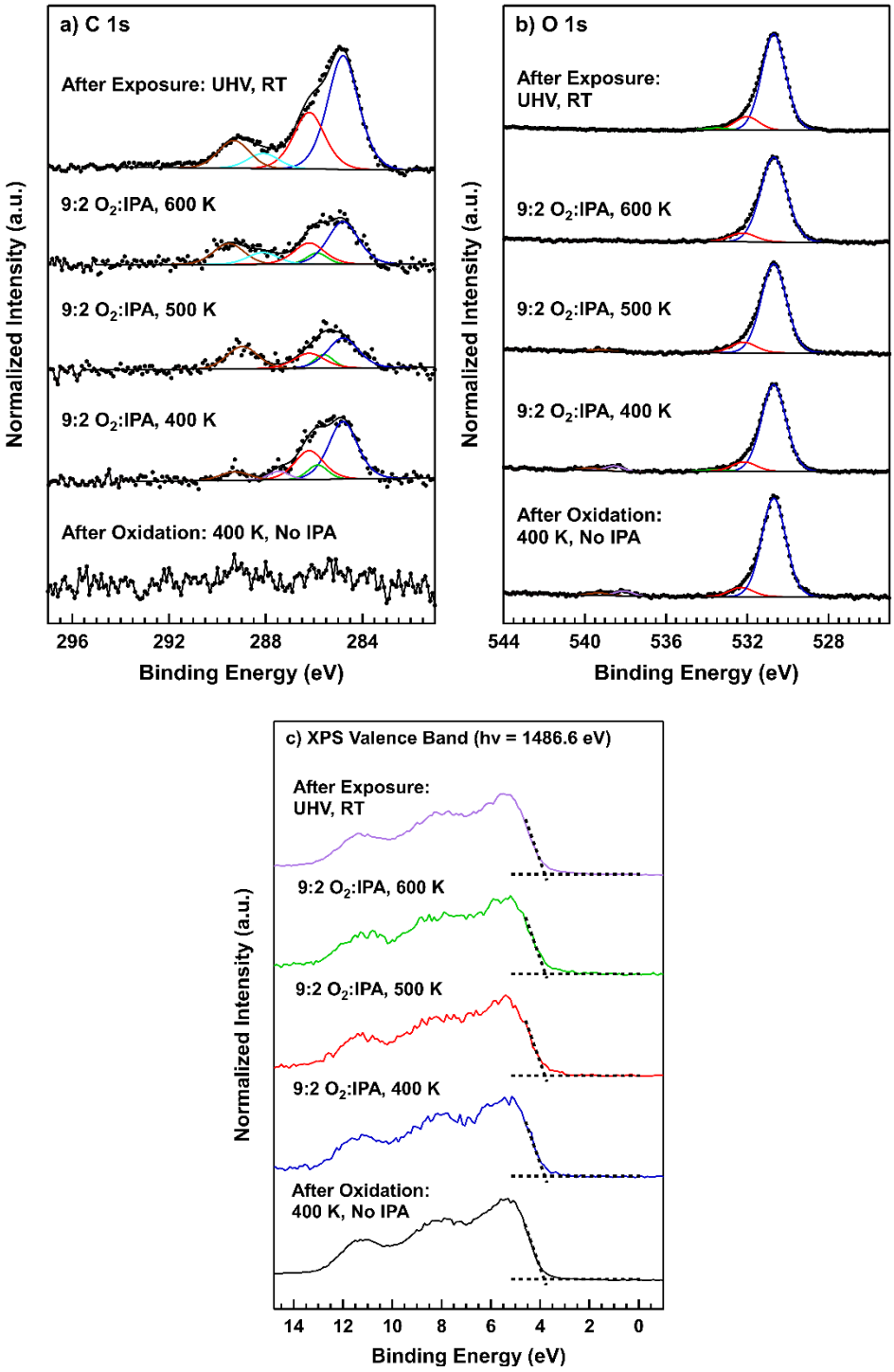

Figure 6.7. NAPXPS of C 1s (a) and O 1s (b) at 9:2 P_{O_2}:P_{IPA} for 400, 500, and 600 K, as well as after exposure at UHV.

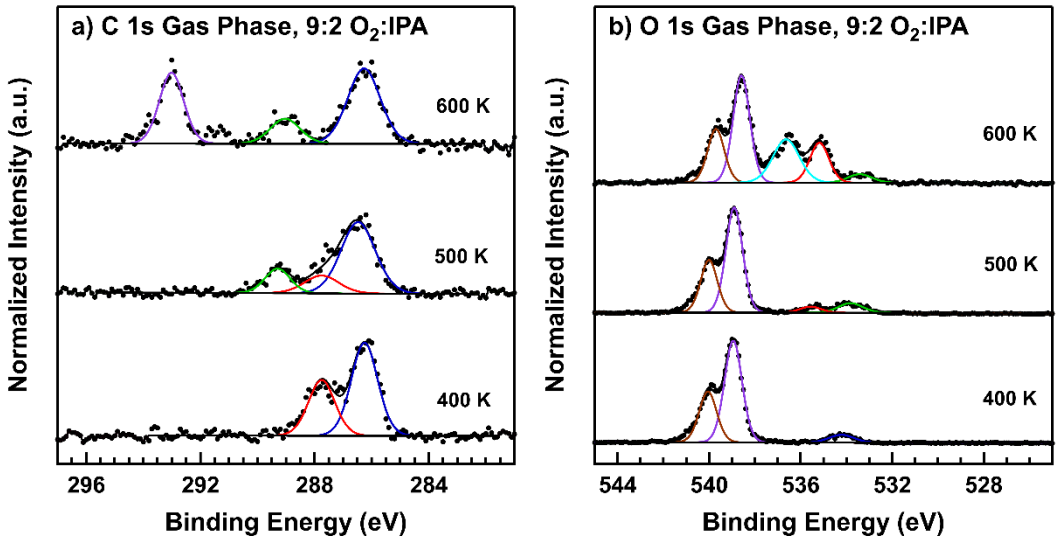

Figure 6.8. Gas phase NAPXPS spectra of C 1s (a) and O 1s (b) at 9:2 P_{O_2}:P_{IPA} for 400, 500, and 600 K.

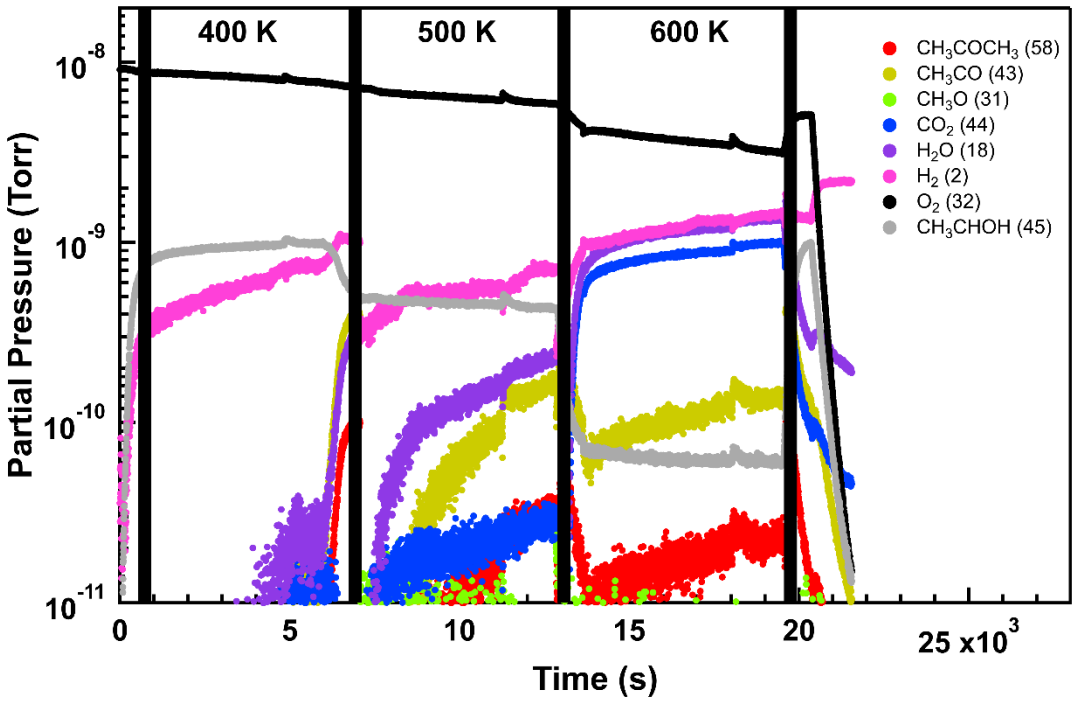

Figure 6.9. Subtracted mass spec data for acetone (m/z 43, yellow and m/z 58, red), CO_2 (m/z 44, blue), water (m/z 18, purple), hydrogen (m/z 2, pink), O_2 (m/z 32, black), and IPA (m/z 45, grey) at 9:2 P_{O_2}:P_{IPA}.

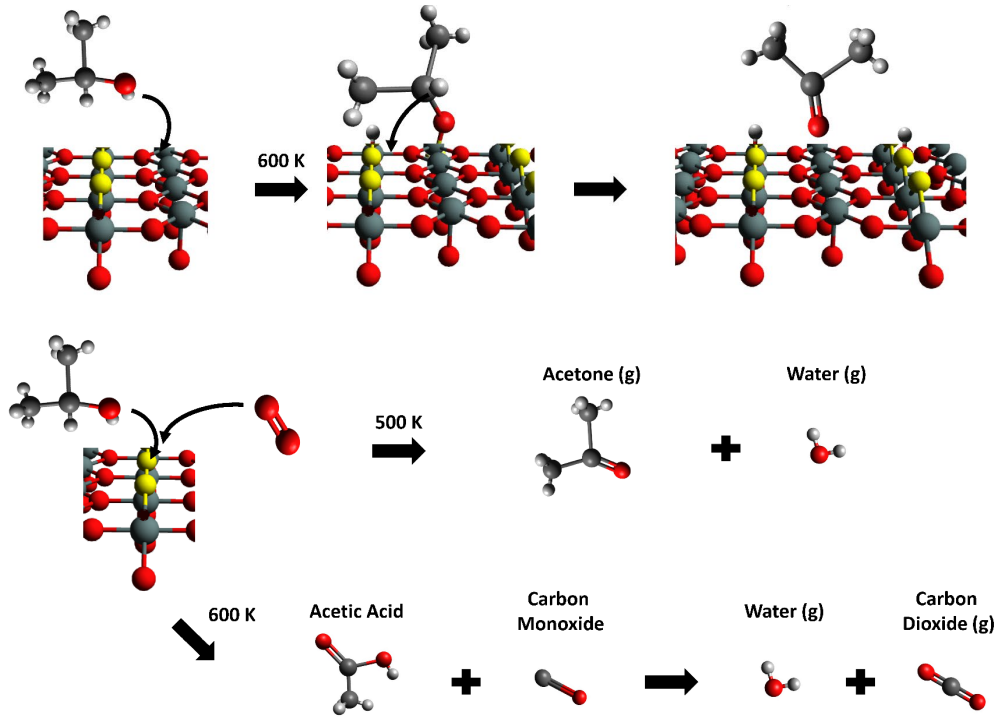

Figure 6.10. Cartoon diagram of the mechanism for IPA adsorption and decomposition on a stoichiometric $SnO_2(110)$ surface.

CHAPTER 7:

CONCLUSIONS AND FUTURE DIRECTIONS

7.1 ORGANOTIN PHOTORESISTS

Surface characterization of organotin thin films combined with ambient, contrast, and annealing studies have provided significant knowledge and led to a proposed mechanism for how tin-based nanocluster resists behave through the patterning process. In chapter 3, we proposed standard characterization methods for new resist materials through the use of AFM, ellipsometry, TPD, ESD, and XPS. These methods allow the study of film morphology, thermal stability, radiation sensitivity, and chemical composition. Chapter 4 focused on radiation induced mechanistic studies through use of XANES and NAPXPS to further confirm the role of electrons in the reaction mechanism and also to try and better understand what reaction products were formed following exposure. In chapter 5, contrast studies provided benchmark sensitivity comparisons, which led to suggestions on improvements for processing and material designs. Finally, annealing studies in chapter 5 provided insight towards the chemical composition of the resulting films post exposure, drawing further conclusions and proposing a full mechanism for the overarching patterning process.

There are still a few characterization studies that could be performed to provide further insight or knowledge about these resist materials. Currently, no chemical composition studies were completed following the full development process. As stated in chapter 5, a significant amount of carbon is still found leftover in the developed film. This is not ideal as the design of the materials were specifically intended to form a metal oxide matrix where most of the carbon originally in the film is removed after development. While annealing studies were able to suggest that significant carbon is left behind, these studies were all done in a controlled vacuum system with maximum

pressures of 1 mbar and therefore not directly correlated with annealing in ambient air. Ambient anneal studies were only performed in 1 mbar of each molecule as this was a safe system pressure for the molecules used. Comparing to air, higher partial pressures would need to be achieved, namely ~200 mbar O_2, ~20 mbar D_2O, and ~730 mbar for N_2. Additionally, since there was evidence of some reduction mechanism taking place through interactions with D_2O, studying mixtures of gasses would determine if an alternative mechanism may occur. Mixing 10:1 O_2:D_2O for annealing studies (a ratio similar to that of air) would be interesting to see if the extra oxygen leads to increased oxidation through hydroxyl species instead of any reducing reactions. Other mixtures, possibly including N_2, may also be useful in shedding light on the chemistry occurring during the PEB.

Following annealing the thin film, the next step is to develop the sample. The goal would be to determine what further changes occur to the films, especially on the surface, after the film is immersed in developer solution. Unfortunately, there are numerous challenges to determining the true composition after exposure to the developer solution. The most straightforward compositional study would be to remove the film from vacuum following exposure and anneal, develop the film *ex-situ*, and then reload the sample in vacuum and measure the composition. However, once a sample is removed from vacuum, the surface composition can drastically change. Additionally, since the development process requires dissolving unexposed areas by immersing the entire film in organic solvents, some carbon will inherently be left behind on the remaining film. X-ray photoelectron spectroscopy is only able to measure a distribution of chemical components, which would make it difficult to separate between film carbon

and what carbon was left behind following development or other adventitious carbon. Alternatively, the use of IR spectroscopy would be a great way to pinpoint specific binding stretches that are characteristic to the film carbon versus the contamination from developer solution or air. With IR spectroscopy, baseline spectra can be subtracted from each measurement, unlike with XPS, providing for a more accurate depiction of the true film chemistry. This would require collecting IR spectra at numerous points during the development process, namely before and after exposure, after the PEB, and after developing the film. These measurements can be done either in atmosphere or more ideally in a controlled environment with a vacuum system. Yves Chabal's group in UT Dallas has established a reliable method to study resist thin films *in-situ* via transmission IR spectroscopy.[133] Dangerfield et al. were able to investigate interfacial chemistries and pinpoint the loss or gain of specific methoxy or hydroxyl vibrational modes for the γ-$NaSn_{12}$ resist. Transmission IR would also be useful to combine with current XPS studies in all prior experiments, not only just for development studies. In the future, a similar setup for IR spectroscopy can be mounted onto the Specs NAPXPS system at Oregon State, allowing for the complete surface characterization and mechanistic study of a resist material *in-situ*.

Resist composition could also be studied through thermal studies combined with spectroscopic compositional studies to draw further conclusions on the chemical changes occurring before, during, and after desorption processes. For example, XPS and/or IR spectroscopy could be collected at three temperatures; just after water desorption ~150 °C, just before the butyl desorption peak ~300 °C, and then just after butyl desorption ~400 °C. TPD has already shown that butyl groups are leaving the

film, but no studies have been performed to determine the chemical information of what remains after butyl desorption. If desorbed butyl ligands are finding their way back to the film by adsorbing to the surface, this could contribute to why only ~20% of carbon is removed post exposure. Tracking the stability of an exposed film is also important for PEB studies. Chapter 5 only discusses the composition changes following anneals to 170 °C as this is the temperature used for the PEB. It would also be interesting to see if the film chemistry changes further with exposure to higher temperatures, as this may suggest a different PEB temperature. Previously, the PEB temperature was determined by analyzing the resist contrast and line edge roughness through e-beam exposure in a scanning electron microscope (SEM) using temperatures that are commonly for metal oxide resist PEBs.[121] However, for organotin, it is possible that even higher temperatures could be effective for a PEB since TPD studies show the pre-exposed films are thermally stable to up to ~350 °C. XPS and/or IR should also be collected for post exposed films at temperatures >170 °C. The key aspects to look for would be whether the oxygenates (C-O and C=O) are eventually removed at higher temperatures, or if they form permanent contamination in the film. The O-C peak in the O 1s spectra would also provide more information on oxygenates in the film. Other important features would be whether carbon can be completely thermally removed, if so at what temperature, and does the Sn change oxidation state during high temperature anneals > 400 °C.

Thermal studies for post exposed films can also be achieved through mass spectrometry studies instead of spectroscopic studies. This would have to be done using a different X-ray source than what has been used for other exposure studies stated in

this dissertation. Specifically for monochromated X-ray sources, only a small spot (0.3-1 mm) is exposed on the sample while the rest remains unexposed. If TPD were to be done on a sample like this, the unexposed regions would also desorb and complicate the analysis. Instead, a dual anode source, scanned monochromated X-ray source, or large scanned electron source would be required to expose the entire sample to radiation. Once exposed, a TPD experiment could be run to determine if the desorption profile is any different than pre-exposed films, followed by spectroscopic characterization of the remaining film. Based on the proposed mechanism, significantly fewer butyl ligands would desorb at the temperature seen for pre-exposed films. Otherwise, another likely result could be a distinctly different peak profile for m/z 41 desorption, possibly at a different temperature as well. This result, combined with spectroscopic analysis, would verify that polymerization occurs and now C-C bonds must be broken instead of solely C-Sn for the decomposition of the film. Another feature to look for would be if longer carbon chain desorption species are now detected with a mass survey. If no change is seen in the m/z 41 profile except for a slight reduction in signal intensity (correlating to the amount of carbon loss seen from annealing studies in chapter 5) this may contradict the suggestion that complete polymerization occurs. Instead it may suggest that not all C-Sn bonds are broken during the exposure process even though a solubility transition is still able to occur. Spectroscopic characterization of the remaining film would provide useful information.

Finally, studies with other organotin materials besides β-$NaSn_{13}$ would be beneficial as well. With organotin synthesis, different ligands can be substituted on nanoclusters in order to try and control the chemistry. While β-$NaSn_{13}$ was well utilized

as a model resist for studying radiation chemistries, adding additional or separate ligands could be useful in thermal studies following exposures. With bulkier and weaker bound ligands leftover in the proposed metal-oxide polymer post exposure, PEBs may then be able remove the carbon more effectively compared to what was seen with polymerized butyl ligands. Charged nanoclusters would also be interesting for post exposure thermal studies as the need for counterions could be utilized to control the chemistries following anneals. Overall, significant knowledge has been gained about the radiation-induced mechanism for organo-tin resists, however a full understanding of the chemical transformations that occur following exposure and anneal require more studies for complete understanding of the patterning process, leading to better designed materials for industrial applications.

7.2 TIN OXIDE CATALYSIS

Ambient pressure XPS studies of 2-propanol (IPA) interactions with SnO_2 determined a Mars-van Krevelen mechanism occurs for the oxidation of IPA to CO_2. Chapter 6 explains the differences between exposures to solely IPA compared to mixtures of O_2 and IPA. The oxygen was shown to be a necessary component to maintain the oxidation state of the surface of SnO_2, which is required to fully convert IPA to CO_2. However, this has only been determined for the oxidized stoichiometric SnO_2 surface. A reduced surface can also be prepared, where a 4x1 LEED pattern is formed instead of the 1x1 pattern seen with a stoichiometric surface. Preparation of a reduced surface, which requires significant removal of oxygen from the bulk of the SnO_2 crystal, would be an interesting alternate surface for IPA conversion studies.

NAPXPS studies have shown ambient oxygen is required for full conversion of IPA to CO_2, but no conclusions have been made on whether bulk oxygen 2-3 atomic layers beneath the surface is as important as ambient oxygen. With the reduced surface the top layer of bridging oxygen is no longer present, providing more available Sn sites for the IPA to adsorb to. However, the bridging oxygen likely plays a role in the acceptance of a proton during the decomposition of IPA. So it is questionable whether more Sn sites would increase or decrease adsorption of IPA. Since studies with only IPA led to a reduction of the SnO_2 surface and ultimately quenching the full conversion to CO_2, the reduced surface will likely not be advantageous versus the stoichiometric surface. There are additionally numerous surface terminations for SnO_2(110) that can be prepared,[10] however the most useful studies would be comparing the differences of IPA conversion on the stoichiometric 1x1 and the reduced 4x1 surface as they are essentially opposites.

Following XPS comparisons between both surfaces, combining STM studies to study the surface would provide more information about the mechanism for each surface preparation and reaction conditions. While LEED is an effective technique to determine the crystal surface structure, STM allows you to image the surface structure and identify defects, like facets or step-edges, and also see if any other contamination is still present that is undetectable by XPS and LEED. With the collection of STM after IPA exposure, atomic resolution images allow for the ability to determine the exact sites where IPA adsorbs to the surface. The coverage of IPA can also be directly determined using STM images instead of estimating the coverage from photoemission spectra. Obtaining a more accurate coverage would be useful to combine with reaction

chemistry studies through XPS and mass spectrometry measurements. Comparing IPA adsorption sites for the stoichiometric and reduced surfaces would further determine the role of bridging oxygen in IPA adsorption. Alternatively to imaging, surface tunneling spectroscopy (STS) can be utilized to measure the electron density of a surface, allowing for the calculation of the bandgap. Looking at bandgap changes following exposure to IPA for each surface or experiment conditions can be combined with valence band changes in XPS measurements to determine how the oxidation state of surface tin sites are changing.

STM can also be collected in ambient pressure and at elevated temperatures. This means that the same NAPXPS experimental conditions can be applied to the STM chamber where images can be collected. A series of images can also be stitched together to form a movie where one can observe the adsorbed IPA interacting with the atoms on the surface. One must consider the time scale of the reaction for creating a movie, as the reaction may be too quick to see intermediates. Instead, a separate experiment may be necessary where IPA pressure is stabilized and O_2 is slowly introduced as images are continuously collected. Alternatively, IPA and O_2 can be mixed and during imaging where O_2 is slowly quenched from the chamber. By changing the O_2 pressure, the reaction kinetics will change and potentially leading to a noticeable change in the adsorbed species. Since NAPXPS is limited in its ability to track specific molecules, combining with NAPSTM could provide significant conclusions on the reaction mechanism.

In addition to surface preparation and further characterization of single crystal SnO_2, a thin film of another element can be deposited onto the surface to potentially

enhance reactivity. Leclercq et al. were able to show that multiple weight percent dopings of Pt on SnO_2 were able to reduce the reaction temperature needed to convert IPA to CO_2 compared to just SnO_2 alone.[11] As the amount of Pt is increased, a further reduction in the temperature requirement is seen.[11] Thin films of Pt can be evaporated onto the surface of a stoichiometric or reduced surface through e-beam evaporation. With e-beam evaporation, submonolayer layers of Pt can be deposited on the surface. A light Ar^+ ion sputter could also be used to introduce defects in the Pt surface and decrease the amount of Pt to less than a monolayer. STM can then be used to characterize the Pt on the surface and measure the coverage. NAPXPS and NAPSTM studies can be repeated for the Pt surface to determine what role the Pt plays in the reaction mechanism.

Lastly, IPA conversion to CO_2 is only one proposed reaction where SnO_2 has been shown to be an effective catalyst. Other reactions for catalytic conversion of other volatile organic compounds, like MeOH, can also be studied. SnO_2 has been shown to be an effective oxidizing catalyst for CO oxidation to CO_2.[12] Not many ambient pressure XPS studies have completed for reactions on SnO_2 surfaces, which means there is still much fundamental knowledge to be obtained for a very unique material. Fundamental knowledge of solid-gas interfacial reactions is vital for advancing heterogeneous catalysis, which plays a central role in numerous commercial applications, namely industrial-scale chemical production, energy conversion applications and pollution control. Advances in the molecular-level understanding of chemical reactions on solid surfaces are essential for developing rational strategies for designing more efficient and selective catalytic processes.

REFERENCES

[1] Bubert, H.; Rivière, J. C. "Introduction," *Surface and Thin Film Analysis*, Eds. Bubert, H.; Jenett, H.; Wiley-VCH Verlag GmbH, Darmstadt, German, **2002**, p. 1-2.

[2] Somorjai, G., *Introduction to Surface Chemistry and Catalysis*, John Wiley & Sons, Inc., New York, NY, USA, **1994**, p. 12-13.

[3] Mozetič, M.; Vesel, A.; Primc, G.; Eisenmenger-Sittner, C.; Bauer, J.; Eder, A.; Schmid, G.H.S.; Ruzic, D.N.; Ahmed, Z.; Barker, D.; Douglass, K.O.; Eckel, S.; Fedchak, J.A.; Hendricks, J.; Klimov, N.; Ricker, J.; Scherschligt, J.; Stone, J.; Strouse, G.; Capan, I.; Buljan, M.; Milošević, S.; Teichert, C.; Cohen, S.R.; Silva, A.G.; Lehocky, M.; Humpoliček, P.; Rodriguez, C.; Hernandez-Montelongo, J.; Mercier D.; Manso-Silván, M.; Ceccone, G.; Galtayries, A.; Stana-Kleinschek, K.; Petrov, I.; Greene, J.E.; Avila, J.; Chen, C.Y.; Caja-Munoz, B.; Yi, H.; Boury, A.; Lorcy, S.; Asensio, M.C.; Bredin, J.; Gans, T.; O'Connell, D.; Brendin, J.; Reniers, F.; Vincze, A.; Anderle, M.; Montelius, L. "Recent developments in surface science and engineering, thin films, nanoscience, biomaterials, plasma science, and vacuum technology," *Thin Solid Films*, **2018**, 660, p. 120-160.

[4] van Daelen, M.A.; Neurock, M.; van Santen, R.A. "Reactivity of diatomic molecules on Cu (100)," *Surf. Sci.*, **1998**, 417, p.247-260.

[5] Cardineau, B.; Del Re, R.; Marnell, M.; Al-Mashat, H.; Vockenhuber, M.; Ekinci, Y.; Sarma, C.; Freedman, D. A.; Brainard, R. L. "Photolithographic Properties of Tin-oxo Clusters Using Extreme Ultraviolet Light (13.5 nm)," *Microelectron Eng*, **2014**, 127, 44-50.

[6] Oleksak, R. P.; Ruther, R. E.; Luo, F.; Fairley, K. C.; Decker, S. R.; Stickle, W. F.; Johnson, D. W.; Garfunkel, E. L.; Herman, G. S.; Keszler, D. A. "Chemical and Structural Investigation of High-Resolution Patterning with HafSOx," *ACS Appl Mater Inter*, **2014**, 6, 2917-2921.

[7] Haitjema, J.; Zhang, Y.; Ottosson, N.; Brouwer, A. M. "Photoreactions of Tin Oxo Cages, Model EUV Photoresists," *J Photopolym Sci Tec*, **2017**, 30(1), 99-102.

[8] Hinsberg, W. D.; Meyers, S. "Numeric Model for the Imaging Mechanism of Metal Oxide EUV Resists," *Proc. SPIE 10146, Advances in Patterning Materials and Processes XXXIV*, **2017**, 1014604.

[9] Li, M.; Manichev, V.; Yu, F.; Hutchison, D. C.; Nyman, M.; Gustafsson, T.; Feldman, L. C.; Garfunkel, E. L.; "Novel Sn-based Photoresist for High Aspect Ratio Patterning," *Proc. SPIE 10586, Advances in Patterning Materials and Processes XXXV*, **2018**, 105860K.

[10] Batzill, M.; Diebold, U. "The Surface and Materials Science of Tin Oxide," *Prog. Surf. Sci.* **2005**, 79, p. 47-154.

[11] Leclercq, J.; Giraud, F.; Bianchi, D.; Fiaty, K.; Gaillard, F. "New Catalytic System for Oxidation of Isopropyl Alcohol with Thin Film Catalysts," *Catal. Commun.*, **2014**, 46, p. 192-196.

[12] Sun, Y.; Lei, F.; Gao, S.; Pan, B.; Zhou, J.; Xie, Y. "Atomically Thin Tin Dioxide Sheets for Efficient Catalytic Oxidation of Carbon Monoxide," *Angew. Chem. Int. Ed.*, **2013**, 52, p. 10569 – 10572.

[13] Arble, C.; Jia, M.; Newberg, J.T. "Lab-based ambient pressure X-ray photoelectron spectroscopy from past to present," *Surf. Sci. Rep.*, **2018**, 73, p. 37-57.

[14] Kaya, S.; Ogasawara, H.; Näslund, L.A.; Forsell, J.O.; Casalongue, H.S.; Miller, D.J.; Nilsson, A. "Ambient-pressure photoelectron spectroscopy for heterogeneous catalysis and electrochemistry," *Catal. Today*, **2013**, 205, p. 101-105.

[15] Stoerzinger, K.A.; Hong, W.T.; Crumlin, E.J.; Bluhm, H.; Shao-Horn, Y. "Insights into Electrochemical Reactions from Ambient Pressure Photoelectron Spectroscopy," *Acc. Chem. Res.*, **2015**, 48, p. 2976−2983.

[16] Talapin, D. V.; Lee, J.; Kovalenko, M. V.; Shevchenko, E. V. "Prospects of Colloidal Nanocrystals for Electronic and Optoelectronic Applications," *Chem Rev*, **2010**, 110, p. 389-458.

[17] Müller, A.; Kögerler, P. "From Simple Building Blocks to Structures with Increasing Size and Complexity," *Coordin Chem Rev*, **1999**, 182, p. 3-17.

[18] Vetere, V.; Faraoni, M. B.; Podestá, J. C.; Casella, M. L. "Pt-based Chiral Organotin Modified Heterogeneous Catalysts for the Enantioselective Hydrogenation of 3,4-Hexanedione," *Appl Catal A-Gen*, **2012**, 445-446, p. 209-214.

[19] da Silva, E. C.; Mendes, P. R.; Brito, Y. C.; Meneghetti, M. R.; Meneghetti, S. M. P. "Hydrolysis of Triacylglycerides in the Presence of Tin(IV) Catalysts," *Catal Commun*, **2016**, Vol. 78, 7-10.

[20] Nunes, R. S.; Altino, F. M.; Meneghetti, M. R.; Meneghetti, S. M. P. "New Mechanistic Approaches for Fatty Acid Methyl Ester Production Reactions in the Presence of Sn(IV) Catalysts," *Catal Today*, **2017**, 289, 121-126.

[21] Piver, W.T. "Organotin Compounds: Industrial Applications and Biological Investigation," *Environ Health Persp*, **1973,** 4, 61-79.

[22] Ghazi, D.; El-Hiti, G. A.; Yousif, E.; Ahmed, D. S.; Alotaibi, M. H. "The Effect of Ultraviolet Irradiation on the Physicochemical Properties of Poly(vinyl Chloride) Films Containing Organotin(IV) Complexes as Photostabilizers," *Molecules*, **2018**, Vol. 23, Issue 2, 254-268.

[23] Tabassum, S.; Pettinari, C. "Chemical and Biotechnological Developments in Organotin Cancer Chemotherapy," *J Organomet Chem*, **2006**, 691, 1761-1766.

[24] Carraher Jr., C. E.; Roner, M. R. "Organotin Polymers as Anticancer and Antiviral Agents," *J Organomet Chem*, **2014**, 751, 67-82.

[25] Amir, M. K.; Khan, S. Rehman, Z.; Shah, A.; Butler, I. S. "Anticancer Activity of Organotin(IV) Carboxylates," *Inorg Chim Acta*, **2014**, 423, 14-25.

[26] Ramasamy, K.; Kuznetsov, V. L.; Gopal, K.; Malik, M. A.; Raftery, J.; Edwards, P. P.; O'Brien, P. "Organotin Dithiocarbamates: Single-Source Precursors for Tin Sulfide Thin Films by Aerosol-Assisted Chemical Vapor Deposition (AACVD)," *Chem Mater*, **2013**, 25, 266-276.

[27] Nath, M.; Sulaxna. "Thermal Behavior of Organotin(IV) Triazolates: Molecular Precursors for Pure-phase, Nanosized SnS/SnO_2," *Thermochim Acta*, **2009**, 489, 27-36.

[28] Johnson, B. F. G. "From Clusters to Nanoparticles and Catalysis," *Coordin Chem Rev*, **1999**, 190-192, 1269-1285.

[29] Striccoli, M. "Photolithography Based on Nanocrystals: Surface Chemistry of All-inorganic Nanomaterials Enables Three-dimensional Patterning," *Science*, **2017**, 357, 353-354.

[30] Wang, Y.; Fedin, I.; Zhang, H.; Talapin, D. V. "Direct Optical Lithography of Functional Inorganic Nanomaterials," *Science*, **2017**, 357, 385-388.

[31] Li, L.; Liu, X.; Pal, S.; Wang, S.; Ober, C. K.; Giannelis, E. P. "Extreme Ultraviolet Resist Materials for Sub-7 nm Patterning," *Chem Soc Rev*, **2017**, 46,4855-4866.

[32] Wagner, C.; Harned, N. "Lithography Gets Extreme," *Nat Photonics*, **2010**, 4, 24-26.

[33] Yeh, J.J.; Lindau, I.; Atomic Subshell Photoionization Cross Sections and Asymmetry Parameters: 1 $\leqslant Z \leqslant$ 103, *Atom Data Nucl Data*, **1985**, 32, 1-155

[34] Del Re, R.; Passarelli, J.; Sortland, M.; Cardineau, B.; Ekinci, Y.; Buitrago, E.; Neisser, M.; Freedman, D. A.; Brainard, R. L. "Low-line Edge Roughness Extreme Ultraviolet Photoresists of Organotin Carboxylates," *J Micro/Nanolith MEM* **2015**, 14(4), 043506.

[35] Narasimhan, A.; Wisehart, L.; Grzeskowiak, S.; Ocola, L. E.; Denbeaux, G.; Brainard, R. L. "What We Don't Know About EUV Exposure Mechanisms," *J. Photopolym. Sci. Tec.*, **2017**, 30(1), 113-120.

[36] Henrich, V.E.; Cox, P.A. *The Surface Science of Metal Oxides*, Cambridge University Press, Cambridge, UK, **1994**, p. 1-3, 149-157.

[37] Guidi, V., Malagù, C., Carotta, M. C., & Vendemiati, B. "Printed semiconducting gas sensors," *Printed Films*, Eds. Prudenziati, M.; Hormadaly, J.; In Woodhead Publishing Series in Electronic and Optical Materials, Woodhead Publishing Limited, Cambridge, UK, **2012**, p. 278-334.

[38] Sun, Y.F.; Liu, S.B.; Meng, F.L.; Liu, J.Y.; Jin, Z.; Kong, L.T.; Liu, J.H. "Metal Oxide Nanostructures and Their Gas Sensing Properties: A Review," *Sensors*, **2012**, 12, p. 2610-2631.

[39] Zhai, T.; Fang, X.; Liao, M.; Xu, X.; Zeng, H.; Yoshio, B.; Golberg, D. "A Comprehensive Review of One-Dimensional Metal-Oxide Nanostructure Photodetectors," *Sensors*, **2009**, 9, p. 6504-6529.

[40] Bañares, M.A. "Supported metal oxide and other catalysts for ethane conversion: a review," *Catal. Today*, **1999**, 51, p. 319-348.

[41] Royer, S.; Duprez, D. "Catalytic Oxidation of Carbon Monoxide over Transition Metal Oxides," *Chem. Cat. Chem.*, **2011**, 3, p. 24–65.

[42] Ramesh, K.; Chen, L.; Chen, F.; Liu, Y.; Wang, Z.; Han, Y.F. "Re-investigating the CO oxidation mechanism over unsupported MnO, Mn_2O_3 and MnO_2 catalysts," *Catal. Today*, **2008**, 131, p. 477-482.

[43] Umrath, W., *Fundamentals of Vacuum Technology* Leybold GmbH, Cologne, Germany **2016**, p. 14-15, 50-53.

[44] Dohnálek, Z,; Kimmel, G.A.; Joyce, S.A.; Ayotte, P.; Smith, R.S.; Kay, B.D. "Physisorption of CO on the MgO(100) Surface," *J. Phys. Chem. B*, **2001**, 105, p.3747-3751.

[45] Frederick, R. T.; Saha, S.; Trey Diulus, J.; Luo, F.; Amador, J. M.; Li, M.; Park, D.-H.; Garfunkel, E. L.; Keszler, D. A.; Herman, G. S. "Thermal and Radiation Chemistry of Butyltin Oxo Hydroxo: A Model Inorganic Photoresist," *Microelectron. Eng.*, **2019**, 205, p. 26−31.

[46] Schroeder, S. L. M.; Gottfried, M. *Temperature-Programmed Desorption (TPD) Thermal Desorption Spectroscopy (TDS)*, Advanced Physical Chemistry Laboratory, Freie Universität Berlin, **2002**, p. 1-22.

[47] Frederick, R. T.; Herman, G. S. "Characterization of HafSOx Inorganic Photoresists using Electron Stimulated Desorption," *Proceedings of SPIE, Advances in Patterning Materials and Processes XXXIII*, **2016**, 9779, 97790I.

[48] Esmaili, S.; Bass, A. D.; Cloutier, P.; Sanche, L.; Huels, M.A. "Synthesis of complex organic molecules in simulated methane rich astrophysical ices," *J. Chem. Phys.*, **2017**, 147, 224704.

[49] Hinsberg, W. D.; Meyers, S. "Numeric Model for the Imaging Mechanism of Metal Oxide EUV Resists." *Proceedings of SPIE 10146, Advances in Patterning Materials and Processes XXXIV*, **2017**; p. 1014604.

[50] Oleksak, R. P.; Ruther, R. E.; Luo, F.; Amador, J. M.; Decker, S. R.; Jackson, M. N.; Motley, J. R.; Stowers, J. K.; Johnson, D. W.; Garfunkel, E. L.; Keszler, D. A.; Herman, G. S. "Evaluation of Thermal and Radiation Induced Chemistries of Metal Oxo-Hydroxo Clusters for Next-Generation Nanoscale Inorganic Resists." *ACS Appl. Nano Mater.,* **2018**, 1, p. 4548−4556.

[51] Redhead, P. A., "Interaction of slow electrons with chemisorbed oxygen," *Can. J. Phys.*, **1964**, 42, p. 886–905.

[52] Bubert, H.; Rivière, J. C. "Electron Detection," *Surface and Thin Film Analysis*, Eds. Bubert, H.; Jenett, H.; Wiley-VCH Verlag GmbH, Darmstadt, German, **2002**, p. 6-18.

[53] Moulder, J. F.; Stickle, W. F.; Sobol, P. E.; Bomben, K. D. *Handbook of X-ray Photoelectron Spectroscopy*; Perkin-Elmer Corporation: Physical Electronics Division: Eden Prairie, MN, 1992.

[54] Zhong, J-Q; Wang, M.; Hoffmann, W. H.; van Spronsen, M. A.; Lu, D.; Boscoboinik, J. A. "Synchrotron-based ambient pressure X-ray photoelectron spectroscopy of hydrogen and helium," *Appl. Phys. Lett.*, **2018**, 112, 091602.

[55] Seah, M. P. "The Quantitative Analysis of Surfaces by XPS: A Review," *Surf. Interface Anal.*, **1980**, 2(6), p. 222-239.

[56] Briggs, D. "Chapter 2: XPS," *Surface analysis of polymers by XPS and static SIMS*, Eds. Clarke, D.R.; Suresh, S.; Ward, I.M.; Cambridge University Press, Cambridge, UK, **1998**, p. 14-46

[57] Lu, Z. H.; Graham, M. J.; Jiang, D. T.; Tan, K. H. "SiO2/Si(100) interface studied by Al Kα x-ray and synchrotron radiation photoelectron spectroscopy," *Appl. Phys. Lett.*, **1993**, 63(21), p. 2941–2943.

[58] Schmidt, V. "Electron Spectrometry of Atoms using Synchrotron Radiation," *Cambridge Monographs On Atomic, Molecular and Chemical Physics*, Eds. Dalgarno, A.; Knight, P. L.; Read, F. H.; Zarc, R. N.; Cambridge University Press, Cambridge, UK, **1997**, p. 29-31.

[59] Newville, M. *Fundamentals of XAFS*, Consortium for Advanced Radiation Sources, University of Chicago, Chicago, IL, **2004**, p. 1-2

[60] Held, G. "Low-energy Electron Diffraction (LEED)," *Surface and Thin Film Analysis*, Bubert, H.; Jenett, H. Eds.; Wiley-VCH Verlag GmbH, Darmstadt, German, **2002**, p. 71-76.

[61] Woollam, J. A.; Johs, B.; Herzinger, C. M.; Hilfiker, J.; Synowicki, R.; Bungay, C. L. "Overview of Variable Angle Spectroscopic Ellipsometry (VASE), Part I: Basic Theory and Typical Applications," *Proceedings of SPIE, Critical Reviews of Optical Science and Technology*, **1999,** CR72, p. 3-28.

[62] Friedbacher, G. "Scanning Probe Microscopy," *Surface and Thin Film Analysis*, Bubert, H.; Jenett, H. Eds.; Wiley-VCH Verlag GmbH, Darmstadt, German, **2002**, p. 276-281.

[63] Salahuddin, S.; Ni, K.; Datta, S. "The era of hyper-scaling in electronics," *Nature Electronics*, **2018**, 1, p. 442-450.

[64] Grenville, A.; Anderson, J.T., Clark, B.L.; De Schepper, P.; Edson, J.; Greer, M.; Jiang, K.; Kocsis, M.; Meyers, S.T.; Stowers, J. K.; Telecky, A.J.; De Simone, D.; Vandenberghe, G.; Integrated Fab process for metal oxide EUV photoresist, *Proc. SPIE 9425, Advances in Patterning Materials and Processes XXXII*, 94250S (2015).

[65] Krysak, M. E.; Blackwell, J. M.; Putna, S. E.; Leeson, M. J.; Younkin, T. R.; Harlson, S.; Frasure K.; Gstrein, F.; Investigation of novel inorganic resist materials for EUV lithography, *Proc. SPIE 9048, Extreme Ultraviolet (EUV) Lithography*, 904805 (2014).

[66] Henke, B.L.; Gullikson, E.M.; Davis, J.C. *X-ray interactions: photoabsorption, scattering, transmission, and reflection at E=50-30000 eV, Z=1-92*, *Atomic Data and Nuclear Data Tables* 54, 181-342 (1993).

[67] Saha, S.; Park, D.-H.; Hutchison, D. C.; Olsen, M. R.; Zakharov, L. N.; Marsh, D.; Goberna-Ferrón, S.; Frederick, R. T.; Diulus, J. T.; Kenane, N.; Herman, G. S.; Johnson, D. W.; Keszler, D. A.; Nyman, M. "Alkyltin Keggin Clusters Templated by Sodium," *Angew. Chem., Int. Ed.*, **2017**, 56, p. 10140-10144.

[68] Buitrago, E.; Kulmala, T.S.; Fallica, R.; Ekinci, Y. "EUV lithography process challenges," *Frontiers of Nanoscience: Materials and Processes for Next Generation Lithography Vol. 11*, Eds. Robinson, A.; Lawson, R.; Elsevier Ltd., Amsterdam, Netherlands, **2016**, p. 135-170.

[69] Eychenne-Baron, C.; Ribot, F.; Steunou, N.; Sanchez, C.; Fayon, F.; Biesemans, M.; Martins, J. C.; Willem, R. "Reaction of Butyltin Hydroxide Oxide with p-Toluenesulfonic Acid: Synthesis, X-Ray Crystal Analysis, and Multinuclear NMR Characterization of $(BuSn)_{12}O_{14}(OH)_6(4\text{-}CH_3C_6H_4SO_3)_2$," *Organometallics*, **2000**, 19, p. 1940-1949.

[70] Tao, F.; Chen, X.F.; Wang, Z.H.; Xu, G.Q. "Binding and Structure of Acetonitrile on Si(111)-7x7," *J. Phys. Chem. B*., **2002**, 106, p. 3890-3895

[71] Tait, S. L.; Dohnálek, Z.; Campbell, C. T.; Kay, B. D. "n-Alkanes on Pt(111) and on C(0001)/Pt(111): Chain Length Dependence of Kinetic Desorption Parameters," *J. Chem. Phys.*, **2006**, 125, 234308.

[72] Shiobara, E.; Mikami, S.; Yamada, K. "Recent Status of Resist Outgas Testing for Metal Containing Resist at EIDEC," *Proceedings SPIE 10583, Extreme Ultraviolet (EUV) Lithography IX*, **2018**; p 105830B.

[73] Davies, J. V.; Pope, A. E.; Skinner, H. A. "Thermochemistry of Metallic Alkyls: Part 10.-Heats of Combustion of Some Tetra-Alkyls of Tin," *T. Faraday Soc.*, **1963**, 59, p. 2233-2242.

[74] Chuvenkova, O. A.; Domashevskaya, E. P.; Ryabtsev, S. V.; Yurakov, Y. A.; Popov, A. E.; Koyuda, D. A.; Nesterov, D. N.; Spirin, D. E.; Ovsyannikov, R. Y.; Turishchev, S. Y. "XANES and XPS investigations of surface defects in wire-like SnO_2 crystals," *Phys. Solid State*, **2015**, 57, p. 153−161.

[75] Kövér, L.; Moretti, G.; Kovács, Z.; Sanjinés, R.; Cserny, I.; Margaritondo, G.; Pálinkás, J.; Adachi, H. "High Resolution Photoemission and Auger Parameter Studies of Electronic Structure of Tin Oxides," *J. Vac. Sci. Technol., A*, **1995**, 13, p. 1382−1388.

[76] Frederick, R.T.; Amador, J.M.; Goberna-Ferrón, S.; Nyman, M.; Keszler, D.A.; Herman, G.S. Mechanistic Study of HafSOx Extreme Ultraviolet Inorganic Resists, *J Phys Chem C*, **2018**, 122, 16100-16112.

[77] Frederick, R. T.; Diulus, J. T.; Hutchison, D. C.; Nyman, M.; Herman, G. S. "Effect of Oxygen on Thermal and Radiation Induced Chemistries in Organotin Photoresists," *ACS Appl. Mater. Interfaces*, **2019**, 11, p. 4514-4522.

[78] Niibe, M.; Koida, K.; Kakutani, Y. Inhibition of Carbon Growth and Removal of Carbon Deposits on Extreme Ultraviolet Lithography Mirrors by Extreme Ultraviolet Irradiation in the Presence of Water, Oxygen, or Oxygen/Ozone Mixtures, *J Vac Sci Technol B*, **2011**, 29, 011030.

[79] Faradzhev, N. S.; McEntee, M.; Yates, Jr., J. T.; Hill, S. B.; Lucatorto, T. B. EUV-Driven Carbonaceous Film Deposition and Its Photo-oxidation on a TiO_2 Film Surface, **2013**, *J Phys Chem C*, 117, 23072−23081.

[80] Stockman, P. EUV Lithography Adds to Increasing Hydrogen Demand at Leading-edge Fabs, *Solid State Technol*, **2018**, 61(2), 12-16.

[81] van der Horst, R. M.; Beckers, J.; Osorio, E. A.; Astakhov, D. I.; Goedheer, W. J.; Lee, C. J; Ivanov, V. V.; Krivtsum, V. M.; Koshelev, K. N.; Lopaev, D. V.; Bijkerk, F.; Banine, V. Y. Exploring the Electron Density in Plasma Induced by EUV Radiation: I. Experimental Study in Hydrogen, *J Phys D: Appl Phys,* **2016**, 49, 145203.

[82] Yildirim, O.; Buitrago, E.; Hoefnagels, R.; Meeuwissen, M.; Wuister, S.; Rispens, G.; van Oosten, A.; Derks, P.; Finders, J.; Vockenhuber, M.; Ekinci, Y. Improvements in Resist Performance towards EUV HVM, *Proc. SPIE 10143, Extreme Ultraviolet (EUV) Lithography VIII*, **2017**, 101430Q

[83] Kaya, S.; Ogasawara, H.; Näslund, L. Å.; Forsell, J. O.; Casalongue, H. S.; Miller, D. J.; Nilsson, A. Ambient-pressure Photoelectron Spectroscopy for Heterogeneous Catalysis and Electrochemistry, *Catal Today*, **2013**, 205, 102-103.

[84] Kucheyev, S. O.; Baumann, T. F.; Sterne, P. A.; Wang, Y. M.; van Buuren, T.; Hamza, A. V.; Terminello, L. J.; Willey, T. M. Surface Electronic States in Three-dimensional SnO_2 Nanostructures, *Phys Rev B*, **2005**, 72, 035404.

[85] Rehr, J. J.; Albers, R. C. Theoretical Approaches to X-ray Absorption Fine Structure, *Rev Mod Phys*, **2000**, 72(3), 621-654

[86] Frederick, R. T.; Diulus, J. T.; Lyubinetsky, I.; Hutchison, D. C.; Olsen, M. R.; Nyman, M.; Herman, G. S. Surface Characterization of Tin-based Inorganic EUV Resists, *Proceedings Volume 10586, Advances in Patterning Materials and Processes XXXV*, **2018**, 1058607.

[87] Tanaka, K.; Matsuzaki, S.; Toyoshima, I. Photodecomposition of Adsorbed Methoxy Species by UV Light and Formaldehyde Adsorption on Si(111) Studied by XPS and UPS, *J Phys Chem*, **1993**, 97, 5675-5677.

[88] Lin, A. W. C.; Armstrong, N.; Kuwana, T. X-ray Photoelectron/Auger Electron Spectroscopic Studies of Tin and Indium Metal Foils and Oxides, *Anal Chem*, **1977**, 49(8), 1228-1235.

[89] Shuttleworth, D. Preparation of Metal-Polymer Dispersions by Plasma Techniques. An ESCA Investigation, *J Phys Chem-US*, **1980**, 84(12), 1629-1634.

[90] Bluhm, H.; Hävecker, M.; Knop-Gericke, A.; Kleimenov, E.; Schlögl, R.; Teschner, D.; Bukhtiyarov, V. I.; Ogletree, D. F.; Salmeron, M. Methanol Oxidation on a Copper Catalyst Investigated Using in Situ X-ray Photoelectron Spectroscopy, *J Phys Chem B*, **2004**, 108(38), 14340-14347.

[91] Thrower, J. D.; Abdulgalil, A. G. M.; Collings, M. P.; McCoustra, M. R. S.; Burke, D. J.; Brown, W. A.; Dawes, A.; Holtom, P. J.; Kendall, P.; Mason, N. J.; Jamme, F.; Fraser, H. J.; Rutten, F. J. M. Photon- and Electron-stimulated Desorption from Laboratory Models of Interstellar Ice Grains, *J Vac Sci Technol A*, **2010**, 28, 799-806.

[92] Alves, L.L; Coche, P.; Ridenti, M.A.; Guerra, V. Electron Scattering Cross Sections for the Modeling of Oxygen-Containing Plasmas, *Eur. Phys. J. D*, **2016**, 70, 124.

[93] Naghma, R.; Vinodkumar, M.; Antony, B. Total Cross Sections for O_2 and S_2 by Electron Impact, *Rad. Phys. Chem.*, **2014**, 97, 6-11.

[94] Thiele, C.; Telten, A.; Echtermeyer, T. J.; Ferrari, A.C.; Casiraghi, C.; Löhneysen, H. V.; Krupke, R. Electron-beam Induced Direct Etching of Graphene, *Carbon*, **2013**, 64, 84-91.

[95] LaVilla, R. E. The O Kα and C Kα Emission and O K Absorption Spectra from O_2 and CO_2. IV, *J Chem Phys*, **1975**, 63, 2733-2737.

[96] Cardineau, B. "Molecular Organometallic Resists for EUV," *Frontiers of Nanoscience: Materials and Processes for Next Generation Lithography Vol. 11*, Eds. Robinson, A.; Lawson, R.; Elsevier Ltd., Amsterdam, Netherlands, **2016**, p. 377-420.

[97] Ghosh, S; Pradeep,C. P.; Sharma, S. K.; Reddy, P. G.; Pal, S. P.; Gonsalves, K. E. "Recent Advances In Non-chemically Amplified Photoresists for Next Generation IC Technology," *RSC Adv.*, **2016**, 6, p. 74462.

[98] Ober, C. K.; Xu, H.; Kosma, V.; Sakai, K.; Giannelis, E. P. "EUV Photolithography: Resist Progress and Challenges," *Proceedings of SPIE 10583, Extreme Ultraviolet (EUV) Lithography IX*, **2018**, p. 1058306.

[99] Sakai, K; Jung, S. H.; Pan, W; Giannelis, E. P.; Ober, C. K. "Development of Metal Organic Cluster EUV Photoresists," *Proceedings of SPIE 10960, Advances in Patterning Materials and Processes XXXVI*, **2019**, p. 1096015.

[100] Fallica, R.; Haitjema, J.; Wu, L.; Castellanos, S.; Brouwer, F.; Ekinci, Y. "Absorption Coefficient and Exposure Kinetics of Photoresists at EUV," *Proceedings of SPIE 10143, Extreme Ultraviolet (EUV) Lithography VIII*, **2017**, p. 101430A.

[101] Xin, F.; Pope, M. T.; Long, G. J.; Russo, U. "Polyoxometalate Derivatives with Multiple Organic Groups. 2. Synthesis and Structures of Tris(organotin) α, β-Keggin Tungstosilicates," *Inorg. Chem.*, **1996**, 35(5), p. 1207-1213.

[102] Diulus, J. T.; Frederick, R. T.; Li, M.; Hutchison, D. C.; Olsen, M. R.; Lyubinetsky, I.; Árnadóttir, L.; Garfunkel, E. L.; Nyman, M.; Ogasawara, H.; Herman, G. S. "Ambient-Pressure X-ray Photoelectron Spectroscopy Characterization of Radiation-Induced Chemistries of Organotin Clusters," *ACS Appl. Mater. Interfaces*, **2019**, 11, p. 2526-2534.

[103] Haitjema, J., Zhang, Y., Vockenhuber, M., Kazazis, D., Ekinci, Y., Brouwer, A., "Extreme ultraviolet patterning of tin-oxo cages," *Proceedings of SPIE 10143, Extreme Ultraviolet (EUV) Lithography VIII*, **2017**, p. 1014325

[104] Van de Kerkhof, M.; Jasper, H.; Levasier, L.; Peeters, R.; van Es, R.; Bosker, J.-W.; Zdravkov, A.; Lenderink, E.; Evangelista, F.; Broman, P.; Bilski, B.; Last, T. "Enabling sub-10nm node lithography: presenting the NXE:3400B EUV scanner," *Proceedings of SPIE, Extreme Ultraviolet (EUV) Lithography VIII*, **2017**, 10143, p. 10143D.

[105] Frederick, R. T.; Diulus, J. T.; Lyubinetsky, I.; Hutchison, D. C.; Olsen, M. R.; Nyman, M.; Herman, G. S. "Surface Characterization of Tin-based Inorganic EUV Resists," *Proceedings of SPIE 10586, Advances in Patterning Materials and Processes XXXV*, **2018**, p. 1058607.

[106] Campbell, S. A. "The Science and Engineering of Microelectronic Fabrication," *The Oxford Series in Electrical and Computer Engineering*, Sedra, A. S., Eds.; Oxford University Press, New York, NY, USA, **2001**, p. 187-190.

[107] Cumpson, P. J.; Seah, M. P. "Elastic Scattering Corrections in AES and XPS. II. Estimating Attenuation Lengths and Conditions Required for their Valid Use in Overlayer/Substrate Experiments," *Surf. Interface Anal*., **1997**, 25, p. 430-446.

[108] Fadley, C. S. "1. Basic Concepts of X-ray Photoelectron Spectroscopy," *Electron Spectroscopy: Theory, Techniques and Applications*, Brundle, C. R.; Baker, A. D. Eds.; Academic Press, London, England, UK, **1978**, p. 23-75.

[109] Itikawa, Y.; Mason, N. "Cross Sections for Electron Collisions with Water Molecules," *J. Phys. Chem. Ref. Data*, **2009**, 38, p. 1-22.

[110] Itikawa, Y. "Cross Sections for Electron Collisions with Oxygen Molecules," *J. Phys. Chem. Ref. Data*, **2005**, 34, p. 1-20.

[111] Hutchison, D.C.; Stern, R.D.; Olsen, M.R.; Zakharov, L.N.; Persson, K.A.; Nyman, M. "Alkyltin clusters: the less symmetric Keggin isomers," *Dalton T.*, **2018**, 47(29), p. 9804-9813.

[112] Srivastava, S.K.; Krishnakumar, E.; Fucaloro, A.F.; van Note, T. "Cross sections for the production of cations by electron impact on methanol," *J. Geophys. Res.*, **1996**, 101(E11), p. 26155-26160.

[113] Berger, M.J.; Hubbell, J.H.; Seltzer, S.M.; Chang, J.; Coursey, J.S.; Sukumar, R.; Zucker, D.S.; Olsen, K. *XCOM: Photon Cross Section Database* (version 1.5). [Online] Available: http://physics.nist.gov/xcom [2019, June 23]. National Institute of Standards and Technology, Gaithersburg, MD.

[114] Sullivan, J. P.; Gibson, J. C.; Gulley, R. J.; Buckman, S. J. "Low-Energy Electron Scattering From O_2," *J. Phys. B: At. Mol. Opt.*, **1995**, 28(19), p. 4319.

[115] Muse, J.; Silva, H.; Lopes, M. C. A.; Khakoo, M. A. "Low Energy Elastic Scattering of Electrons From H_2 and N_2," *J. Phys. B: At. Mol. Opt.*, **2008**, 41(9), p. 095203.

[116] Varella, M. T. do N.; Bettega, M. H. F.; Lima, M. A. P.; Ferreira L. G. "Low-Energy Electron Scattering by H_2O, H_2S, H_2Se, and H_2Te," *J. Chem. Phys.*, **1999**, 111(14), p. 6396.

[117] Khakoo, M. A.; Blumer, J.; Keane, K.; Campbell, C.; Silva, H.; Lopes, M. C. A.; Winstead, C.; McKoy, V.; da Costa, R. F.; Ferreira, L. G.; Lima, M. A. P.; Bettega, M. H. F. "Low-Energy Electron Scattering From Methanol and Ethanol," *Phys. Rev. A*, **2008**, 77, p. 042705.

[118] Itikawa, Y. "Cross Sections for Electron Collisions with Nitrogen Molecules," *J. Phys. Chem. Ref. Data*, **2006**, 35, p. 31-53.

[119] Yu, M.; Xu, H.; Kosma, V.; Odent, J.; Kasahara, K.; Giannelis, E.; Ober, C. "Positive Tone Nanoparticle Photoresists: New Insight on the Patterning Mechanism," *J. Photopolym. Sci. Tec.*, **2016**, 29(3), p. 509-512.

[120] Sharps, M.C.; Frederick, R.T.; Javitz, M.L; Herman, G.S.; Johnson, D.W.; Hutchison, J.E. "Organotin Carboxylate Reagents for Nanopatterning: Chemical Transformations during Direct-Write Electron Beam Processes," *Chem. Mater.*, **2019**, 31(13), p. 4840-4850.

[121] Olynick, D.; Schwartzberg, A.; Keszler, D.A "Mainstreaming inorganic metal-oxide resists for high-resolution lithography," *Frontiers of Nanoscience: Materials and Processes for Next Generation Lithography Vol. 11*, Eds. Robinson, A.; Lawson, R.; Elsevier Ltd., Amsterdam, Netherlands, **2016**, p. 350-371.

[122] Inomata, Y.; Albrecht, K.; Yamamoto, K.; "Size-Dependent Oxidation State and CO Oxidation Activity of Tin Oxide Clusters," *ACS Cat.*, **2018**, 8(1), p. 451-456.

[123] Boeglin, M.L.; Wessels, D.; Henshel, D. "An investigation of the relationship between air emissions of volatile organic compounds and the incidence of cancer in Indiana counties," *Environ. Res.*, **2006**, 100, p. 242–254.

[124] National Center for Biotechnology Information. PubChem Database. Isopropyl alcohol, CID=3776, https://pubchem.ncbi.nlm.nih.gov/compound/Isopropyl-alcohol (accessed on Sept. 6, 2019)

[125] Christensen, P. A.; Mashhadani, Z. T. A. W.; Abd Halim Bin Md Ali "In situ FTIR studies on the oxidation of isopropyl alcohol over SnO_2 as a function of temperature up to 600 °C and a comparison to the analogous plasma-driven process," *Phys. Chem. Chem. Phys.*, **2018**, 20, p. 9053-9062.

[126] Paredis, K.; Ono, L.K.; Mostafa, S.; Li, L.; Zhang, Z.; Yang, J.C.; Barrio, L.; Frenkel, A.I.; Cuenya, B.R. "Structure, Chemical Composition, And Reactivity Correlations during the In Situ Oxidation of 2-Propanol," *J. Am. Chem. Soc.*, **2011**, 133, p. 6728–6735

[127] Farfan-Arribas, E.; Madix, R.J. "Role of Defects in the Adsorption of Aliphatic Alcohols on the TiO_2(110) Surface," *J. Phys. Chem. B*, **2002**, 106, p. 10680-10692.

[128] Wu, Y.Y.; Kung, H.H. "Probing properties of the interfacial perimeter sites in TiOx/Au/SiO_2 with 2-propanol decomposition," *Appl. Catal. A-Gen.*, **2017**, 548, p. 150–163

[129] Batzill, M.; Katsiev, K.; Diebold, U. "Surface Morphologies of SnO_2," *Surf. Sci.*, **2003**, 529(3), p. 295-311.

[130] Batzill, M.; Katsiev, K.; Burst, J. M.; Diebold, U.; Chaka, A. M.; Delley, B. "Gas-phase-dependent properties of SnO_2 (110), (100), and (101) single-crystal surfaces: Structure, composition, and electronic properties," *Phys. Rev. B*, **2005**, 72, p. 165414.

[131] Cox, D. F.; Fryberger, T. B.; Semancik, S., "Oxygen vacancies and defect electronic states on the Sn02(110)-1x1 surface," Phys. Rev. B., **1988**, 38(3) p. 2072-2083.

[132] Domashevskaya, É.P.; Ryabtsev, S.V.; Turishchev, S.Y.; Kashkarov, V.M.; Yurakov, Y.A.; Chuvenkova, O.A.; Shchukarev, A.V. "XPS and XANES Studies of SnO_x Nanolayers," *J. Struct. Chem*+., **2008**, 49, p. S80-S91.

[133] Dangerfield, A.; Li, M.; Hutchinson, D.; Nyman, M.; Garfunkel, E. L.; Chabal, Y. J. "Interfacial Evolution and Patterning Performance of a Novel Tin-Oxo EUV Resist Film" *In Preparation*.